Stony Brook University

Studies of Hydrodynamic Processes in Alternative Magneto-Inertial Fusion Devices

A Dissertation Presented

by

Lina Zhang

to

The Graduate School

in Partial Fulfillment of the

Requirements

for the Degree of

Doctor of Philosophy

in

Applied Mathematics and Statistics

Stony Brook University

May 2014

Stony Brook University

The Graduate School

Lina Zhang

We, the dissertation committee for the above candidate for the

Doctor of Philosophy degree, hereby recommend

acceptance of this dissertation.

Roman Samulyak - Dissertation Advisor
Professor, Department of Applied Mathematics and Statistics

James Glimm - Chairperson of Defense
Distinguished Professor, Department of Applied Mathematics and
Statistics

Xiangmin Jiao - Member
Associate Professor, Department of Applied Mathematics and
Statistics

Michael Zingale - Outside Member
Associate Professor, Department of Physics and Astronomy

This dissertation is accepted by the Graduate School.

Charles Taber
Dean of the Graduate School

Abstract of the Dissertation

Studies of Hydrodynamic Processes in Alternative Magneto-Inertial Fusion Devices

by

Lina Zhang

Doctor of Philosophy

in

Applied Mathematics and Statistics

Stony Brook University

2014

The main goal of the research is evaluation of the plasma jet driven magneto-inertial fusion (PJMIF) concept via simulations. To achieve this goal, the development of mathematical models and numerical algorithms for PJMIF has been performed, and large-scale simulation studies have been conducted.

In the PJMIF concept, a plasma liner, formed by the merger of a large number of radial, highly supersonic plasma jets, implodes on a magnetized plasma target and compresses it to conditions of the fusion ignition. 1- (spherically symmetric), 2- and 3-dimensional simulations of the implosion of plasma liners and compression of plasma targets have been performed using the Fron-

Tier code based on the method of front tracking. Scaling laws and related fusion theories have been investigated and their conclusions compared with our results.

Compared with previous theoretical and numerical studies of PJMIF, our numerical models and algorithms implement several new physics models important to PJMIF. One of them is a numerical model for atomic physics processes. The influence of atomic physics processes on the plasma liners for magneto-inertial nuclear fusion has been studied based on equation of state models with dissociation and ionization. These atomic processes in imploding liners reduce the temperature and increase the Mach number of liners, result in higher stagnation pressure and the fusion energy gain. Other factors influencing liner implosion are the residual vacuum gas and heat conduction. By replacing the idealized vacuum region with realistic residual gas and adding the Spitzer electronic thermal conductivity, we quantified their effects in the low-energy simulation regime.

We have demonstrated that the internal structure of argon plasma liners, formed by the merger of plasma jets is strongly influenced by a cascade of oblique shock waves generated by colliding jets. Corresponding studies have been performed using 2- and 3-dimensional simulations. 10 times reduction of the stagnation pressure was found compared with spherically symmetric liner with the same pressure and density profiles at the merging radius, due to the influence of oblique shock waves and adiabatic compression heating. The experiment results of single argon plasma jet propagation and two argon plasma jets merger reported by Plasma Liner Experiment group in Los Alamos

National Lab have also been compared with our simulations.

A multi-stage computational approach for simulations of the liner-target interaction and the compression of plasma targets has been developed to minimize computing time. Simulations revealed important features of the target implosion process, including instability and disintegration of targets. The non-uniformity of the leading edge of the liner caused by the oblique shock waves between jets leads to instabilities during target compression. By using front tracking, the evolution of targets has been studied in 2- and 3-dimensional simulations. Optimization studies of target compression with different number of jets have also been performed.

Key Words: simulation, front tracking, interface, plasma jet/liner/target, PJMIF, EOS, fusion energy, pressure, instabilities

To my father, Yuanqin Zhang

To my mother, Mei Zhou

Table of Contents

List of Figures

xv

List of Tables

Acknowledgements

Although this dissertation is written under my name, it embodies the efforts of many people. I am really grateful to all those people and really appreciate this great experience.

First of all, I would like to express my sincere gratitude to my advisor Professor Roman Samulyak for his support of my Ph.D. study. It is my great honor and fortune to work under his supervision. I still remember the day when I first discussed with him about joining his group. His creative ideas, wide knowledge and great patience have contributed a lot to my growth as a qualified graduate student. He is one of the most important persons in my whole life. I would also thank Professor Xiangmin Jiao who gave us great lectures and Professor James Glimm who has contributed a lot to our department. Thank you so much for being on my dissertation committee.

I would like to thank all my friends during my years of study at Stony Brook for their friendship and encouragement. I would like to mention Hyoungkeun Kim for his great help during these years and his wife for all the delicious cakes. I will never forget those days we worked and discussed together. I would like say thank you to Lingling Wu, Hongren Wei, Tongfei Guo, Wei Li, Morris Chen, Telang Gaurish, Kwangmin Yu, Jun Ma and Hang

Chapter 1

Introduction

1.1 Overview of Plasma Jet Driven Magneto-Inertial Fusion and Goals

In the PJMIF concept, a plasma liner, formed by the merger of a large number of radial, highly supersonic plasma jets, implodes on a magnetized plasma target and compresses it to conditions of the fusion ignition. One of the concerns about solid liner driven fusion is called stand-off problem which says that the target-related hardware should be located sufficiently far from the hot spot and another concern is about liner manufacturing cost. Thio *et al.* [1] then suggested the plasma liner method, that is, a spherical array of supersonic plasma jets, launched from the periphery of the implosion chamber, can be used to create a spherically symmetric plasma liner to implode on the central magnetized target. Such a plasma liner is assembled when the jets intersect and merge with each other at an intermediate radius r_m, as shown schematically in Fig. 1.1 [2].

1

Several theoretical and numerical works [2, 3, 4, 5, 6, 7, 8, 9] have addressed the dynamics of spherically symmetric liners imploding on deuterium plasma targets or undergoing the self-implosion process and properties of plasma liner/target achieved after the implosion. 3-dimensional simulation focusing on the internal fine structure of plasma liners has been studied carefully [10]. The Plasma Liner Experiment group in Los Alamos National Lab has contributed a lot in this area. They proposed a collaborative project to explore the feasibility of plasma liner formation to reach a desirable stagnation pressure. They studied related theories such as the concept-level overview of plasma liner MIF with analysis on the efficiency of conversion [11] and estimates of confinement time to assess the fusion energy yield using exact solution to a self-similar converging shock model [12]. One-dimensional radiation-hydrodynamic simulations were then presented to provide insight into the scaling of stagnation pressure with initial conditions using the RAVEN and HELIOS codes [8]. Three-dimensional simulations were also performed to study the effects of discrete plasma jets on the processes of plasma liner formation and self-implosion using smoothed particle hydrodynamics (SPH) [6]. Finally, experiment results of single argon plasma jet propagation [5] and two argon plasma jets merger [13] were reported recently using a pulsed-power-driven plasma railgun by HyperV Technologies Corp.

The main goal of this research is the evaluation of the plasma jet driven magneto-inertial fusion (PJMIF) concept via simulations studies, which includes: a) Spherically-symmetric simulation studies including scaling laws and new physics models important to PJMIF. One of the most important issues we

2

need to solve is how to improve the fusion energy gain. According to the scaling law derived from Parks' formulas [2], the gain increases with the reduction of the liner thickness provided that such a liner is still capable of compressing the target. A thin liner with less initial kinetic energy increases the fusion energy gain while it has the same ability to compress the target to the fusion condition. Keeping the liner unchanged, there is also an optimal choice for the target radius based on the initial conditions in order to get the maximum fusion energy gain. Heavy liner material such as argon is also proposed to yield better results. One of the new physics models implemented in our code is a numerical model for atomic physics processes. The influence of atomic physics processes on the plasma liners for magneto-inertial nuclear fusion has been studied based on equation of state models with dissociation and ionization. These atomic processes in imploding liners reduce the temperature and increase the Mach number of liners, result in higher stagnation pressure and the fusion energy gain. Other factors influencing the liner implosion are the residual vacuum gas and heat conduction. By replacing some unrealistic values in the idealized vacuum region with realistic residual gas states and adding the Spitzer electronic thermal conductivity, we quantified their effects in the low-energy simulation regime. b) 3-dimensional studies of plasma liners, including propagation of single jet, merger of jets and self-implosion of liner. Based on oblique shock waves and other factors, the internal fine structure of plasma liners obtained by the merger of plasma jets, the decrease of self-implosion pressure comparing to the uniform liner and the final potential implications to the target compression have been explained precisely. The experiment program Plasma Liner

Experiment (PLX) at LANL aims on experiments on plasma jet propagation/merging, and liner formation/implosion. We obtained available relevant data from them and compared the results. c) Multi-dimensional studies of implosion with target including evolution of liner, compression of plasma target with instabilities and comparison in different dimensional cases. We studied the scaling laws and related theories using 1-dimensional spherically symmetric liner based on its uniform structure. But due to the oblique shock waves and other factors, the internal structure of plasma liners is not uniform. We then performed 2-dimensional simulations to show the Rayleigh-Taylor (RT) instabilities on the interface in detail and the influence of the surface behavior on the fusion energy and stagnation pressure. RT instability is an instability of an interface between two fluids of different densities that occurs when one of the fluids is accelerated into the other [21]. The instability in our simulations is not in the traditional sense since there is no random perturbation and it is also combined with RichtmyerMeshkov (RM) instability which is open to discuss [22]. After bubbles and spikes growing into certain heights, we observed that the target broke into fragments. We performed different numbers of jets to form the liners and compared the results. 3-dimensional simulations were also performed to obtain further investigation. In the 3-dimensional simulations, the interface structure is much more complicated than it is in a 2-dimensional space. A multi-stage computational approach has been developed to minimize computational time. We used a coarse mesh before the liner reaches the target and refined mesh afterwards. Similar target behaviors were observed compared with the 2-dimensional simulation. The MHD processes in the target prevent

target diffusion. To simulate this effect without including MHD in the code, we set the velocity of the target to be zero before the liner-target interaction. Simulation results were also compared with 1-dimensional uniform cases to obtain better understanding. My work includes: a) EOS model validation, discussion of functions implemented in FronTier, studies of influence of vacuum and heat conduction, and related simulation studies (joint work with H. Kim and Prof. Roman Samulyak); b) discussion of functions implemented in FronTier, comparison studies with oblique shock theory and experimental results, and related simulation studies (joint work with H. Kim and Prof. Roman Samulyak); c) Multi-dimensional studies of implosion with target (joint work with Prof. Roman Samulyak). The plasma EOS model mentioned in our papers is first implemented in this area. Multi-dimensional studies of implosion with target, especially the 3-dimensional space, shed some light on the PJMIF project.
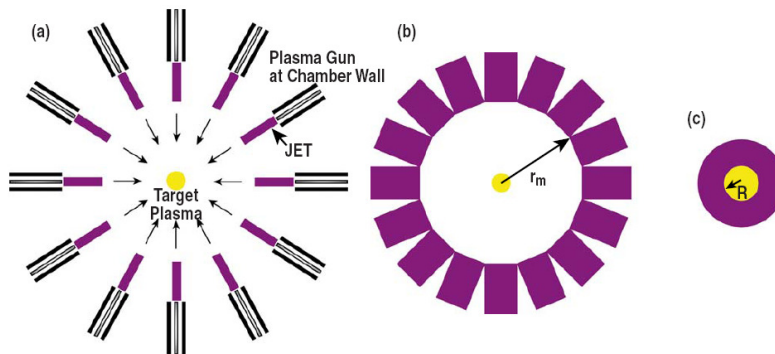
Figure 1.1: Schematic of plasma jet induced magnetized target fusion: (a) Plasma gun shoot supersonic jets; (b) Plasma liner is formed at the merging radius; (c) Plasma liner implodes on the target.

1.2 Methods and Tools

First, all of our simulations are performed using FronTier code. There are two approaches to deal with fluid dynamics, Eulerian method and Lagrangian method (see Fig. 1.2). In Eulerian method, flow moves with respect to the coordinate frame (or computational mesh), which is fixed to laboratory frame. With Eulerian method, the evaluation of fluid states is relatively easy to be extended to higher dimension but it is difficult to capture dynamic interfaces. In Lagrangian method, the substance represented by material parcels moves together with the flow. With Lagrangian method, it is easy to deal with the resolution of the interface but the material parcels are severely distorted by the flow especially in high dimension. A hybrid Lagrangian-Eulerian code based on the front tracking method [14] called FronTier code [15] is then used in our simulations. Front tracking is a numerical method in which surfaces of discontinuity are given explicit computational degrees of freedom together with continuous solutions at regular grid points. Thus the code has special ability to track dynamically moving fronts (often interfaces between materials) which are Lagrangian meshes moving through a volume filling Eulerian grid. Fig. 1.3 and Fig. 1.3 [14] show the schematic of this idea in 2-dimensional and 3-dimensional spaces. We observe that the front (or interface) is presented with a lower dimensional structure in regular Eulerian grid, that is, curve in rectangle and surface in cuboid. With this description and its own data structures, we obtain the first essential idea to the front tracking method. Fig. 1.4 also shows the representation in detail in 3-dimension. The CURVE consists of BONDs with the linking order of BONDs corresponding to the natural order

along the CURVE. Each BOND is a pair of POINTs with the straight-line segment joining them. SURFACE is composed of TRIANGLEs while the linking order has no intrinsic relation to SURFACE. NODEs correspond to boundaries of CURVE and CURVEs correspond to the boundaries of SURFACE. COMPONENTs are equivalence class separated by the HYPERSURFACEs (SURFACEs in 3-dimension). The second critical idea is to define the dynamics of the front derived from corresponding differential equation with Riemann solvers and a finite difference algorithm to couple the interior cells to the front with ghost cell extrapolation [16]. The propagation of points on the front (dynamics of the front) is operated in two directions: normal and tangential to the interface (see Fig. 1.5 [16]). The operation projects the flow state into either along the normal ray or the tangent plane from the point being propagated. A Riemann problem with the two states at either side of the front is solved to find the front speed and updated states. The method of characteristics tracing back linearly from the new front position with Rankine-Hugoniot conditions across the front is used to obtain the time updated states at the front. By averaging the wave speed computed from initial Riemann problem and the value obtained from method of characteristics, the final front speed is solved. For cells with a regular stencil, a standard scheme, such as Monotonic Upstream-centered Scheme for Conservation Laws (MUSCL) [17] is used. For cells with an irregular stencil, some cells are cut by the front. But then it may cause an error because of finite differences in the level set function. The ghost cell method is used to solve this error recently. A Riemann solver is used for interior-front coupling. The solver enters into the front propagation and

<div align="center">(a)   (b)</div>
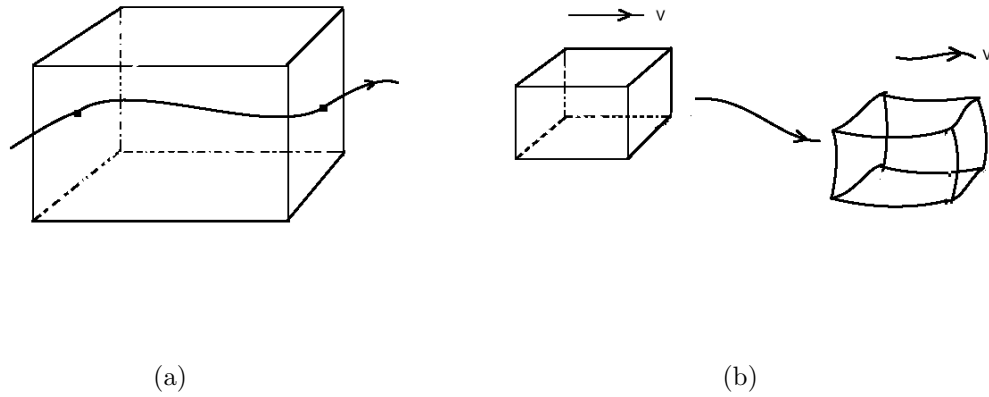
Figure 1.2: Mesh of Eulerian and Lagrangian method

the setting of the front states. Based on solved front states, extrapolation as constant is performed for the ghost cell. Local states near the front are then given by extrapolating states for each side of the front. With ghost cell states, the regular states including the irregular one has a full stencil of states from a single side of the interface. A normal finite difference solver is then used to compute the states including regular ones and extrapolated ghost ones.

The code is ideal when discontinuities are an important feature such as complex shocks and wave front interactions. Based on the elimination (or large reduction) of numerical diffusion across interfaces, front tracking improves the accuracy of multiphase simulations. Explicit geometrical interfaces also improve the simulation of processes occurring at material interfaces (for instant, phase transition), and enable the use of different numerical models in regions separated by interfaces (for example, electrically conducting and non-conducting fluids). That is one of the most important reasons why we use this

<div align="center">8</div>
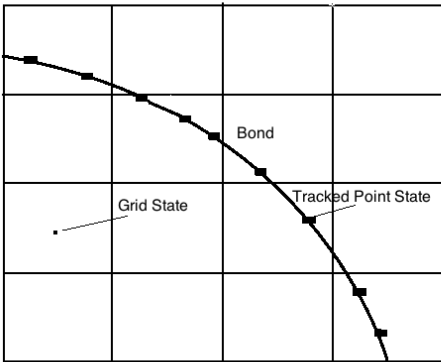
Figure 1.3: Schematic of front tracking method in 2-dimensional space, solution is composed of finite difference grid and a dynamic grid following the front.
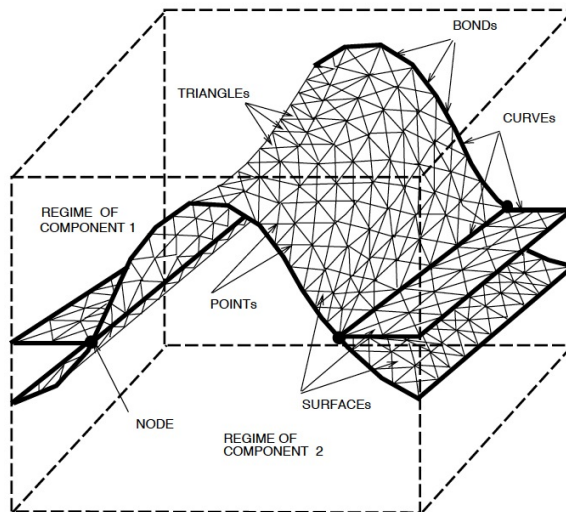
Figure 1.4: Schematic of front tracking method in 3-dimensional space, solution is composed of finite difference grid and a dynamic grid following the front.
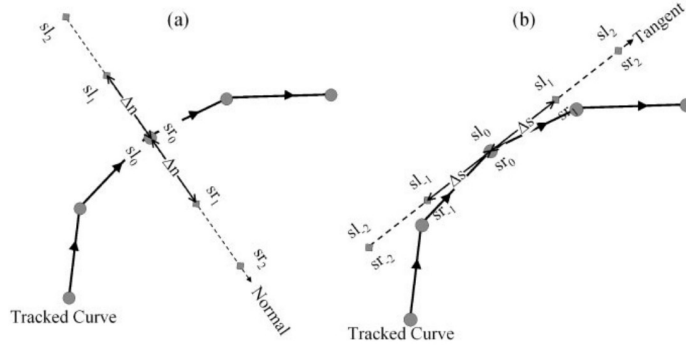
Figure 1.5: Schematic of point propagating in 2-dimensional space: (a) normal and (b) tangential directions.

code for all our simulations, especially for simulations of targets compressed by liners. The FronTier code has been used on various supercomputers for the simulations [18] of fundamental (turbulent fluid mixing) and applied problems (liquid accelerator targets, fuel jets, pellet fueling of tokamaks, etc.). It supports compressible and incompressible Navier-Stokes equations with phase transitions, MHD equations in the low magnetic Reynolds number approximation [19], and oil reservoir equations.

Second, compared with previous theoretical and numerical studies of PJMIF, our numerical models and algorithms implement several new physics models important to PJMIF. One of them is a numerical model for atomic physics dynamics. In addition to conservation laws, the thermodynamic relation between state variables under a given set of physical conditions referred as an equation of state (EOS) is also required to completely specify the problem (close the system of equations). It connects two or more state functions associated with the matter, such as temperature, pressure, volume, or internal energy. It is useful to describe intrinsic properties of gas, fluid and solid. For a

given system, the temperature, volume, and pressure are dependent with the general form as

$$f(p, V, T) = 0$$

where p is pressure, V is volume, T is absolute temperature (Kelvin (K)). Most previous works have used polytropic ideal gas EOS for the plasma liner material, which can be expressed as

$$p = \rho(\gamma - 1)e$$

where p is pressure, ρ is density, $\gamma = C_p/C_v$ is adiabatic index (ratio of specific heats), $e = C_v T$ is the internal energy per unit mass (specific internal energy), C_p is specific heat at constant pressure and C_v is the specific heat at constant volume. But as the increase of the liner temperature reported in previous studies is large enough to cause dissociation and ionization, we need to consider the influence of atomic processes. In order to solve this problem, we implemented the equation of state model for deuterium [20] and developed a numerical equation of state model for high-Z gases that resolves multiple ionization based on local thermodynamic equilibrium. These EOS models have been implemented in the FronTier code [15] and used for all of our plasma simulations. Other factors influencing liner implosion are the residual vacuum gas and heat conduction. We replace the idealized vacuum region with realistic residual gas and analyze the results. Heat conduction can also cause important changes during the implosion process. We investigate this factor by applying the Spitzer electronic thermal conductivity in our simulations.

Finally, we introduce our visualization tools for data analysis. For 1-dimensional simulation, MATLAB is enough for plotting. But for 2-dimensional and 3-dimensional simulations, we always obtain a huge amount of output files which are not easy to be visualized. FronTier solves this problem by producing vtk files which contain the state information such as density, temperature and pressure at each position and are visualized by VisIt. VisIt was originally developed by the Department of Energy (DOE) Advanced Simulation and Computing Initiative (ASCI) to analyze the results of terascale simulations. It contains plugin architecture for custom readers, data operators, plots and many different user interfaces. Users can produce visualizations, animate the evolution, manipulate with multiple operators and mathematical expressions, do qualitative and quantitative analysis and finally save the images or animations. Because of its rich set of visualization features, a wide variety of data including scalar and vector fields defined on 2- and 3-dimensional structured, adaptive and unstructured meshes can be visualized. Sometimes MATLAB is also used for specific analysis for 2- and 3-dimensional simulations.

1.3   Dissertation Organization

In Chapter 2, we introduce the scaling Laws, EOS model with atomic process based on Saha Equations and influence of residual vacuum gas and heat conduction in detail with simulations results. Chapter 3 presents the 3-dimensional studies of plasma liner including propagation of single jet, merger of jets and self-implosion of liner. Simulation results are explained with oblique shock wave theories. The experiment results by Plasma Liner Experiment

group are also presented. Chapter 4 discusses liner-target interaction in multi-dimensional regimes. Because of the non-uniformity of the plasma liner merged by jets, Rayleigh-Taylor instabilities are introduced to explain the evolution of target surface in 2-dimension and 3-dimension. The influence on the fusion energy and stagnation pressure is also presented with different number of jets. Finally, Chapter 5 reports some of the on-going work and plans for the future direction.

Chapter 2

Spherically-symmetric Simulation of Plasma Liner and Target Compression

We start with spherically symmetric simulations for this thesis. Spherically symmetric simulations of the implosion of plasma liners and compression of plasma targets in the concept of the plasma jet driven magneto-inertial fusion have been performed using FronTier code. Scaling laws and related fusion theories have been investigated to compare with our results. Several new physics models are also implemented in the code [7].

2.1   Scaling Laws and Comparison with Theory

Fusion energy gain in our simulations is obtained by the following approach. At each time step, the production of fusion neutrons is calculated for each computational cell of the target based on the thermodynamic state of the

target and the fusion reactivity [23]:

$$< \sigma v >= c_1 \theta(T) \sqrt{\frac{[BG^2/(4\theta(T))]^{1/3}}{DT^3}} \exp\left[-3\left[BG^3/(4\theta(T))\right]^{1/3}\right], \quad (2.1)$$

where

$$\theta(T) = \frac{T}{1 - \frac{T(c_2 + T(c_4 + Tc_6))}{1 + T(c_3 + T(c_5 + Tc_7))}}.$$

Here the temperature T is in keV units, the dimension of the fusion reactivity is cm^3/s, and $c_1 = 1.17302 \times 10^{-9}$, $c_2 = 0.0151361$, $c_3 = 0.0751886$, $c_4 = 0.00460643$, $c_5 = 0.0135$, $c_6 = -1.0675 \times 10^{-4}$, $c_7 = 1.366 \times 10^{-5}$, $BG = 34.3827$, $D = 1.124656 \times 10^6$. The neutron production is integrated in the target volume and time to obtain the total fusion energy

$$E_{\text{fusion}} = (e_{\text{neutron}} + e_\alpha) \int_{t0}^{\infty} \int \int \int_{V_{target}(t)} < \sigma v > \frac{n^2}{4} dV \, dt, \quad (2.2)$$

where n is the target number density, $e_{\text{neutron}} = 14.1$ MeV is the neutron energy and $e_\alpha = 3.5$ MeV is the alpha particle energy released in the process of fusion. Finally, the fusion gain is obtained as

$$G_{\text{simulation}} = E_{\text{fusion}}/E_{\text{liner}}, \quad (2.3)$$

where $E_{\text{liner}} = E_{\text{kinetic}} + E_{\text{internal}} \simeq E_{\text{kinetic}}$ is the total initial energy of the plasma liner.

The scaling law, which shows the theoretical predictions of the fusion

gain dependence on parameters, is derived from Parks' formulas [2].

$$G = 10^{-4} \frac{\langle \sigma v \rangle_{DT}}{T^{3/2}} \frac{R^2}{L_{jet}} (n_0 n_L)^{1/2} \left(\frac{m_{jet}}{2.5}\right)^{1/2} C_L C_T^{3/2} \frac{\eta_E}{0.25}$$

$$= 10^{-4} \frac{\langle \sigma v \rangle_{DT}}{T^{3/2}} \frac{R_m R_0}{\sqrt{R} L_{jet}} (n_0 n_L)^{1/2} \left(\frac{m_{jet}}{2.5}\right)^{1/2} \frac{\eta_E}{0.25} \qquad (2.4)$$

where T and R are the target temperature and radius at stagnation (cm), n_0 is the initial target density (cm^{-3}), L_{jet} is the length of jets forming the liner (cm), n_L is the initial liner density (cm^{-3}), m_{jet} is the jet ion mass (amu), $C_L = R_m/R$ is the radial convergence of the liner, $C_T = R_0/R$ is the radial convergence of the target, and η_E is the electric gun efficiency which is equal to one throughout this paper.

According to Eq.2.4, the fusion energy gain increases with reduction of initial liner thickness since the liner with smaller thickness contains smaller initial energy while produces identical fusion energy [3]. Further reduction of thickness is not practical since the propagation of very short plasma jets prior to their merger results in the spreading of their density. Another way is the inclusion of alpha particles heating. It assumes that alpha particles produced in the nuclear fusion process escape the target without interaction. In [3], a very simplified model was proposed: Some fractions of alpha particles are absorbed locally and deposit their energy of 3.5 MeV per alpha particle in order to evaluate the effect on fusion gain. Alpha heating had small effect on fusion gain of deuterium liner with increment of 4.3% using absorption coefficient of 0.35. Fusion gain with larger targets compressed by heavy xenon liners and double layer deuterium-xenon liners were also simulated. With

16

inclusion of alpha heating, the fusion energy gain was improved significantly with xenon liner. The use of composite deuterium-xenon liner, which had been expected to provide extra fuel for thermonuclear reaction, reduced the fusion gain because of the compression of deuterium liner layer and can't achieve ignition without alpha heating. Keeping the liner unchanged, 20 cm target was the most optimal for the given liner [3]. To evaluate the effect of alpha heating for targets producing significant energy gains, the same simulations with alpha heating turned off were also performed. With alpha heating turned off, the fusion gain of 15 cm target was reduced to 5.6 while the fusion gain of 20 cm target was reduced to 6.0. The conclusion is that with inclusion of alpha particles heating, the fusion gain reached 10 in the most optimal setup as follows: target with 20 cm radius compressed by a single layer xenon liner (see Fig. 2.1 [3]).

In [7], we proposed a further explanation of the scaling law using argon liner and plasma EOS. Here we use the code features of solving Riemann problem, front tracking and applying plasma EOS model. The initial simulation parameters for a deuterium liner are consistent with [3]: The liner is 5 cm thick with density $\rho = 3.8 \times 10^{-5}\,\text{g/cm}^3 = 9.2 \times 10^{18}\,1/\text{cm}^3$, temperature $T = 0.0358\,\text{eV} = 415.4\,\text{K}$, pressure $P = 0.65\,\text{bar}$, velocity $v = 100\,\text{km/s}$, and the Mach number $M = 60$. The plasma target is initially 5 cm in radius with uniform density $\rho = 8.3 \times 10^{-6}\,\text{g/cm}^3 = 2 \times 10^{18}\,1/\text{cm}^3$, temperature $T = 100\,\text{eV}$ and pressure $P = 640.3\,\text{bar}$. The mesh size is 0.2 mm with flow through boundary condition for right side and reflecting boundary for left side. Fig. 2.2 shows the Mach number evolution and Fig. 2.3 depicts the evolution of
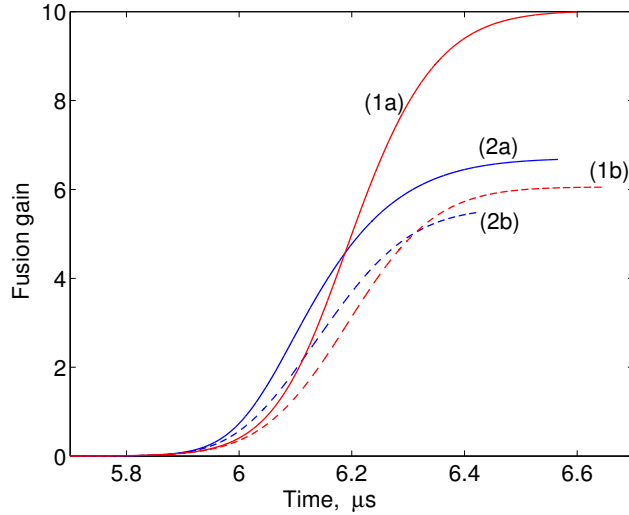
Figure 2.1: Influence of alpha heating on the fusion gain of targets compressed by 5 cm thick single layer xenon liner. Solid lines show the fusion gain in the presence of alpha heating and dashed lines show the fusion gain when alpha heating was turned off. Initial target radii are: 20 cm (1a,b) and 15 cm (2a,b).

fusion energy gain in the target after interaction with the liner. In agreement with previous theoretical and numerical estimates of scaling laws, the increase of Mach number for the plasma EOS model leads to larger compression of the target with higher fusion energy gain.

The next simulations show the compression of plasma targets by heavy argon liners. Here we use the code features of solving Riemann problem, front tracking and applying plasma EOS model. Based on the liner information in [3], we proposed the following initial conditions of the argon liner with comparable particle number density: density $\rho = 4.0 \times 10^{-4}\,\mathrm{g/cm^3} = 6.03 \times 10^{18}\,\mathrm{1/cm^3}$, temperature $T = 0.7269\,\mathrm{eV} = 8435.15\,\mathrm{K}$, and pressure $P = 9.35\,\mathrm{bar}$. The mesh size is 0.2 mm with flow through boundary condition for right side and reflecting boundary for left side. According to [3], more
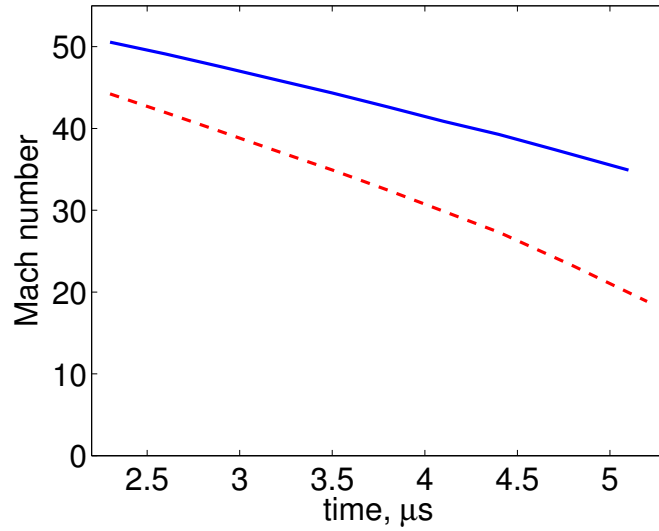
Figure 2.2: (Joint work with H. Kim) Evolution of mean Mach number of the liner before the interaction with the target by the plasma (blue solid line) and polytropic (red dashed line) EOS models.
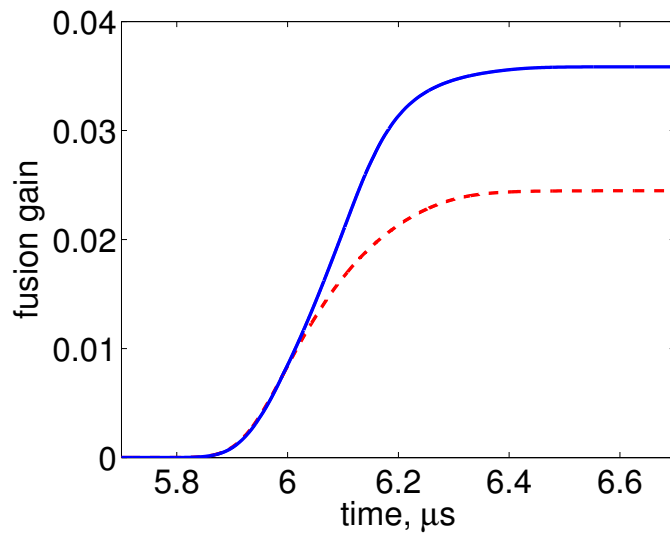
Figure 2.3: (Joint work with H. Kim) Evolution of the fusion energy gain of the plasma target compressed by the deuterium liner at given time with polytropic EOS (red dashed line) and plasma EOS (blue solid line).
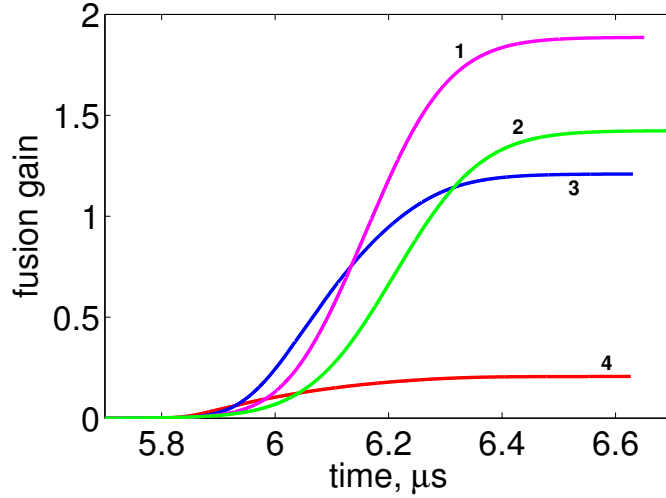
Figure 2.4: (Joint work with H. Kim) Comparison of fusion gains with different target radius using same argon liner and polytropic EOS (target radius: 15 cm (1), 20cm (2), 10 cm (3), 5 cm (4)).

fusion energy gain for argon liner (heavy material) compared with deuterium line is obtained. Keep liner unchanged, [3] found that the most optimal target radius for the given xenon liner was 20 cm. Similarly, Fig. 2.4 shows that the target with radius of 15 cm is the most optimal for argon liner by showing dynamics of the corresponding fusion gain. This target size is then used for the investigation of the influence of ionization on the target stagnation pressure and fusion energy gain later.

2.2   EOS Models and Influence of Ionization

The thermodynamic relation between state variables under a given set of physical conditions is referred as an equation of state (EOS). It connects two or more state functions associated with the matter, such as temperature, pressure,

20

volume, or internal energy. A particular relation of the form $p = \rho(\gamma - 1)e$ is called polytropic ideal gas EOS, where p is pressure, ρ is density, $\gamma = C_p/C_v$ is adiabatic index (ratio of specific heats), $e = C_v T$ is the internal energy per unit mass (specific internal energy), C_p is specific heat at constant pressure and C_v is the specific heat at constant volume. Most previous works have used this model for the plasma liner material. However, in order to describe the simulation more precisely, as the increase of the liner temperature reported in previous studies is large enough to cause dissociation and ionization with energy sinks, our group used the EOS model for deuterium [20] and developed a numerical EOS model for high-Z gases (argon) for multiple ionization instead of polytropic ideal gas EOS. Both EOS models assume local thermodynamic equilibrium.

[7] and [20] describe a deuterium EOS model: Specific internal energy and pressure of a partially dissociated and ionized diatomic gas can be expressed as

$$E = \left(\frac{1 - f_d}{2(\gamma_m - 1)} + \frac{f_d + f_i}{\gamma - 1} \right) \frac{kT}{m_a} + \frac{1}{2} f_d \frac{k\epsilon_d}{m_a} + f_i \frac{k\epsilon_i}{m_a}, \tag{2.5}$$

$$P = \left(\frac{1}{2} + \frac{1}{2} f_d + f_i \right) \frac{\rho kT}{m_a} \tag{2.6}$$

where k is the Boltzmann constant, m_a is the atom(ion) mass , γ_m is specific heat ratio for molecules and $\gamma = 5/3$ is specific heat ratio for atoms. The

21

definitions of dissociation $f_d(\rho, T)$ and ionization $f_i(\rho, T)$ fractions are

$$
\begin{aligned}
f_d &= (n_a + n_i)/n, \\
f_i &= n_i/n,
\end{aligned}
$$

where $n \equiv 2n_g + n_a + n_i = \rho/m_a$ is the total number density of *nuclei*, and n_g, n_a, and n_i stand for the number densities of gas D_2 molecules, D atoms, and D^+ ions, respectively. The dissociation energy and ionization energy for deuterium are $\epsilon_d = 4.48$ eV, and $\epsilon_i = 13.6$ eV, respectively. The dissociation and ionization fractions can be solved from Saha equations [24]. The equations for deuterium (in eV units) can be expressed as

$$
\frac{f_d^2}{1 - f_d} = 1.55 \times 10^{24} \frac{T^{\alpha_d}}{n} \exp\left(-\frac{\epsilon_d}{T}\right), \tag{2.7}
$$

$$
\frac{f_i^2}{1 - f_i} = 3.0 \times 10^{21} \frac{T^{\alpha_i}}{n} \exp\left(-\frac{\epsilon_i}{T}\right), \tag{2.8}
$$

where $\alpha_i = 3/2$ and $\alpha_d = 0.327$. These values are the best approximation of deuterium thermodynamic data [25]. For hydrodynamic code solvers we need to get pressure as a function of density and specific internal energy. Then we have to solve the quadratic equations (2.8) - (2.7) for f_i and f_d respectively. A nonlinear equation $\Phi(\rho, E, T) = 0$ is then obtained to get T for given values of ρ and E by substituting f_i and f_d into the energy equation (2.5). Finally we obtain dissociation and ionization fractions and the pressure based on the temperature.

Suppose multiply ionized state with ionization energies $I_1, I_2, \ldots, I_Z$ can

be obtained for high-Z monatomic gas EOS model (see details in our paper [7]). Similar to previous discussion, specific internal energy and pressure can be expressed as

$$
\begin{aligned}
E &= \frac{3}{2}\left(1+f_e\right)\frac{kT}{m_a} + \frac{1}{m_a}\sum Q_m f_m + \frac{1}{m_a}\sum W_m f_m, & (2.9) \\
P &= \left(1+f_e\right)\frac{\rho kT}{m_a} & (2.10)
\end{aligned}
$$

where f_e is fraction of electrons and f_m is fraction of ions with m as the ionization degree, $Q_m = I_1 + I_2 + \ldots + I_m$ is defined as the energy needed to remove m electrons, with m-th ionization potential I_m, and W_m denotes the electronic excitation function. The fractions of electrons and ions satisfy the following equations

$$
\sum_m m f_m = f_e, \quad \sum_m f_m = 1
$$

and also the system of Saha equations based on the assumption of local thermodynamic equilibrium

$$
\frac{f_{m+1}f_e}{f_m} = \frac{2m}{\rho}\frac{u_{m+1}}{u_m}\left(\frac{2\pi m_e kT}{h^2}\right)^{3/2}\exp\left(-\frac{I_{m+1}}{kT}\right), \quad m = 1,\ldots,Z, \quad (2.11)
$$

where u_m, $m = 1,\ldots,Z$ are electron partition functions that are already known and h is the Planck constant. In order to solve the system of Saha equations in an EOS library more efficiently as it is a coupled system of Z nonlinear equations, we introduce the continuum approximation of the particle

number densities, ionization energy function and ionization fractions as in [24],

$$n_m \to n(m), \quad I_m \to I(m), \quad f_m \to f(m),$$

with the integral form of conservation laws

$$\int m\, n(m)dm = n_e,$$

$$\int n(m)dm = n,$$

By applying these to (2.11), the coupled system of Saha equations is reduced to a single ordinary differential equation

$$\left(1 + \frac{d\log n}{dm}\right)n_e = CT^{3/2}\exp{-\frac{I(m+1)}{kT}}. \tag{2.12}$$

The function of argon ionization energies is shown with continuum representation in Fig. 2.5 by a third order piece-wise polynomial approximation [7].

Based on [24], the distribution of ionized states $n(m)$ at given temperature and density resembles a sharp, Gaussian-type curve centered at the average ionization $\bar{m}$ defined as

$$\bar{m} = \frac{\int m\, n(m)dm}{\int n(m)dm} = \frac{n_e}{n} = m\big|_{\frac{dn}{dm}=0}.$$
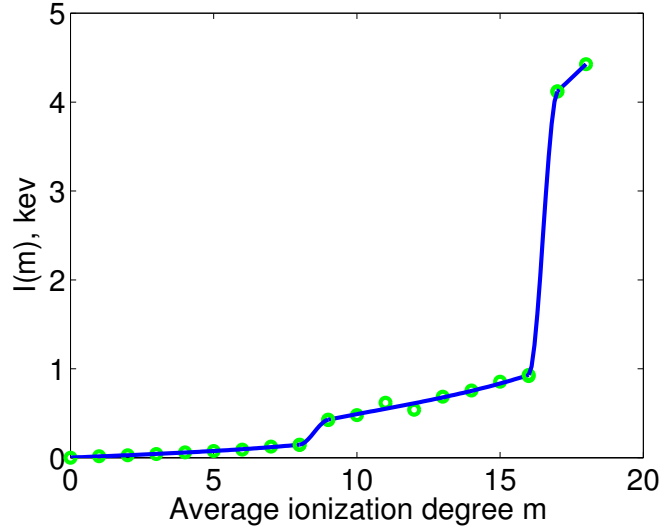
Figure 2.5: (Joint work with H. Kim) Ionization energies of argon atom (circles) and their continuum representation by function $I(m)$ (solid line).

By applying it to (2.12), the average ionization value becomes

$$\bar{m} = \frac{CT^{3/2}}{n} \exp -\frac{\bar{I}}{kT}.$$

(2.13)

Then we have internal energy and pressure for average ionization modeling

$$
\begin{aligned}
E &= \frac{3}{2}\left(1+\bar{m}\right)\frac{kT}{m_a} + \frac{1}{m_a}Q(\bar{m}), & (2.14) \\
P &= n\left(1+\bar{m}\right)kT & (2.15)
\end{aligned}
$$

Substitute (2.15) or (2.14) into the Saha equation(2.13) with the continuum approximation for discrete functions I_m and Q_m, we obtain a nonlinear equation to solve $\bar{m}$ at given pressure or specific internal energy with value of density. We then obtain other quantities such as sound speed required by the
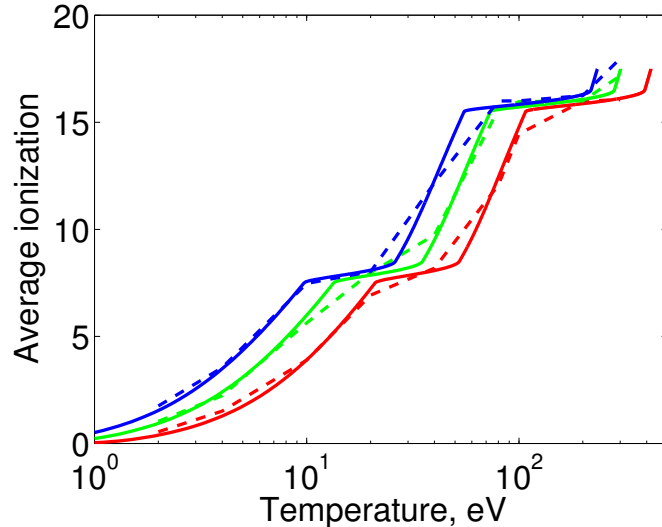
Figure 2.6: (Joint work with H. Kim) Comparison of the average ionization calculated using the Zeldovich model (solid lines) and the full system of coupled Saha equations (dashed lines) at given temperature and three density values, $5 \times 10^{-3} \, g/cm^3$ (red bottom lines), $5 \times 10^{-5} \, g/cm^3$ (green middle lines), and $5 \times 10^{-7} \, g/cm^3$ (blue top lines) is shown.

Riemann solver based on the expression for entropy from [24] and the local gamma-law fit.

The coupled system of Saha equations is compared with average ionization EOS model as follows: Fig. 2.6 shows the relation between the average ionization level and temperature of argon gas for three density values: $5 \times 10^{-7} \, g/cm^3$, $5 \times 10^{-5} \, g/cm^3$, and $5 \times 10^{-3} \, g/cm^3$. Fig. 2.7 presents the corresponding pressure curves obtained by the coupled system of Saha equations and the average ionization EOS model. Only negligibly small discrepancies near non-smooth sections of the curve appear which also gives us the validation of the average model [7] .

However, in order to implement this EOS model in FronTier code [26]
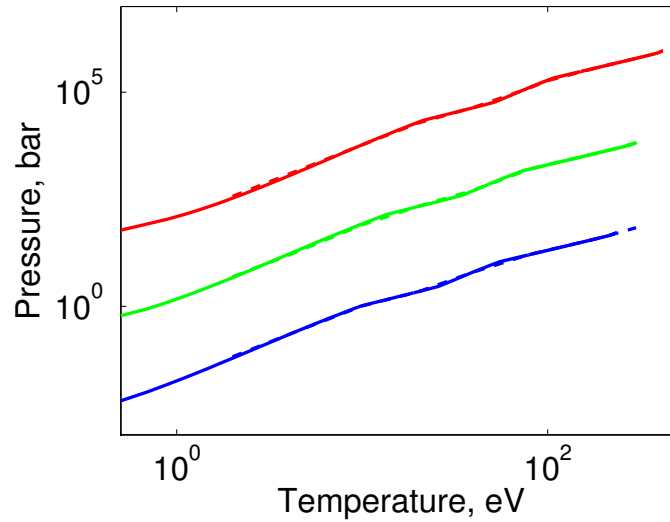
Figure 2.7: (Joint work with H. Kim) Comparison of pressure values calculated using the Zeldovich model (solid lines) and the full system of coupled Saha equations (dashed lines). Temperature dependence of the argon gas pressure at three density values, $5 \times 10^{-3}\,g/cm^3$ (top lines), $5 \times 10^{-5}\,g/cm^3$ (middle lines), and $5 \times 10^{-7}\,g/cm^3$, (bottom lines) is shown.

with second order MUSCL type schemes and interface propagation algorithms, we need to solve numerically a Riemann problem which requires an ability to calculate the sound speed and integrals of Riemann invariant type expressions along characteristics. Explicit expressions are then needed for the entropy, sound speed, and other thermodynamic properties of the system (2.6) - (2.7) [20]. Precomputed tabulated data sets are often used to reduce calculation time of Riemann-type invariants [7].

To show the influence of the ionization with EOS models, we present the simulation results using deuterium and argon gas liner [7] . For the same simulation in section 2.1 explaining the scaling law, Fig. 2.8a shows the evolution of mean dissociation and ionization fractions of deuterium by averaging values across the liner at each time step during liner implosion before the interaction with the target. The fractions increase as the temperature increases with time. Here the mean dissociation fraction is 0.02 while the ionization fraction remains negligible small at the late stage because of small changes of the temperature in the liner. Fig. 2.8b presents the evolution of dissociation and ionization energy ratios defined as the dissociation (ionization) energy divided by the specific internal at given time. The dissociation energy remains a significant fraction of the liner energy while the ionization energy is negligible. The dissociation energy sink causes liner temperature around 3 times smaller compared with the simulation with polytropic EOS and the corresponding Mach number increases approximately by the factor of two (see Fig. 2.2).

The ionization process becomes significant when the interaction between the liner and target starts. The front layer of the liner is almost completely
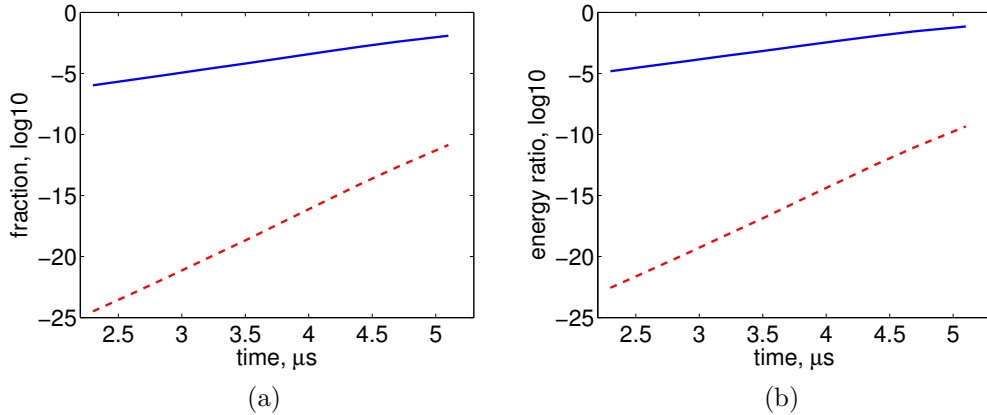
Figure 2.8: (Joint work with H. Kim) Evolution of atomic processes in the liner before the interaction with the target at given time. (a) Mean dissociation fraction (blue solid line) and ionization fraction (red dashed line) of the liner (b) Mean dissociation energy ratio (blue solid line) and mean ionization energy ratio (red dashed line) of the liner.

dissociated and ionized at stagnation time with more ionization energy ratio than dissociation energy ratio (see Fig. 2.9). The profiles of temperature and Mach number are also compared with the corresponding polytropic EOS model simulation (see Fig. 2.10). It is known that the increase of the Mach number leads to much larger compression of the target, we then obtain higher fusion energy gain and maximum pressure in the target (see Fig. 2.3 and Fig. 2.11). We also notice that atomic processes had no effect on the target deconfinement time defined in [20], that is, the time during which the pressure in the target decreases by the factor of two compared with the fully compressed state.

Next is the compression of plasma target by the heavy argon liner. We use the same simulation in section 2.1. The target stagnation pressure of polytropic EOS is 61 Mbar, compared with 110 Mbar when the argon EOS with ionization is used (see Fig. 2.12). And the fusion energy gain are 1.9 and
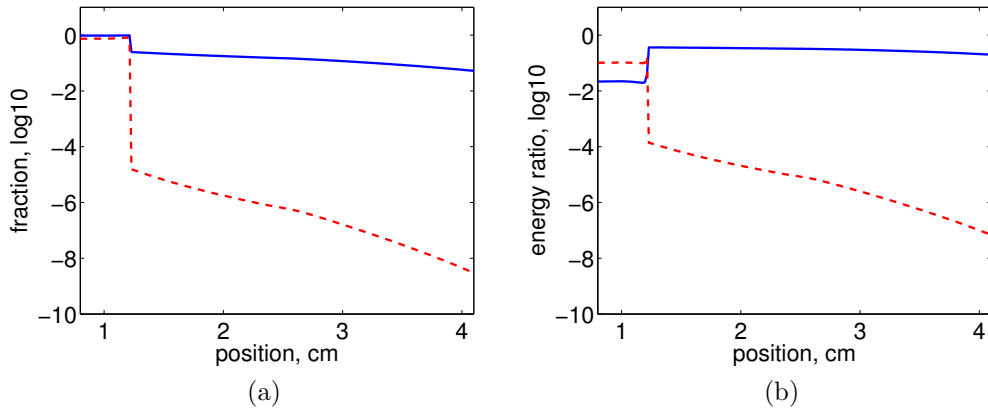
Figure 2.9: (Joint work with H. Kim) Values of dissociation and ionization fractions, and the corresponding energy ratios across the liner around the stagnation time. (a) Dissociation (blue solid line) and ionization (red dashed line) fractions, (b) Dissociation (blue solid line) and ionization (red dashed line) energy ratios.
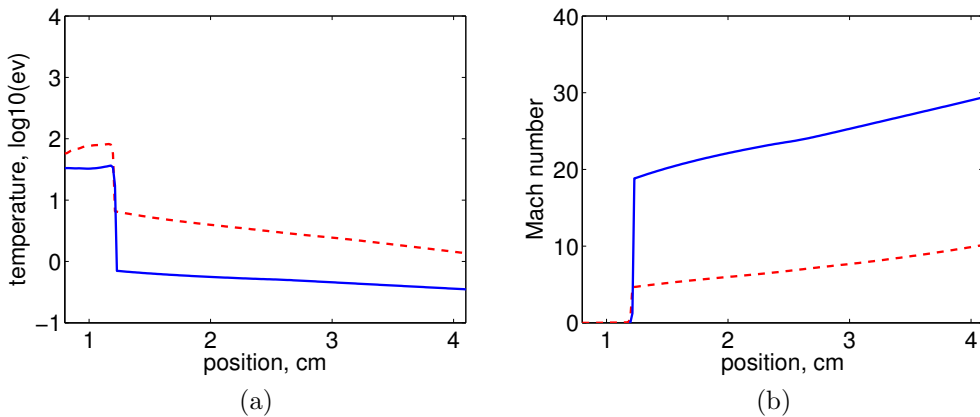
Figure 2.10: (Joint work with H. Kim) Temperature (a) and Mach number (b) across the liner around the stagnation time by plasma (blue solid line) and polytropic (red dashed line) EOS models.
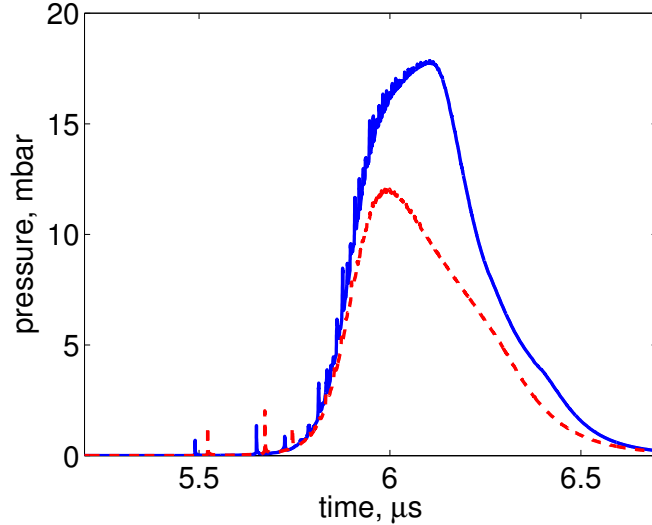
Figure 2.11: (Joint work with H. Kim) Evolution of maximum pressure with polytropic EOS (red dashed line) and plasma EOS (blue solid line) of deuterium liner at given time.

3.7 correspondingly (Fig. 2.13) [7] .

We also perform argon liner self-collapse simulations to show the ionization effect. Fig. 2.14 shows simulation results using the parameters of case 6 of Table II in [4] from Plasma Liner Experiment group in Los Alamos National Lab. The mesh size is 0.2 mm with flow through boundary condition for right side and Neumann boundary for left side. We also compare the results with other codes (see Figures 5 and 12 in [4]). For the polytropic EOS, the maximum pressure using the FronTier code is between the results using the RAVEN and HELIOS codes. For the plasma EOS, maximum pressure using the FronTier code is similar to the HELIOS code result obtained with PROPACEOS non-LTE EOS [4].
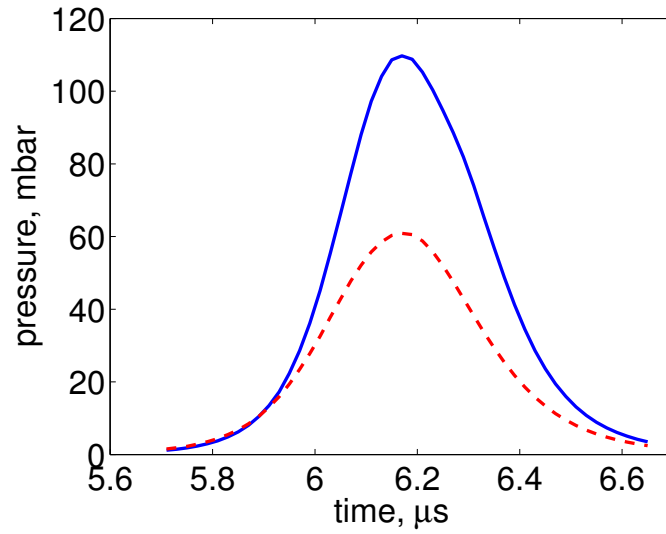
Figure 2.12: (Joint work with H. Kim) Evolution of maximum pressure with polytropic EOS (red dashed line) and plasma EOS (blue solid line) of argon liner at given time.
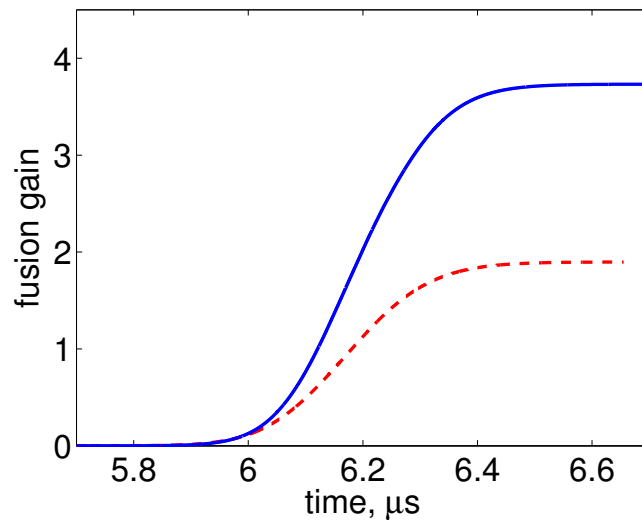
Figure 2.13: (Joint work with H. Kim) Evolution of the fusion energy of the plasma target compressed by the argon liner at given time with polytropic EOS (red dashed line) and plasma EOS (blue solid line).
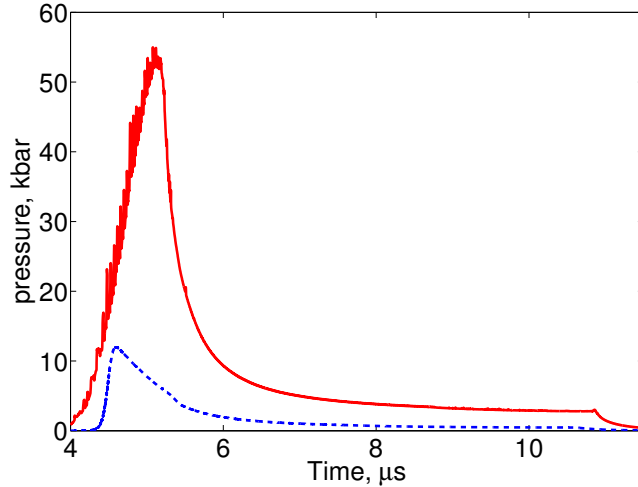
Figure 2.14: (Joint work with H. Kim) Evolution of maximum pressure of case 6 of Table II in [4] by using plasma EOS (red solid line) and polytropic EOS (blue dashed line).

2.3 Influence of Vacuum and Heat Conduction

During the evolution of the self-collapse liner by solving the hyperbolic equations in FronTier code, the solver produces some unrealistic values because of the shock produced in the idealized vacuum region around the origin (see Fig. 2.15). These unphysical states can affect the final results after interaction with the liner. In order to clarify this influence, we replace this region with realistic residual gas: at each time step, we replace the layer between the origin and liner with realistic residual gas, density $\rho = 10^{-12} \, \text{g/cm}^3$, and pressure $p = 10^{-9} \, \text{bar}$. Here we use the code features of solving Riemann problem and front tracking. The mesh size is 0.2 mm with flow through boundary condition for right side and Neumann boundary for left side. When the interface between the liner and vacuum reaches the origin, we delete the interface to make the

33

code run correctly.

Fig. 2.15 shows density and pressure distributions at the time just before final step with realistic residual gas simulation compared with regular simulation (without replacing). The unrealistic high values around the origin are removed. Fig. 2.16 shows density and pressure distributions at the time just after final step with realistic residual gas simulation compared with regular simulation (without replacing). There is a sharp increase of density (or pressure) around the origin. The reason is that after solving the hyperbolic equations, a sharp discontinuity in the simulation profile appears because of a huge jump from previous value replacing. Fig. 2.17 shows the comparison of maximum pressure with and without realistic gas replacing. The maximum pressure values are both around 470 bar. We conclude that the unrealistic values have a negligibly small effect in the low-energy PLX regime. Note that in Fig. 2.17, there is also a sharp increase of maximum pressure as in Fig. 2.16. The unrealistic value around the origin in regular simulation acts as a smooth factor. For this evaluation we ignore the conservation laws since the material and energy in this idealized vacuum region are very small compared with the whole system. And the final results also show that this effect is negligibly small, otherwise our method is questionable.

Next we evaluate the importance of the heat conduction on the argon liner self-implosion. Heat conduction is the transfer of internal energy because of temperature gradient. In gases it can take place by microscopic diffusion and collisions of particles such as ions and electrons during their random motion from a hotter to a colder region and approach thermal equilibrium. All the
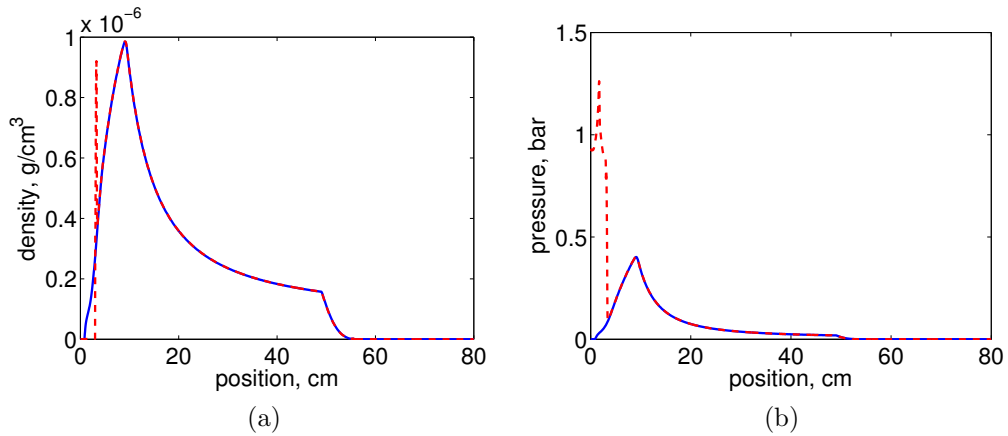
Figure 2.15: (a) Density and (b) Pressure distributions just before final step with realistic residual gas replacing simuation (blue solid line) compared with regular simulation (without replacing, red dashed line) at the same time.
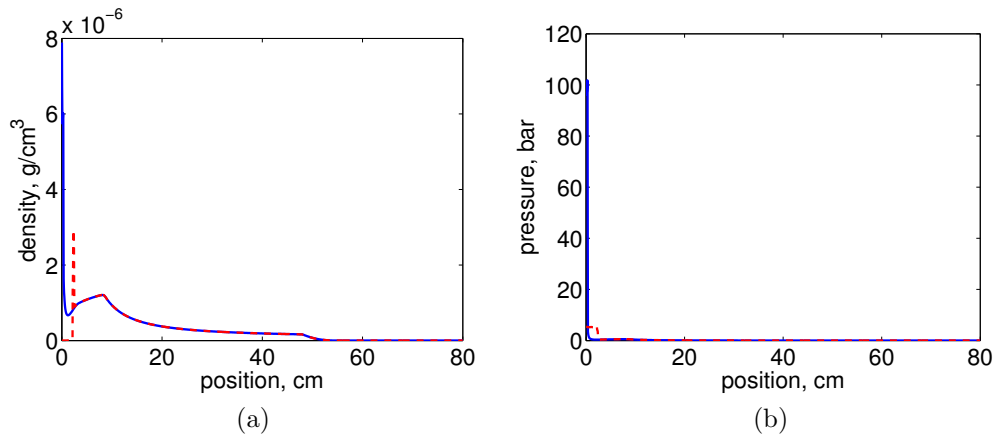
Figure 2.16: (a) Density and (b) Pressure distributions just after final step with realistic residual gas replacing simuation (blue solid line) compared with regular simulation (without replacing, red dashed line) at the same time.
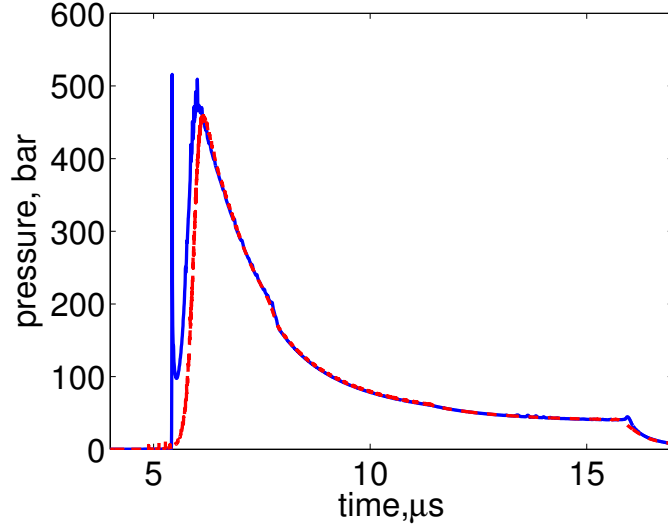
Figure 2.17: Evolution of maximum pressure around stagnation with (blue solid line) and without (red dashed line) realistic gas replacing.

previous simulations are preformed without heat conduction. In this section we evaluate this factor by adding the thermal conductivity. Here we use the code features of solving Riemann problem and applying heat conduction effect.

The heat conduction equation in 1-dimensional space is expressed as follows:

$$\frac{\partial T}{\partial t} = \frac{\partial}{\partial x}(\alpha \frac{\partial T}{\partial x})$$

where α is the thermal diffusivity and $\alpha = k/(c_p\rho)$ with thermal conductivitty k, mass density ρ and specific heat capacity c_p, T is the temperature. Thermal conductivity k is a material-specific quantity. We use the Spitzer electronic thermal conductivity for our plasma gas

$$k = k_0 T^{5/2},$$

36

where the electron temperature is in eV units and the constant

$$k_0 = \frac{3.10275 \times 10^4}{ln\Lambda} \left(\frac{\delta}{\bar{\bar{Z}}} \right)$$

has the units of $J/(s \cdot m \cdot eV^{7/2})$, then the heat flux has the units of $J/(s \cdot m^2)$. Here $\bar{Z}$ is the average charge state of the ions, the Spitzer-Harm coefficient δ depends on $\bar{Z}$: $\delta = 1$, 1.582, 2.28, 3.515, and 4.444, for $\bar{Z} = 1$, 2, 4, 16, and ∞, respectively, and $ln\Lambda \sim 10$.

We apply this equation at each time step in our code and Fig. 2.18 shows the average pressure of the PLX 1 liner (setup is from [4]) with and without the thermal conduction. The mesh size is 0.2 mm with flow through boundary condition for right side and Neumann boundary for left side. We conclude that the thermal conduction has negligibly small effect in the low-energy PLX regime.
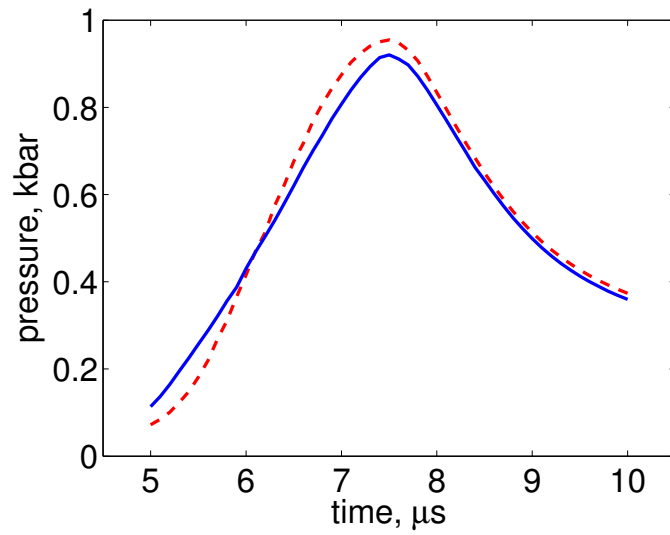
Figure 2.18: (Joint work with H. Kim) Distribution of average pressure of the PLX1 liner without thermal conduction (blue solid line) and with thermal conduction (red dashed line) at the moment of stagnation.

Chapter 3

Plasma jet Merger and Formation of Plasma Liners

In this chapter we focus on the internal structure and self-collapse of 3-dimensional argon liner formed by the merger of high Mach number argon plasma jets using FronTier code. By including 3-dimensional factors contributing to the degradation of liners, we obtain more accurate results instead of only the upper limit values, such as maximum pressure. In order to describe the process more precisely, we apply the plasma EOS for argon with multiple ionization levels [10].

3.1   Propagation of High Mach Number Plasma Jets

The PLX experiment planned to merge 30 high-density argon jets in the Mach number range of 10 - 35 and demonstrate the liner formation and its self-implosion. All the following initial data are based on this experiment. Here we use the code features of solving the Riemann problem in 3-dimensional

space and applying plasma EOS model. First, we perform the simulation of the propagation of a single detached argon jet from the nozzle of the plasma gun to the merging radius. The main purpose is to find the distribution of density, pressure and velocity in the plasma jet before the merger as the input data for 3-dimensional jet-merger simulations to save time. We use the following initial conditions for our simulations: velocity 50 km/s, density $\rho = 5.747 \times 10^{-6}$ g/cm^3, and temperature $T = 1$ eV (see PLX case 6 of Table 2 in [4]). The ambient vacuum is modeled as rarefied gas with density $\rho_0 \sim 10^{-9}$ g/cm^3 and pressure $\sim 10^{-6}$ bar. The mesh size is 4 mm with reflecting boundary for left side and flow through boundary conditions for other sides. We assume that the jet remains axially symmetric (2-dimensional cylindrically symmetric) during the expansion which is another way to save time.

Fig. 3.1 presents the distribution of the initial density and the density at $t = 18.5$ μs or at 0.925 m distance from the plasma gun nozzle in the single jet. Fig. 3.2 shows the profiles of density, pressure, temperature and average ionization in the transverse direction through the jet center at different times (ms). From the profiles, we find that all quantities decrease in time and the jet boundary becomes diffuse very quickly.

The jet expansion can also be estimated analytically. Here we define the jet radius as the location of points with the density of $0.1\rho_0$ to make the result more reasonable. The liner expansion model with constant initial sound speed shows the jet radius d as $d(r_m) = d_0 + c_0(r_c - r_m)/u_j$. Here d_0 is the initial jet radius, c_0 is the initial sound speed, r_c is the chamber radius, and r_m is the

(a) t = 0.0 ms   (b) t = 0.0185 ms
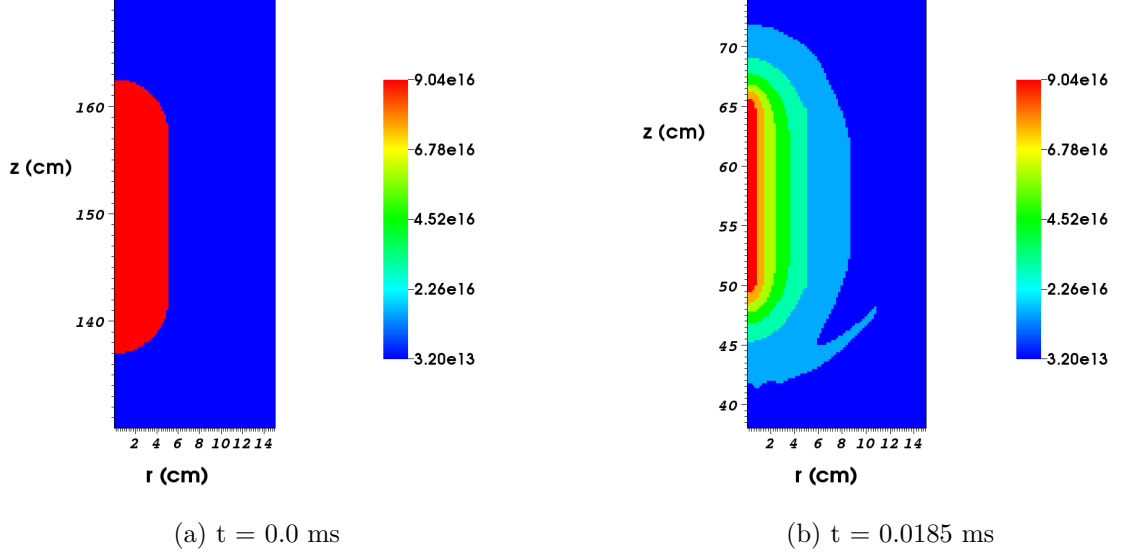
Figure 3.1: (Joint work with H. Kim) Density $(1/cm^3)$ of the detached jet. (a) initial density; (b) density before merging radius.

merging radius [2].

Assume that the jet expands adiabatically with the decrease of the sound speed during the expansion, we obtain an improved model (see details in our paper [10]):

$$c(t) = \sqrt{\gamma \frac{P(t)}{\rho(t)}} = \sqrt{\gamma A \rho(t)^{\gamma-1}},$$

where $P = A\rho^\gamma$ is the adiabatic relation with A as a constant. We then obtain two kinds of models as follows: For the jet length that is much larger than the diameter, we obtain long jet

$$b(t) = b_0 + c_0 \left(\frac{b_0}{b(t)} \right)^{(\gamma-1)} t$$

And for the jet length that is similar to the diameter, we obtain short jet with

41
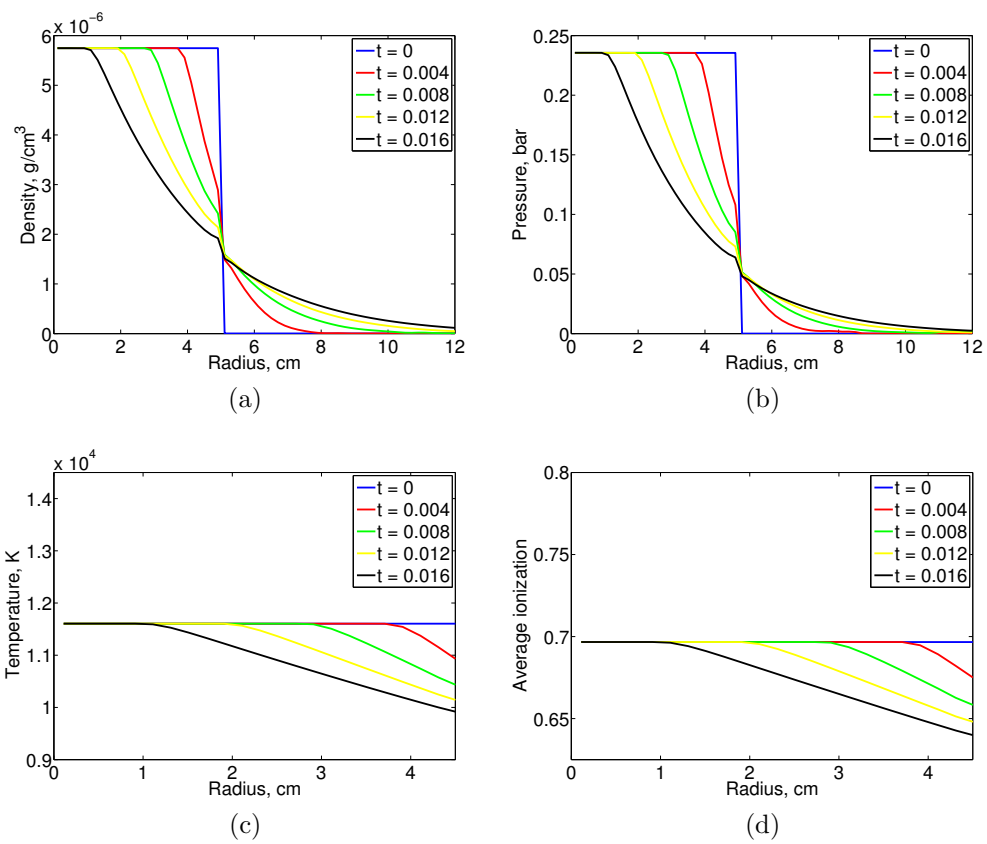
Figure 3.2: (Joint work with H. Kim) Density, pressure, temperature and average ionization across the center of the detached argon jet.

spherical expansion

$$b(t) = b_0 + c_0 \left(\frac{b_0}{b(t)} \right)^{\frac{3}{2}(\gamma - 1)} t$$

Suppose $\gamma = 5/3$, the nonlinear equation for a long cylindrical jet is

$$[b(t)]^{2/3} (b(t) - b_0) = c_0 b_0^{2/3} t \qquad (3.1)$$

and the equation for a short spherical jet is

$$[b(t)]^2 - b_0 b(t) - c_0 b_0 t = 0 \qquad (3.2)$$

In order to compare this theory with our results, we use local gamma $\gamma = 1.14$ for simulations using argon plasma EOS. Then we obtain numerical solution for jet radius based on the nonlinear equations. Fig. 3.3 depicts the evolution of the expanding jet radius from simulation and analytic model with good fitting.

As we mentioned in the scaling law section, Mach number plays an important role in the self-implosion pressures or target compression rates. The higher value of the Mach number, the higher pressures we obtain. Therefore we pay attention to the Mach number change during the jet expansion, which is adiabatic cooling process. Before showing the result, need to justify our method of data selection We know that during expansion, a very strong rarefaction wave exists at the tail of the detached jet. But if we include the jet tail data to find the average Mach number, large values of the Mach number caused by rarefaction wave in vacuum behind the jet tail will significantly affect the average Mach number. Therefore we decide to only take care of
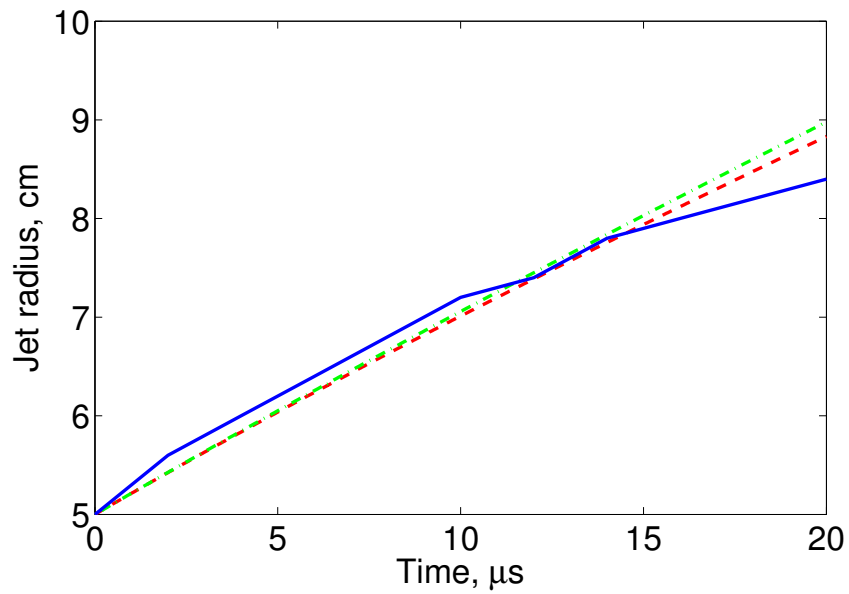
Figure 3.3: (Joint work with H. Kim) Jet expansion comparison of numerical simulation result (blue solid line), analytic model of long jet (green dash-dotted), and analytic model of short jet (red dashed line).
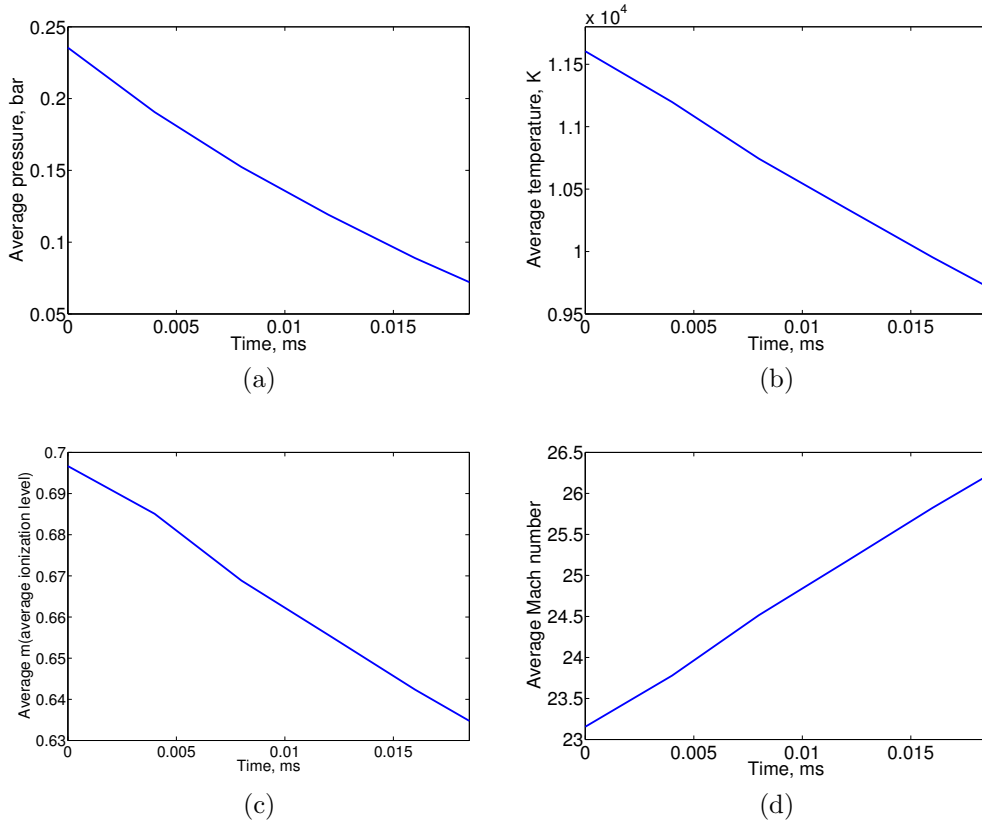
Figure 3.4: (Joint work with H. Kim) Average values of pressure, temperature, m (average ionization) and Mach number of a detached argon jet.

the front half of the jet body when we calculate the average Mach number. Fig. 3.4 depicts the jet cooling process during expansion. The average Mach number increases as time goes by with the maximum value of 26 while at the mean time the average temperature decreases with time. Besides of that, the increase of the jet length slightly increases the average Mach number after the expansion.

3.2 Plasma Jet Merger and Oblique Shock Waves

After obtaining the profiles for the single jet before the merger, we first find directions for 30 jets uniformly distributed in space and then initialize states around each direction based on pressure, density, and velocity profiles from single jet simulation. The mesh size is 4 mm with flow through boundary conditions. We use Spherical Centroidal Voronoi Tessellation (SCVT) to find the uniform distribution of 30 points on a unit sphere, which finds the directions for 30 jets. This problem can be solved using the software by John Burkardt [27] based on Qiang Du's algorithm [28]. We perform transformation from 2-dimensional cylindrical coordinate into 3-dimensional Cartesian coordinate together with bi-linear interpolation, which initializes the states around each jet direction.

Before showing the plasma jet merger with oblique shock waves, we first justify the fluid dynamics process. We argue that the jets cannot interpenetrate each other and change their direction via the oblique shock waves when they merge together. We evaluate the mean free path of ions (The angle between each pair of argon jets is approximately 36°) [29] as:

$$\lambda_i = v_{Ti}/\nu_i, \tag{3.3}$$

where the ion thermal velocity $v_{Ti} = 9.79 \times 10^5 \mu^{-1/2} T_i^{1/2}$ cm/s, and the ion collision rate $\nu_i = 4.80 \times 10^{-8} Z^4 \mu^{-1/2} n_i T_i^{-3/2} \ln \Lambda \, 1/s$. By applying the following states of the jet edge from the simulation: $\mu = m_i/m_p = 40$, $Z \sim 1$, $\ln \Lambda \sim 10$, $n_i = 1.5 \times 10^{16} \, 1/cm^3$, $T_i = 0.86$ eV, we obtain $v_{Ti} = 1.44 \times 10^5$

cm/s, $\nu_i = 1.43 \times 10^9$ 1/s, and thus $\lambda_i \sim 1 \times 10^{-4}$ cm. Then the conclusion is the edge of the jet is fully collisional and the mean free path in the jet center is even shorter [10]. For the jet merger, we apply the slowing down rate in [29].

$$\frac{dv_\alpha}{dt} = -\nu_s^{\alpha \backslash \beta} v_\alpha \tag{3.4}$$

where $\nu_s^{\alpha \backslash \beta} = (1 + m_\alpha/m_\beta) \phi(x^{\alpha \backslash \beta}) \nu_0^{\alpha \backslash \beta}$, $\nu_0^{\alpha \backslash \beta} = 4\pi n_\beta e_\alpha^2 e_\beta^2 \lambda_{\alpha\beta}/m_\alpha^2 v_\alpha^3$, $x^{\alpha \backslash \beta} = m_\beta v_\alpha^2/2kT_\beta$, and $\phi(x) = \frac{2}{\sqrt{\pi}} \int_0^x t^{1/2} e^{-t} dt$. By applying the parameters in the jet edge and $\lambda_{\alpha\beta} \sim 10$, integrating numerically the equation, we find that after around 0.5 cm, the ion's initial penetrating velocity 3.1×10^6 cm/s is slowed down to thermal velocity. Based on the analysis, electrons are indeed highly collisional with the electrostatic interaction reducing the ion penetration, we justify what we argued (see details in our paper [10]).

We believe that the jets merger process is accomplished through a cascade of oblique shock waves which heat the liner, reduce Mach number and cause the non-uniformity of the liner. Fig. 3.5, Fig. 3.6 and Fig. 3.7 depict density, pressure and average ionization contours before and after merger. Fig. 3.8a shows the distribution of density states on a plane slicing containing the origin and axes of the neighboring three jets to give a better overall picture. Due to oblique shock waves, we observe that the highest pressure appears along the plane of interaction of the neighboring jets while at the initial merge stage the highest density is in the main body of jet and shifts to middle between jet axes at later stages. There is also an interesting phenomenon observed in [30], that is, the formation of high pressure contours having shapes of the pentagon and hexagon, determined by the number of jet closest neighbors.

Fig. 3.9 shows the distribution of density and pressure on a 10 cm radius spherical slice through the leading edge of the 3-dimensional liner. This plot shows the post-shock regions formed by three-jet interactions. It also gives us the shapes of the pentagon and hexagon as we mentioned before. Fig. 3.8b presents the schematic of oblique shocks. Here δ means the angle between the plasma jet and the plane of reflection (the median line between two jets), and α is the angle of the oblique shock wave. As we mentioned, the angle between each pair of argon jets is approximately 36°, the collision of jets is equivalent to the collision of a jet with a solid wall at 18° angle. We then apply the standard theory of oblique shock waves for states in the after-shock region. The states are calculated by following equations [31]: Here we assume non-expanding flow (with parallel stream lines) has polytropic gas properties initially, $\gamma = 5/3$, and α, P, ρ, T, M stand for oblique shock wave's angle, pressure, density, temperature, Mach number respectively.

$$\frac{\tan(\alpha - \delta)}{\tan \alpha} = \frac{2 + (\gamma - 1)M_1^2 \sin^2 \alpha}{(\gamma + 1)M_1^2 \sin^2 \alpha} \tag{3.5}$$

$$\frac{P_2}{P_1} = \frac{2\gamma M_1^2 \sin^2 \alpha - (\gamma - 1)}{\gamma + 1} \tag{3.6}$$

$$\frac{\rho_2}{\rho_1} = \frac{(\gamma + 1)M_1^2 \sin^2 \alpha}{(\gamma - 1)M_1^2 \sin^2 \alpha + 2} \tag{3.7}$$

$$\frac{T_2}{T_1} = \frac{[2\gamma M_1^2 \sin^2 \alpha - (\gamma - 1)][(\gamma - 1)M_1^2 \sin^2 \alpha + 2]}{(\gamma + 1)^2 M_1^2 \sin^2 \alpha} \tag{3.8}$$

(a) t = 0.0203 ms

(b) t = 0.0223 ms

(c) t = 0.0243 ms

(d) t = 0.0263 ms
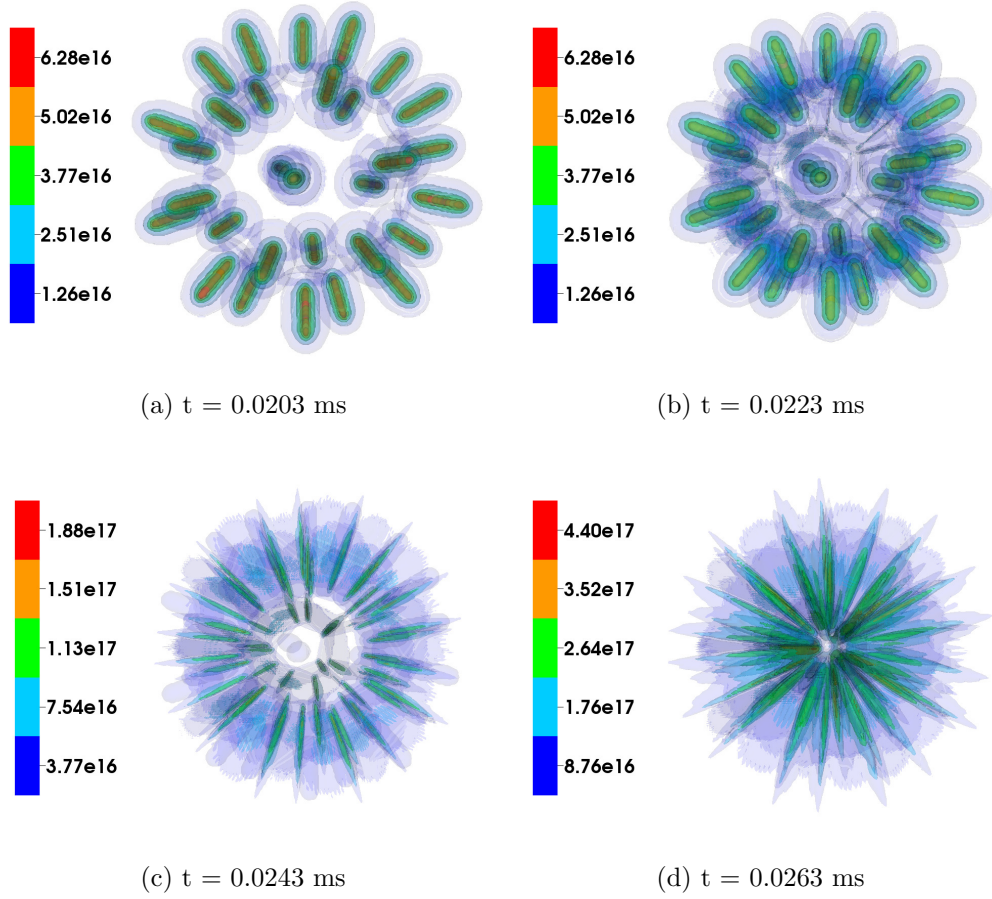
Figure 3.5: (Joint work with H. Kim) Density $(1/cm^3)$ contours before merger (a, b) and after merger (c, d) of 30 argon plasma jets.

$$M_2^2 \sin^2(\alpha - \delta) = \frac{(\gamma - 1)M_1^2 \sin^2 \alpha + 2}{2\gamma M_1^2 \sin^2 \alpha - (\gamma - 1)} \tag{3.9}$$

where quantities with the index 1 describe the pre-shock state and the corresponding quantities with index 2 describe the post-shock state.

Here we apply a 2-dimensional simulation to show the merger of polytropic gas jets and compare the results with the oblique shock theory to obtain

(a) t = 0.0203 ms   (b) t = 0.0223 ms

(c) t = 0.0243 ms   (d) t = 0.0263 ms
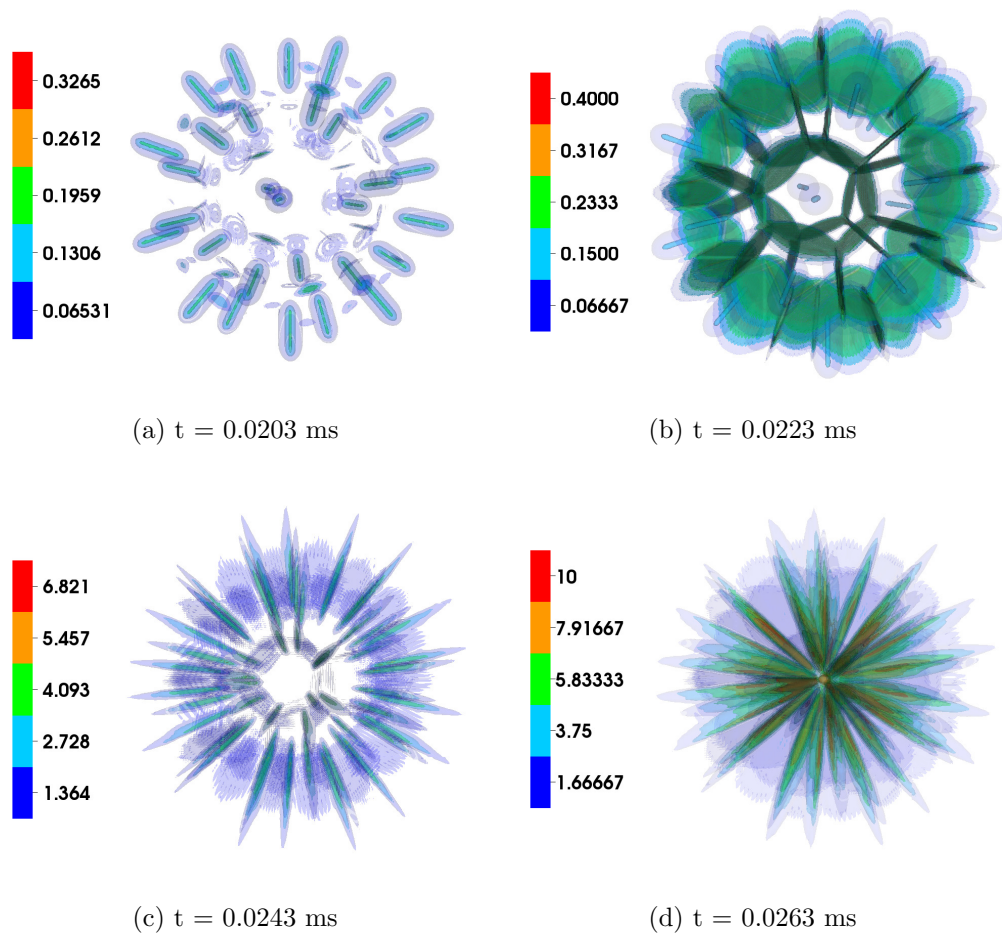
Figure 3.6: (Joint work with H. Kim) Pressure (bar) contours before merger (a, b) and after merger (c, d) of 30 argon plasma jets.

(a) t = 0.0203 ms

(b) t = 0.0223 ms

(c) t = 0.0243 ms

(d) t = 0.0263 ms
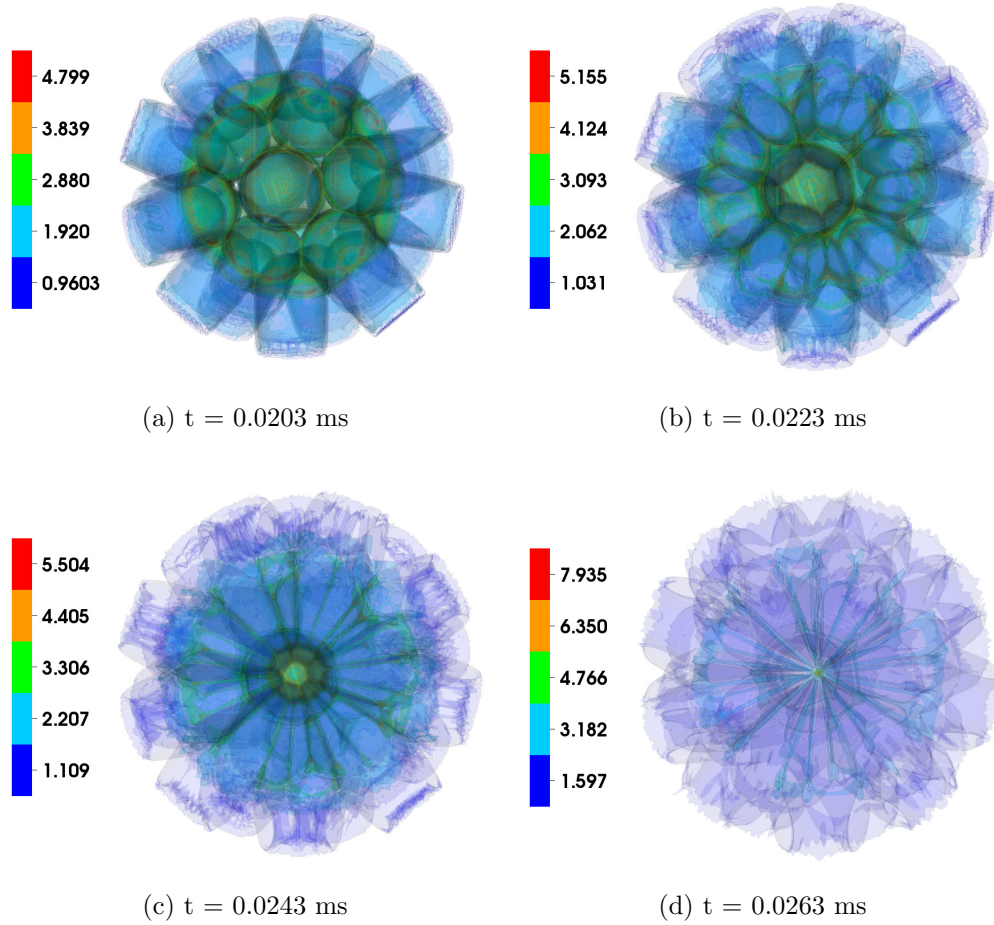
Figure 3.7: (Joint work with H. Kim) Average ionization contours before merger (a, b) and after merger (c, d) of 30 argon plasma jets.

(a)   (b)
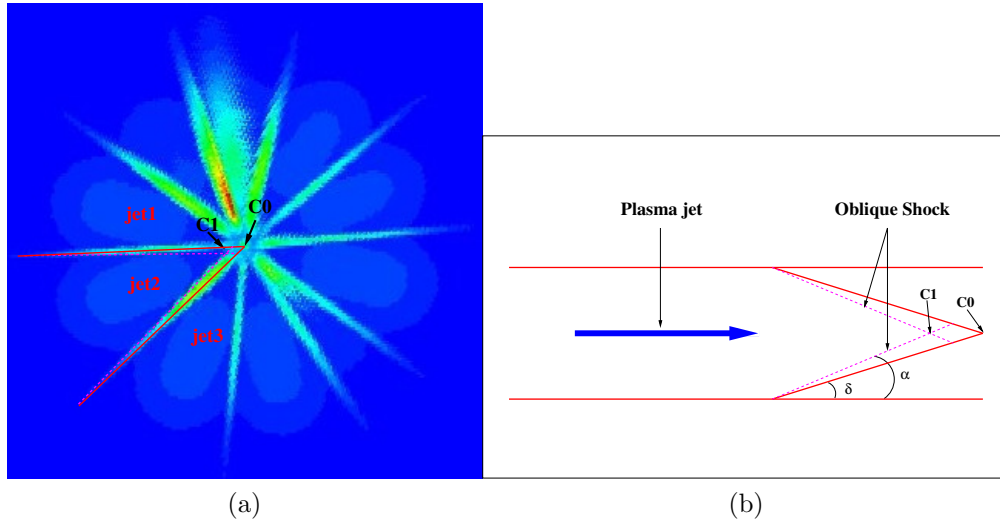
Figure 3.8: (Joint work with H. Kim) (a) Density distribution on a slice of 3-dimensional data at stagnation and (b) schematic of oblique shocks in the jets merger process.

(a) Number density, $1/cm^3$ (b) Pressure, bar
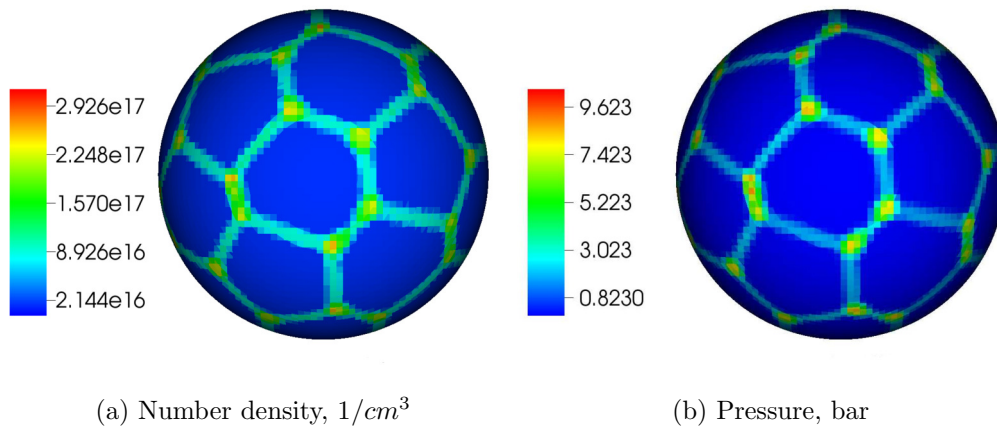
Figure 3.9: (Joint work with H. Kim) Distribution of density and pressure on a 10 cm radius spherical slice of 3-dimensional liner data when t = 0.0253 ms.

a better understanding [10] since 3-dimensional merger is too complicated by (a) secondary shocks due to three-jet interactions, (b) spreading out of free jets in all directions, (c) change of the ionization fraction across the oblique shock wave, and (d) heating associated with the adiabatic compression. We use the code feature of solving the Riemann problem. The initial pressure and density are uniformly distributed with sharp boundaries (non-expanding jets before the merger) in these idealized 2-dimensional simulations. The angle between two jets is set according to the angle in the 3-dimensional jets array. The mesh size is 4 mm with flow through boundary conditions. The process is shown in Fig. 3.10 describing the initialization and density distribution with first and second cascades of oblique shock waves at later time. Fig. 3.11 depicts profiles of pressure, density, and Mach number after the first oblique shock waves. Based on the results from Table 3.1, a good agreement between simulated values of pressure, density, Mach number and other quantities in the first post-shock region and related theory with solutions to the nonlinear system of oblique shock equations is obtained. Since the theory talks about steady-state oblique shock while the simulation didn't reach the steady state before the second oblique shock followed, there is small discrepancy between these two.

	α	M_2	ρ_2/ρ_1	T_2/T_1	P_2/P_1
Theory	24.8	3.9	3.9	35	137
Simulation	23.5	4.0	3.5	35	135

Table 3.1: (Joint work with H. Kim) Comparison of simulations and theory of states in the first oblique shock wave.
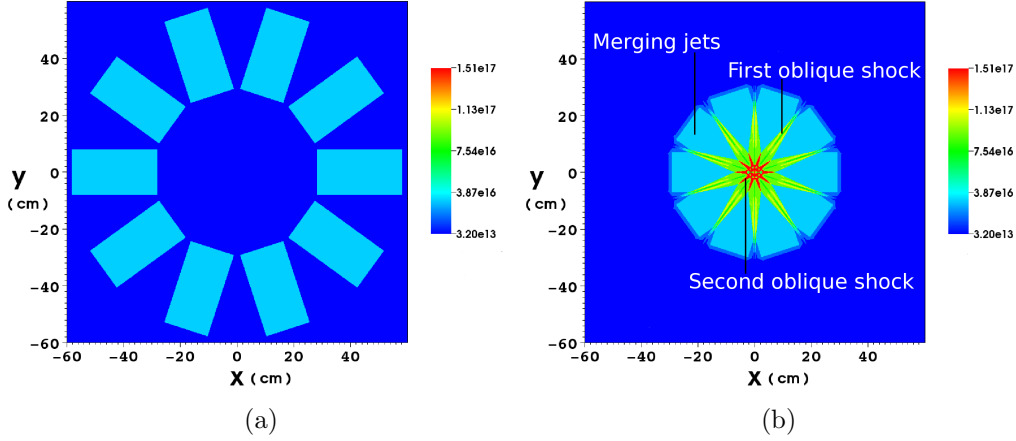
Figure 3.10: (Joint work with H. Kim) (a) Initial density of the 2-dimensional jet merger simulation and (b) density distribution showing the first and second cascades of oblique shocks $(1/cm^2)$.

Next we analyze the second oblique shock wave. The angle between converging flow remains $36°$ since the flow velocity is parallel to the mid-plane after first shock wave. The collision of flows generates the secondary oblique shock wave which is again equivalent to collision of a jet with a solid wall at $18°$ angle. Fig. 3.12 shows the distribution of states in the post-shock region and similar comparison of theory and simulation is shown in Table 3.2. We believe that the cascades of oblique shock waves would continue until the chamber center is reached with a hammer-shock (a shock acting like a hammer hits the wall). But the third one was almost invisible due to the residual vacuum gas and the expansion of the jets. In general terms, we achieved a good agreement with theory on post-shock states after the first and second oblique shocks.

(a) Number density, $1/cm^2$

(b) Pressure, bar
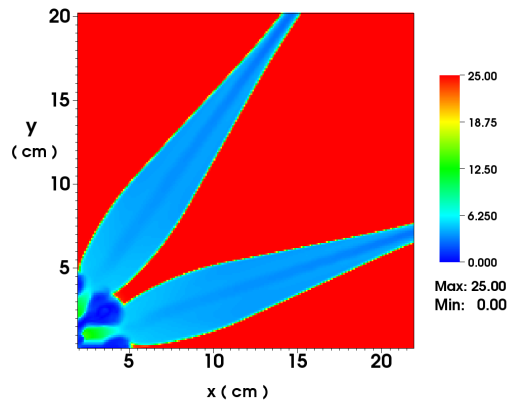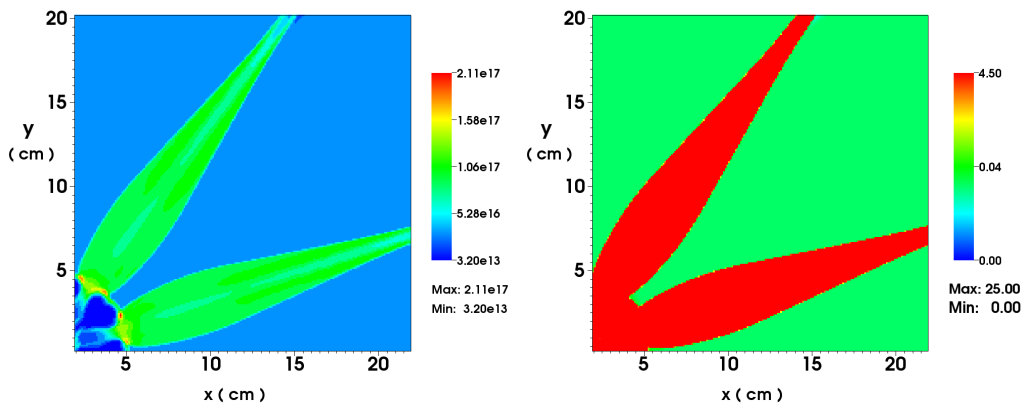
(c) Mach number

Figure 3.11: (Joint work with H. Kim) First cascade of oblique shock waves in 2-dimensional jet merger simulation.
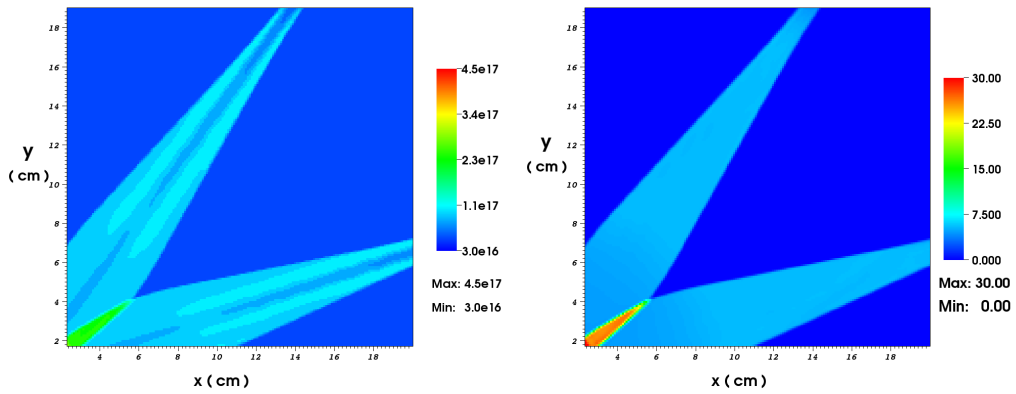
(a) Number density, $1/cm^2$

(b) Pressure, bar
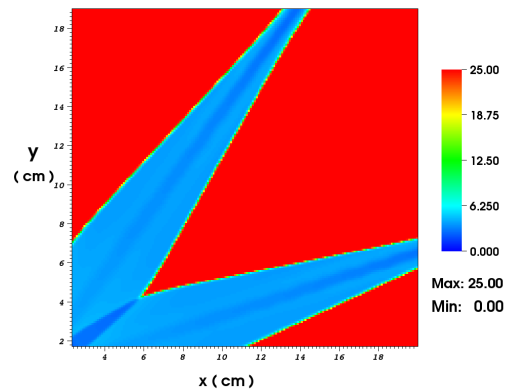
(c) Mach number

Figure 3.12: (Joint work with H. Kim) Second cascade of oblique shock waves in 2-dimensional jet merger simulation.

	α	M_2	ρ_2/ρ_1	T_2/T_1	P_2/P_1
Theory	33	2.3	2.4	2.3	5.6
Simulation	30	2.4	2.5	2.3	5.3

Table 3.2: (Joint work with H. Kim) Comparison of simulations and theory of states in the second oblique shock wave.

## 3.3   Simulation of LANL Plasma Liner Experiments

In this section we first analyze the 3-dimensional simulation results compared with 1-dimensional spherical simulations and simulations in [4] and [6]. We average the 3-dimensional properties in radial coordinates at the merging radius and compare with the corresponding 1-dimensional simulations with same amount of mass, pressure and density [10]. Fig. 3.13 presents the evolution of the averaged Mach number in the 3-dimensional and 1-dimensional space. Because of the expansion of the detached jets, we obtain higher initial value of the average Mach number of 3-dimensional liner. After the merger process, the Mach number of the 3-dimensional liner decreases faster compared with the 1-dimensional liner, reaching values of 14.4 (3-dimensional) and 19.5 (1-dimensional).

Fig. 3.14 shows the average density and pressure of the 3-dimensional liner at stagnation in radial direction, those of the 1-dimensional liner with the same profile as the 3-dimensional liner at the merging radius, and those of the 1-dimensional liner with the same mass but sharp profile at the merging radius. We find that the self-collapse pressure of the 3-dimensional liner is 6.4 kbar, the pressure of the equivalent 1-dimensional liner is 64 kbar (10 times
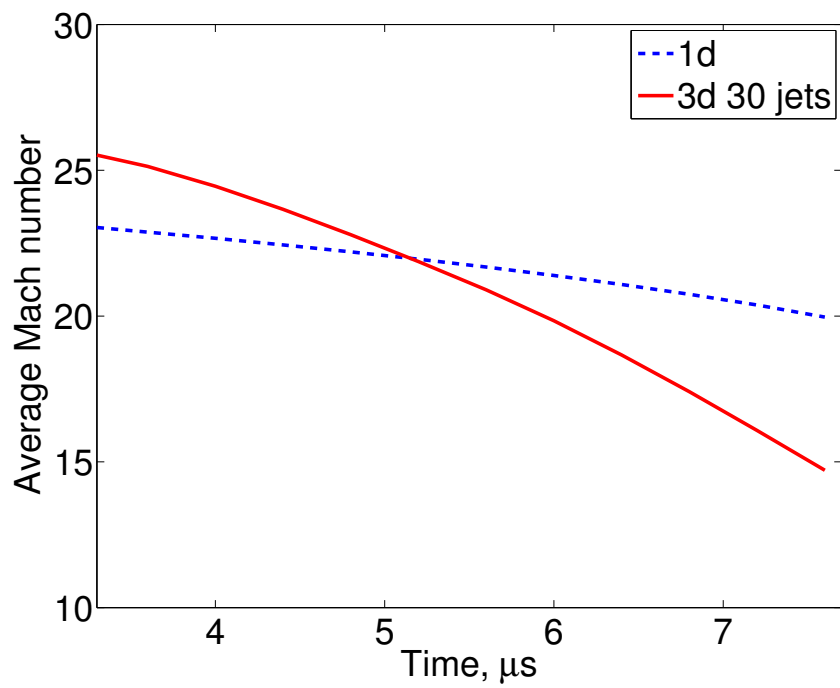
Figure 3.13: (Joint work with H. Kim) Evolution of average Mach numbers of 1-dimensional and 3-dimensional liners.

smaller), while the pressure of 1-dimensional liner with the sharp profile at the merging radius is 320 kb (50 times smaller). We believe that the oblique shock waves reduce the liner Mach number and the self-implosion pressures. As a result of this and other factors, the self-collapse pressures of uniform liners (1-dimensional) significantly exceed pressure values achievable in liners formed by the jet merger (3-dimensional). The result contradicts [6] which says that the self-collapse pressure of the 3-dimensional liner formed by the merger of 30 jets are same as that of 1-dimensional spherically symmetric liner. Here in our simulations we apply plasma EOS in the vacuum region with energy sinks to mitigation the effect caused by liner compressing residual vacuum gas with eliminating artificially high pressure in the vacuum region. By using plasma EOS for the residual gas with initial pressure of 1 mTorr and liner with parameters of PLX Table 2, case 6 of [4], we obtain 30 times higher self-implosion pressure compared with using polytropic gas EOS.

Since we perform 3-dimensional simulation with the domain size as $(160\ cm)^3$ and the mesh size as $(400)^3$, we would like to comment on the numerical resolution and convergence to ensure accuracy. Fig. 3.15 shows the convergence of the averaged Mach number on meshes with different resolution using polytropic EOS. The result also shows that the mesh size of 0.4 cm is enough for 3-dimensional self-collapse simulations.

Finally note that the number of jets (30) used in our simulations is due to the current experimental equipment instead of optimization considerations. If we use more jets, the effect of oblique shock waves will be reduced while the merging radius and the convergence time of the merged liner will be increased.

59

(a)   (b)
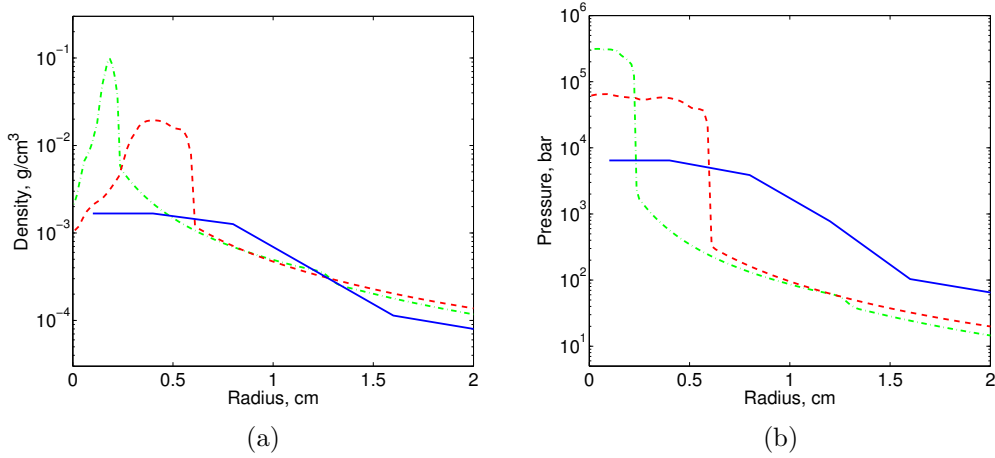
Figure 3.14: (Joint work with H. Kim) Distribution of density (a) and pressure (b) during stagnation of the 3-dimensional liner averaged in radial coordinates (solid blue line), the 1-dimensional liner initialized with sharp profile at the merging radius (green dash-dotted line) and the 1-dimensional liner initialized with same profile as the 3-dimensional liner at the merging radius (red dashed line).

In recent time, PLX group in Los Alamos National Lab (LANL) reported experiment results of single argon plasma jet propagation and two jets merger. [5, 32, 33]. We perform these simulations using FronTier code and compare the results. The initialization of propagation of a 2-dimensional cylindrically symmetric simulation for a single argon jet is based on Table II in [5]. The initial conditions are $\rho = 1.327 \times 10^{-6}$ $g/cm^3 = 2 \times 10^{16}$ $1/cm^3$, velocity $V = 30$ km/s and temperature $T = 1.4$ eV. The mesh size is 4 mm with reflecting boundary for left side and flow through boundary conditions for other sides. Fig. 3.16a and Fig. 3.16b present the initial density profile and profile after 0.0125ms which is used for initialization of two jets merge later. Fig. 3.17a shows the average density profile over radial direction on the jet's

60
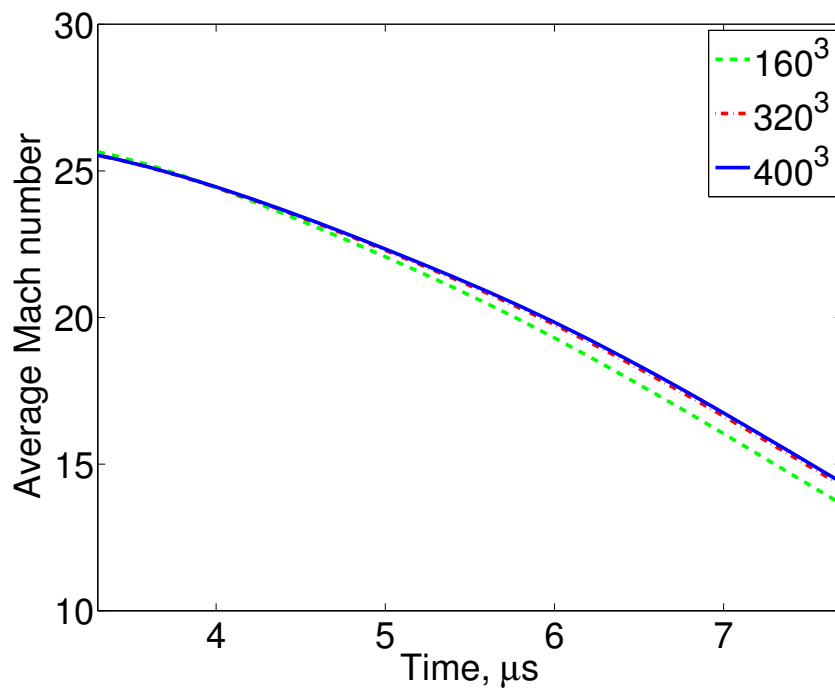
Figure 3.15: (Joint work with H. Kim) Mesh convergence studies of 3-dimensional liner formation and implosion simulation. Evolution of average Mach number using three different mesh sizes is shown.
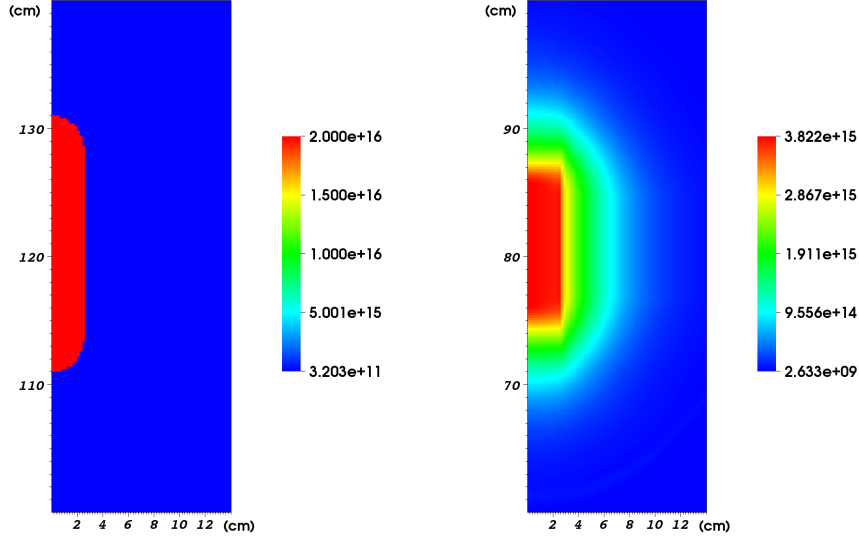
Figure 3.16: (Joint work with H. Kim) Density $(1/cm^3)$ of the detached jet. (a) initial density; (b) density before merging radius.

axial direction which is comparable with Figure 11 in [5]. Fig. 3.17b presents density profile on radial direction which is also consistent with the experiment results in [5].

For two plasma jets merger simulation, we perform both 2-dimensional and 3-dimensional simulations with domain $x \times y$ as $[-20 \ cm, \ 100 \ cm] \times [-35 \ cm, \ 35 \ cm]$ and $x \times y \times z$ as $[-10 \ cm, \ 90 \ cm] \times [-30 \ cm, \ 30 \ cm] \times [-30 \ cm, \ 30 \ cm]$ respectively and the mesh size of $0.4 \ cm$ in each direction based on the subspace of experiment chamber and jet merger angle of $24°$ in [5] with flow through boundary conditions. Fig. 3.18b and Fig. 3.19b show the merger after around $90 \ cm$ propagation from the chamber wall. We observe the two layers structure as in [32, 33] with the distance around $3.5 \ cm$.
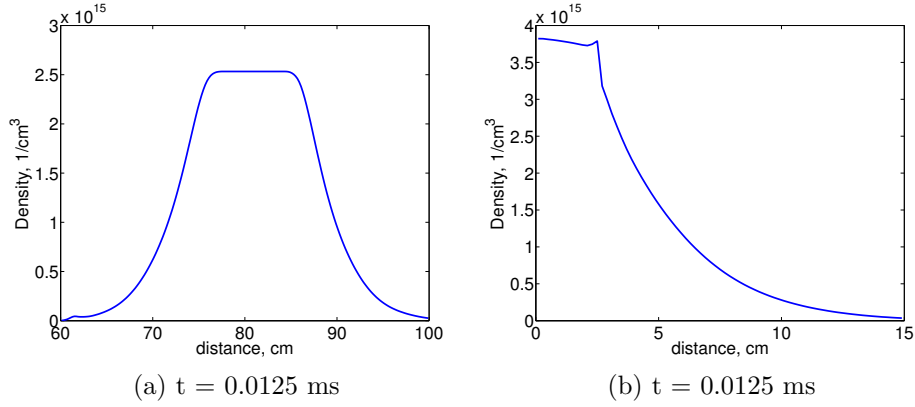
Figure 3.17: (Joint work with H. Kim) Density of the detached jet. (a) average number density ($1/cm^3$) over raial direction on the jet's axial direction; (b) density profile ($1/cm^3$) on the radial direction of jet.

Fig. 3.20 shows argon atom density and free electron density along the line of $x = 17\ cm$ and y from -15 cm to 15 cm for 2-dimensional case and $x = 17\ cm$, $y = 0\ cm$ and z from -15 cm to 15 cm for 3-dimensional case and we choose the positions of $\sim 12\ cm$ and $\sim 18\ cm$ as each jet's center without passing oblique shock waves. The density difference across the oblique shock wave is around one order of magnitude which is consistent with the theoretical values and the experimental observation in [32, 33]. The results are not consistent with contents in their recent published paper [13], we will investigate this further in our future study. The absolute density values in the 3-dimensional simulation is approximately 3 times lower than those of 2-dimensional simulation which is caused by the expansion in 3-dimensional space. Table 3.3 shows comparison between simulation works and the oblique shock wave theory (see details in [10]). Here we use $\gamma \sim 1.1$ based on γ-law fit in the plasma LTE EOS, initial Mach number ($M_1 \sim 14$) and corner angle ($\delta = 12°$). As 2-dimensional and

3-dimensional simulations share local gamma value, initial Mach number, and the interaction angle, the overall dynamics of oblique shock waves is very similar with discrepancy because of additional dimension. The difference between simulation results and theory is caused by non-uniform states.

	α	M_2	ρ_2/ρ_1	T_2/T_1	P_2/P_1
Theory	14	11	7.6	1.6	12
2-dimensional	15.5	8.7	7.4	1.8	17
3-dimensional	15.5	9.3	8.8	1.8	22

Table 3.3: (Joint work with H. Kim) Comparison of results from the oblique shock wave theory and simulations of 2-dimensional and 3-dimensional.

Finally, to justify this simulation study, the ion-ion mean free path estimates are calculated for the jet inside and jets merger cases. (3.3) shows the mean free path for single jet. By applying the plasma jet edge's parameters $Z \sim 1$, $\ln \Lambda \sim 10$, $T_i = 0.8$ eV, $n_i = 2.4 \times 10^{14}$ $1/cm^3$, we obtain $v_{Ti} = 1.83 \times 10^5$ cm/s, $\nu_i = 2.5 \times 10^7$ 1/s, and thus $\lambda_i = 5.5 \times 10^{-3}$ cm. This mean free path justifies our single plasma jet propagation study. For the jets merger case, the slowing down of a penetrating ion is calculated in (3.4). By applying the plasma jet edge's states and $\lambda_{\alpha\beta} \sim 10$, the ion's initial penetrating velocity 1.2×10^6 cm/s is slowed down to thermal velocity with distance around 0.7 cm. With highly collisional electrons and electrostatic interaction, we justify two jets merger simulation study.
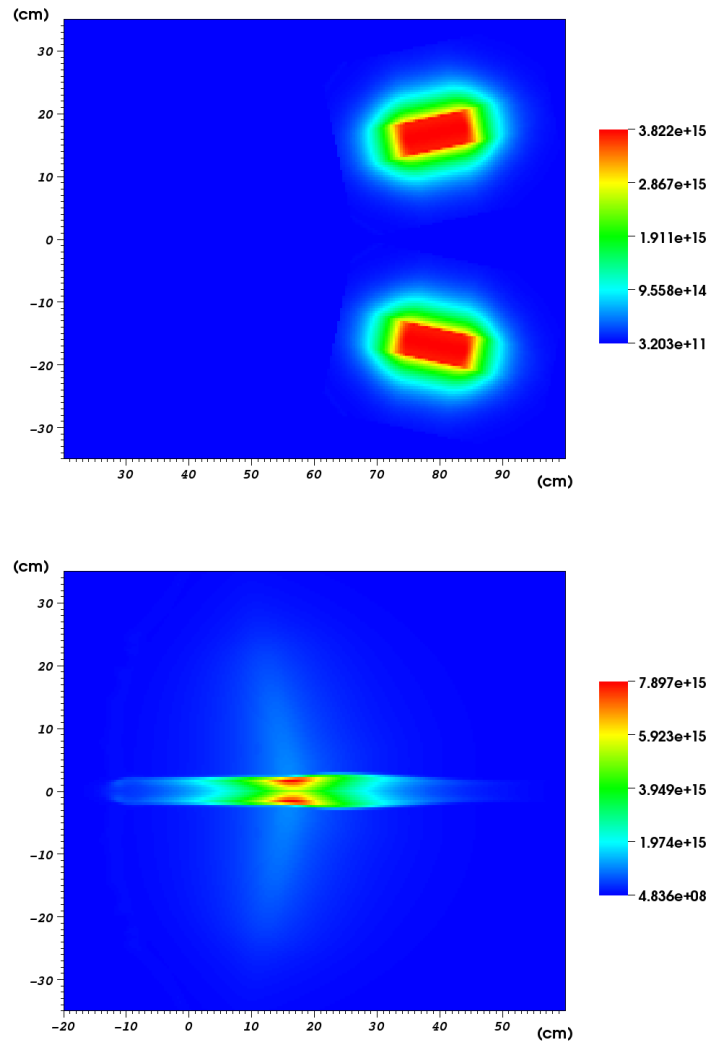
Figure 3.18: (Joint work with H. Kim) (a) 2-dimensional two jets merger simulation initial density profile ($1/cm^3$) using single jet result; (b) 2-dimensional two jets merger density profile ($1/cm^3$) after ~ 90 cm propagation from the chamber wall.
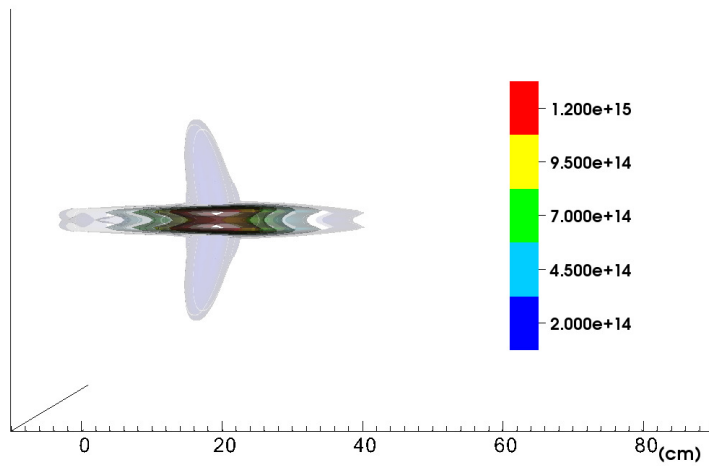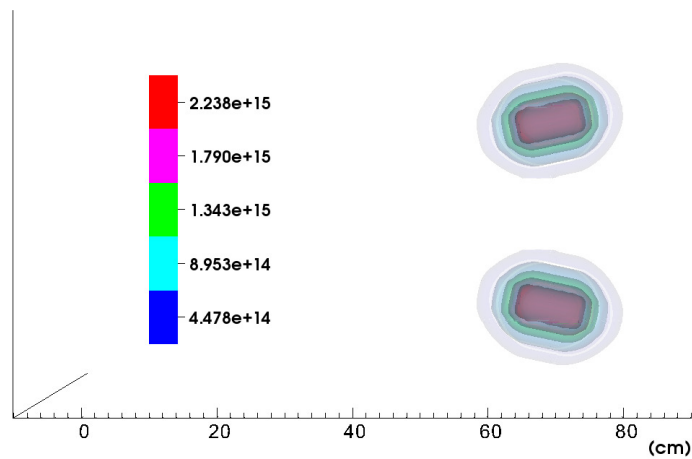
Figure 3.19: (Joint work with H. Kim) (a) 3-dimensional two jets merger simulation initial contour density profile $(1/cm^3)$ using single jet result; (b) 3-dimensional two jets merger contour density profile $(1/cm^3)$ after $\sim 90\ cm$ propagation from the chamber wall.
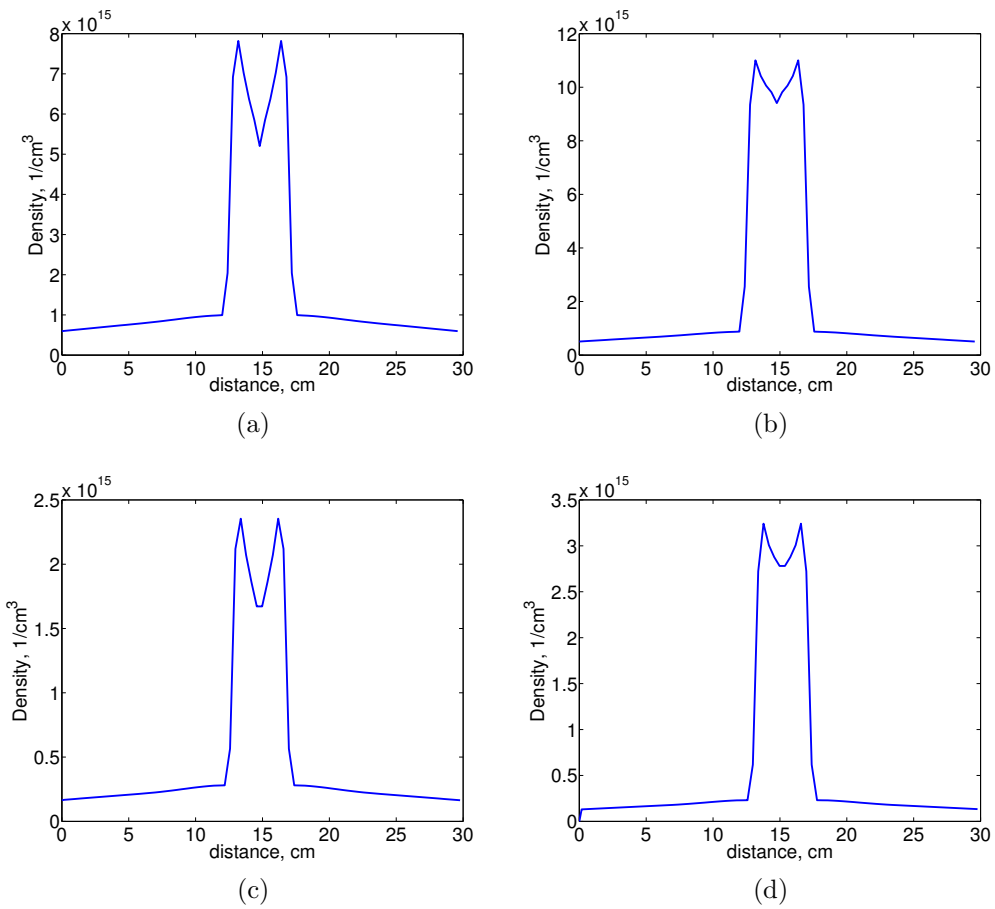
Figure 3.20: (Joint work with H. Kim) 2-dimensional two jets merger transverse argon atom density (a) and electron density (b) profile; 3-dimensional two jets merger transverse argon atom density (c) and electron density (d) profile at the position of $\sim 90\ cm$ from the chamber wall.

Chapter 4

Implosion of Plasma Targets

The final goal of this research area is to reach satisfactory states in the target to achieve ignition conditions using efficient driver power. We have studied the imploding liner (driver power) in detail based on Thio *et al.* [1] suggestion, that is, a spherical array of supersonic plasma jets launched from the periphery of the implosion chamber can be used to create a spherically symmetric plasma liner. In this chapter, we focus on plasma target simulation in higher dimensional spaces.

4.1   Modeling of Liner - Target Interaction

We have discussed 1-dimensional spherical liner-target simulations in chapter 2, especially in section 2.1 about scaling laws. All the liners are spherical symmetric, which means that they are uniform. Uniform liners present an upper limit of maximum pressure and fusion energy. But liners formed by a spherical array of supersonic plasma jets are not uniform anymore. Fig. 3.9 shows the distribution of density and pressure on a 10 cm radius spherical slice

through the leading edge of the 3-dimensional liner. This plot demonstrates non-uniformities of density and pressure in the liner. The effects caused by the non-uniformities are investigated in this chapter.

First we introduce our multi-stage scheme for the simulations in this chapter. Here we take 2-dimensional simulation as an example, steps for 3-dimensional simulation are similar. As in the previous 3-dimensional simulation, we perform the simulation of the propagation of a single detached argon jet from the nozzle of the plasma gun first in order to find the distribution of density, pressure and velocity in the plasma jet before the merger as the input data for 2-dimensional jet-merger simulations to save time. Here we use the code features of solving the Riemann problem, front tracking and applying plasma EOS model. We use 16 jets with following initial conditions: The same initial inner radius and outer radius as in previous simulations, that is, 137.2 cm and 162.7 cm and the same target initial states as in section 2.1, that is density $\rho = 8.3 \times 10^{-6} \, \text{g/cm}^2$, pressure $P = 640.3$ bar to obtain reasonable fusion energy. For the jet, the density $\rho = 3.58 \times 10^{-4} \, \text{g/cm}^2$, pressure $P = 8.37$ bar, velocity $v = 100 \, \text{km/s}$, and the Mach number $M = 60$. The ambient vacuum is modeled as rarefied gas with density $\rho \sim 10^{-9} \, g/cm^2$ and pressure $\sim 10^{-6}$ bar. The mesh size is 2 mm with reflecting boundary for left side and flow through boundary conditions for other sides. As with Fig. 2.4, we performed simulations with different target sizes and found that 10 cm gave the most optimal fusion energy gain. We then chose the target radius as 10 cm. Fig. 4.1 presents the distribution of the initial density and the density at $t = 18.5 \, \mu s$ or at 85 cm distance from the plasma gun nozzle in the single jet.

Note that we place the jet at 92.5 cm instead of 137.2 cm, but let the jet move same distance (85 cm from the nozzle with final position as 7.5 cm instead of 52 cm) to shrink the computational domain.

After obtaining the profiles for the single jet before the merger, we first find directions for 16 jets uniformly distributed in space and then initialize states around each direction based on pressure, density, and velocity profiles from single jet simulation (see Fig. 4.1c). Fig. 4.2 shows density, pressure, Mach number distributions of 16 jets before interacting with the target. The mesh size is 2 mm with flow through boundary conditions.

For 2-dimensional simulation, the final results of compression of the plasma target can be achieved after the previous steps. Here we also per-form another simulation with 2 mm based on 5 mm mesh size. It is designed as follows: We take the data of the center area from simulation iwth the 5 mm mesh size when the liner is still not reaching the target and then do the mesh refinement (2 mm) run. This strategy is applied to 3-dimensional simulation to save computational time and processors to be used. Fig. 4.3 shows the density, pressure and Mach number profiles for simulations with 5 mm mesh size and with 2 mm based on 5 mm mesh size at the time around liner-target interaction. This approach is validated in next part.

Next we present the quantities to analyze our final results. First is the average pressure in the target since the target condition is the most important part and average value makes more sense because of non-uniform states. We summarize all the pressure values in the target and then divide it by the total number to obtain the average value. Second is the fusion energy. The nuclear
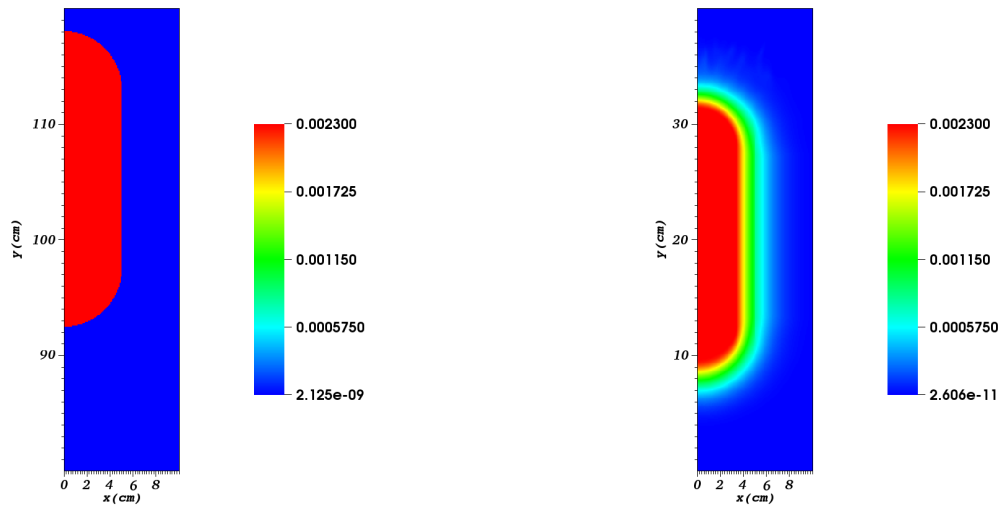
(a) t = 0.0 ms

(b) t = 0.0085 ms
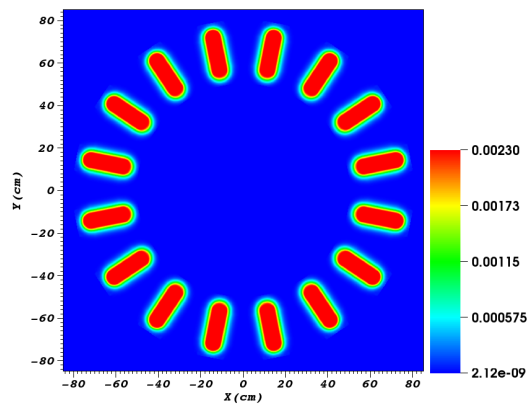
(c)

Figure 4.1: Density (g/cm^3) of the detached jet (a) initial density; (b) density before merging radius. (c) Density distribution of 16 jets.

(a)

(b)

(c)
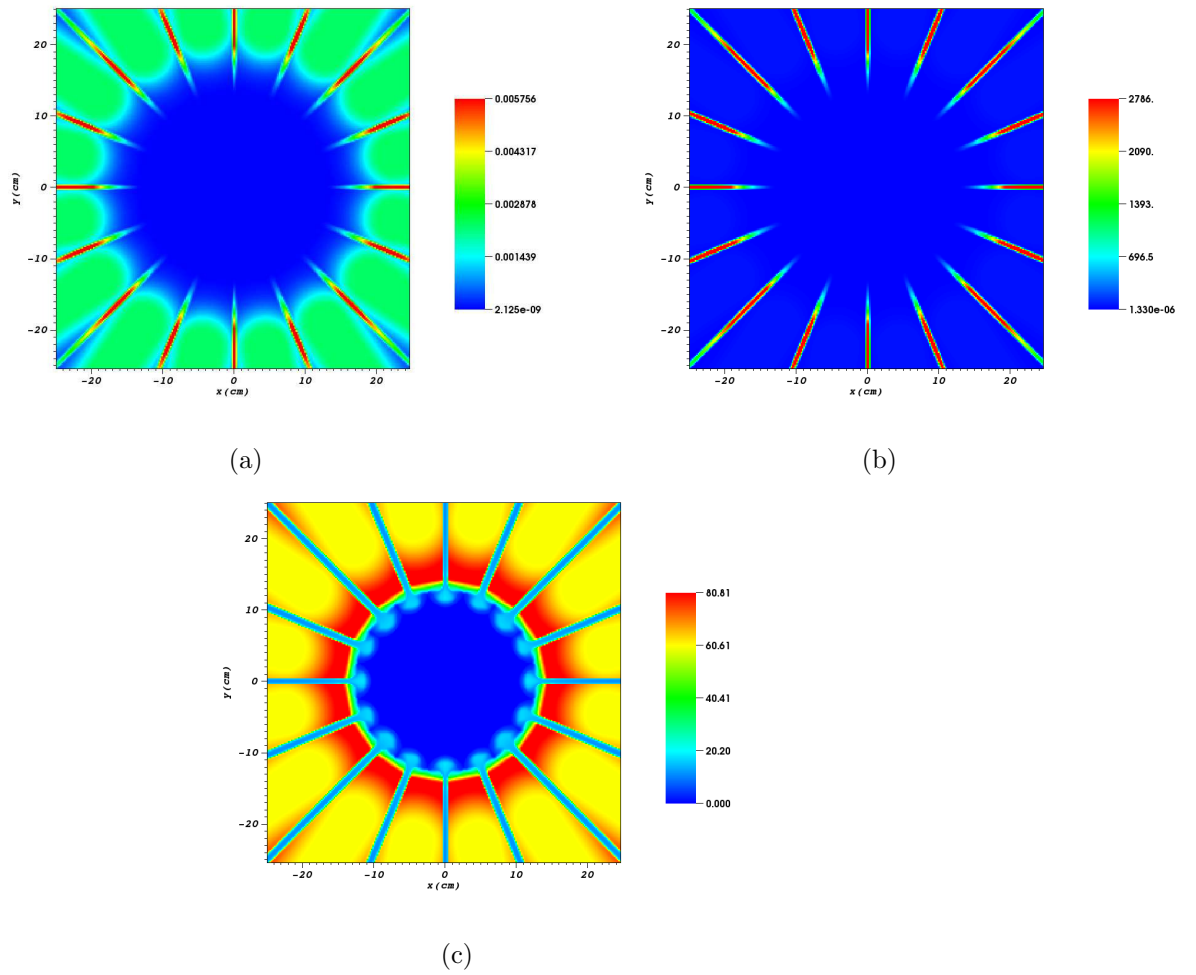
Figure 4.2: Distributions of (a) density (g/cm^3); (b) pressure (bar); (c) Mach number of the 16 jets before interacting with the target.
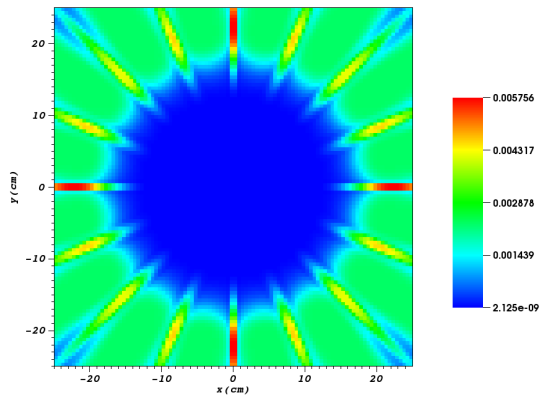
(a) Denisty, g/cm^3
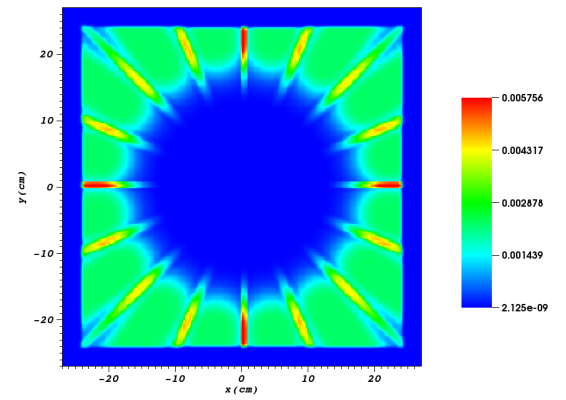
(b) Denisty, g/cm^3
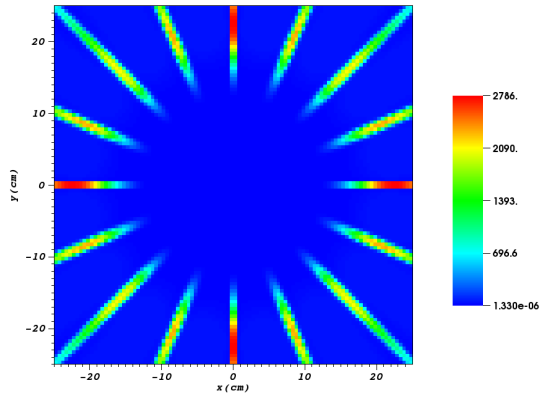
(c) Pressure, bar

(d) Pressure, bar
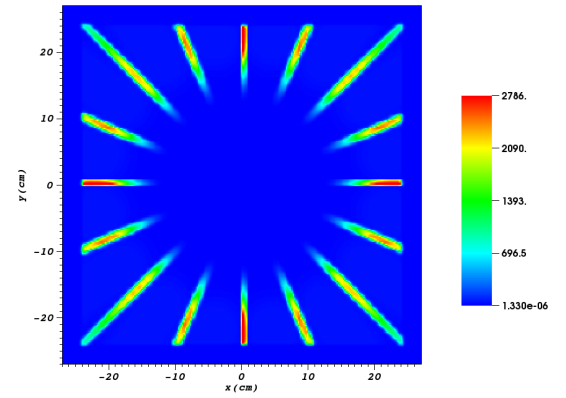
Figure 4.3

(e) Mach number   (f) Mach number
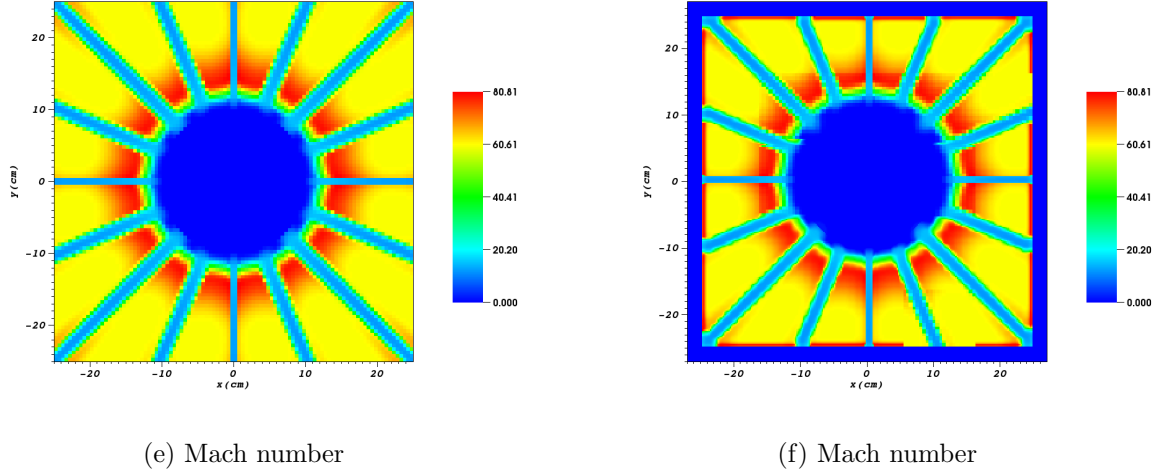
Figure 4.3: Distributions of density, pressure and Mach number for simulations with 5 mm mesh size (left column) and 2 mm based on 5 mm mesh size (right column).

fusion energy obtained in simulations is using similar approach as in section 2.1 [23] with some modifications. We accumulate neutrons at each time step for each computational cell and then convert to fusion energy. Here we choose average pressure to validate our previous idea since fusion energy is quite sensitive. Fig. 4.4 shows the evolution of average pressure in the target for different cases around the time when target breaks into fragments. The reason why we choose this time range is that after breaking up, the behavior of the target becomes quite unstable, which is described in detail later. The average pressure in the target of simulation with 2 mm based on 5 mm mesh size is almost same with the one using 2 mm mesh size directly since compression of target is mainly based on the leading edge of the liner, the main body mainly contributes to the deconfinement time [3]. Now we have validated our modeling of liner-target interaction and we apply it to our later 3-dimensional simulation.

74
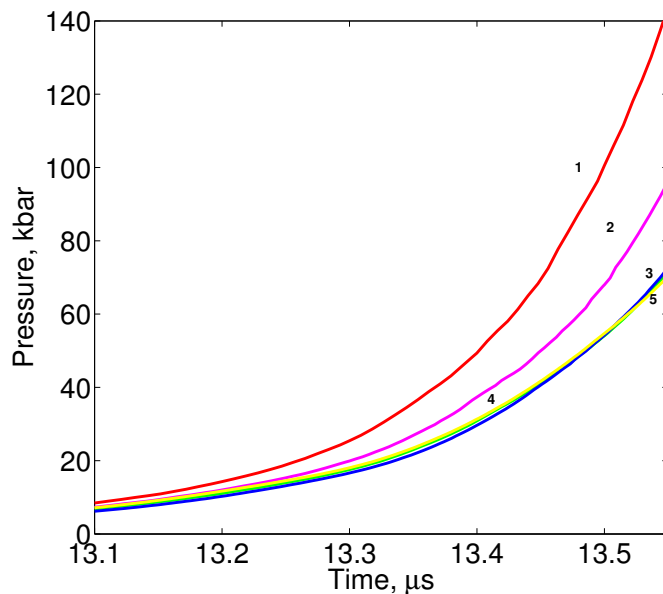
Figure 4.4: Mesh convergence study of average pressure in the target of simulations with mesh size as (1) 5 mm (2) 3 mm (3) 2 mm (4) 1 mm and (5) 2 mm based on 5mm

Besides of that, we also show the convergence study of the 2-dimensional simulations. From Fig. 4.4, average pressure shows good convergence from simulations with 5 mm mesh size to 1 mm mesh size and the simulations with 1 mm and 2 mm mesh size almost coincide with each other.

4.2 2D Studies of Rayleigh-Taylor Instabilities in Plasma Targets

In this section we use only 16 jets case for our study. Because of the nonuniform of the liner formed by an array of plasma jets due to oblique shock with higher density and pressure in the shock region, we expect the instabilities in

plasma target after interaction with the liner. Fig. 4.5 shows the evolution of instabilities in the target with density (left) and pressure (right) distributions. The target exhibits bubbles and spikes until it breaks into fragments. After this target breaking, the behaviors of the fragments seem chaotic. We focus on the stage around target breaking in the following analysis.

Fig. 4.5 shows Rayleigh-Taylor (RT) instabilities in this special regime. RT instability is a fingering instability of an interface between two different materials. The traditional formation is due to gravity, when the fluid is slightly perturbed, the light and heavy fluids inter-penetrate to form bubbles in light fluid and spikes in heavy fluid moving in opposite direction with accelerated speed. This acceleration then decreases because of a balance between buoyancy and form drag forces, resulting in a constant terminal velocity [21]. Our regime is different since the liner is quite nonuniform and there is no random perturbation at the beginning. Here spikes are inward pointing the target and bubbles are outward pointing the liner. The spike and bubble heights measure the radial distance from the origin to the tip of the spike and bubble on the interface respectively. The spike and bubble velocities are in radial direction. Positive and negative velocity means the object moves outwards and inwards respectively. From Fig. 4.6, we find that the bubble and spikes heights keep decreasing and the terminal bubble velocity is constant around 12.6 $\mu s \rightarrow$ 13.1 μs before target starting to break, which are properties of RT instability [21]. After this, the bubble velocity decreases (absolute value). Note that the position calculation, especially for the spikes, is very sensitive.

From the pressure evolution (see Fig. 4.5d and Fig. 4.5f), the wave which

moves toward the origin is reflected outward, then it interacts with the interface which is known as reshock. It then causes Richtmyer-Meshkov (RM) instabilities. The general feature of RM instabilities is described in [22]. As an incident shock collides with the interface, it bifurcates into a transmitted shock and reflected wave detaching from the interface. The incident shock accelerates the growth of bubbles and spikes. The wave moving into the origin causes a pressure singularity and is reflected outward. Then the reflected wave interacts with the interface again as it moves outward (see Fig. 4.5d and Fig. 4.5f). Wave bifurcation can occur again and repeat the previous cycle (see Fig. 4.5f and Fig. 4.5h). If we define amplitude A and the growth rate R as:

$$A = \frac{1}{2}(l_{bb} - l_{sp})$$

$$R = \frac{1}{2}(v_{bb} - v_{sp})$$

where h_{bb} and h_{sp} are bubble and spike heights; v_{bb} and v_{sp} are the bubble and spike velocities. The amplitude and growth rate are plotted in Fig. 4.7. The amplitude keeps increasing and growth rate is changing. It can be explained as follows: At first the growth rate decays which is caused by the resistance to penetration by liner. Then it oscillates a little bit which is a balance result between the resistance and instabilities. At last the instabilities dominate, resulting in the rate increasing.

(a)

(b)

(c)

(d)

(e)

(f)

Figure 4.5

78
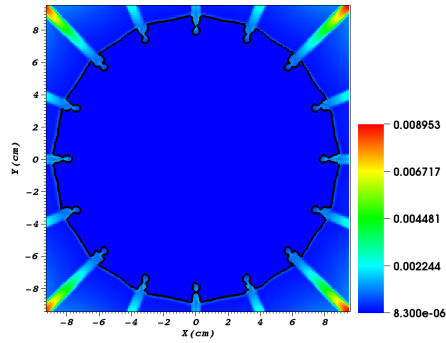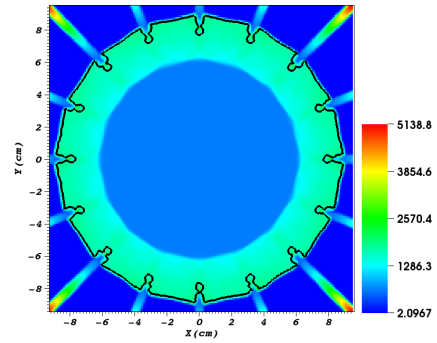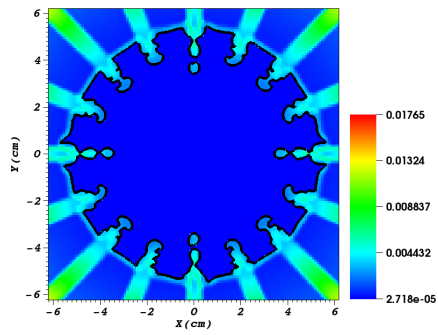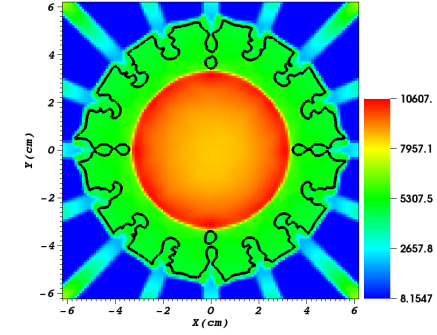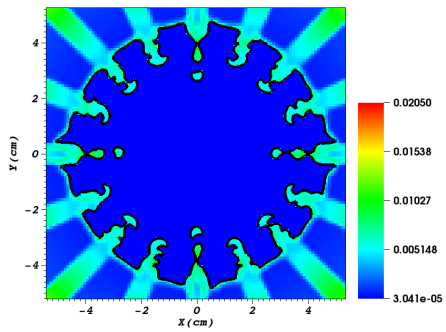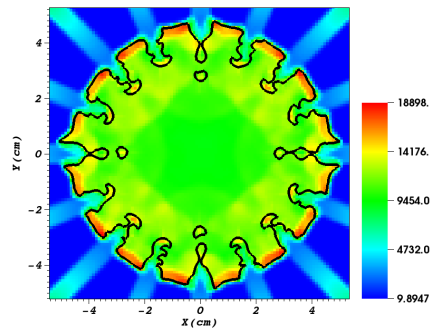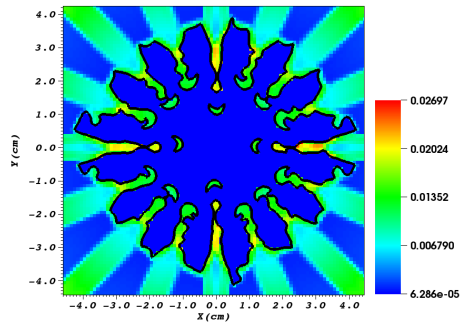
(g)
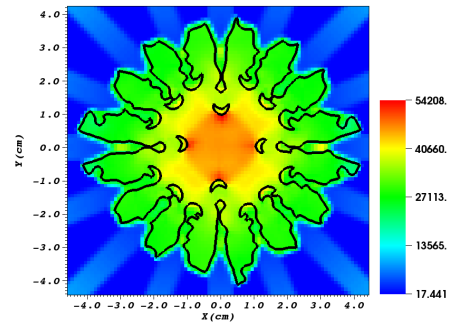
(h)
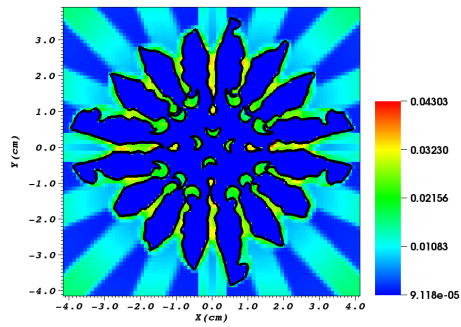
(i)
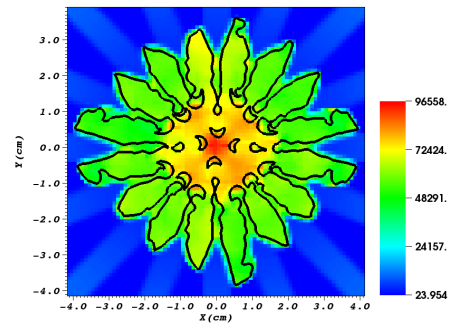
(j)
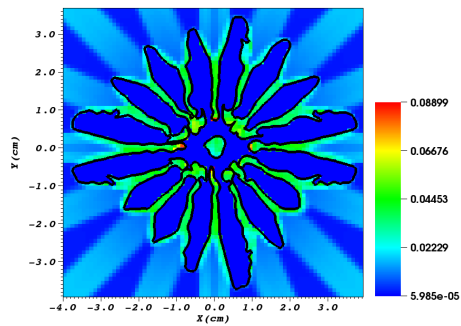
(k)
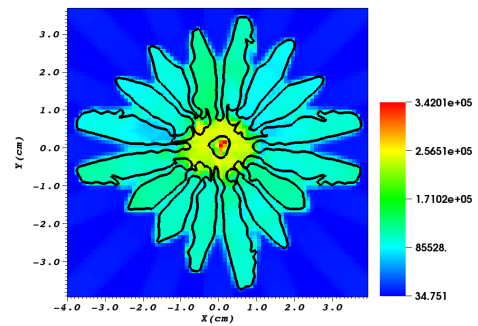
(l)
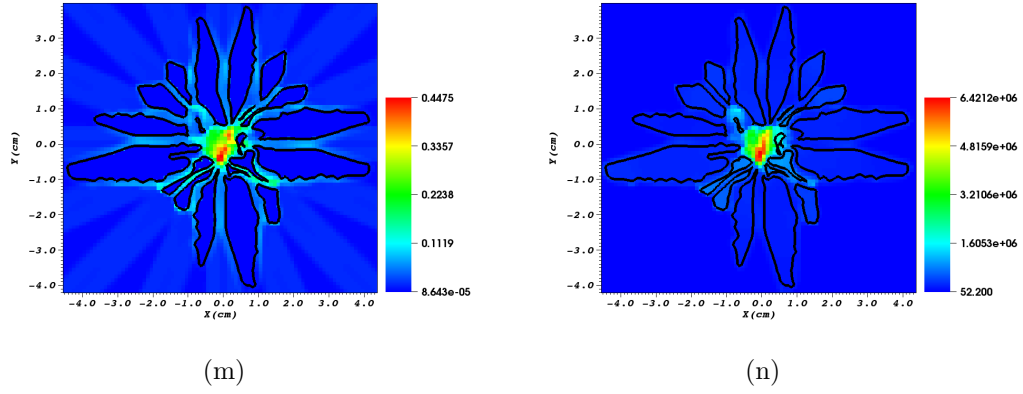
Figure 4.5

Figure 4.5: Interface evolution with density (left) and pressure (right) distributions at same time step for each row.
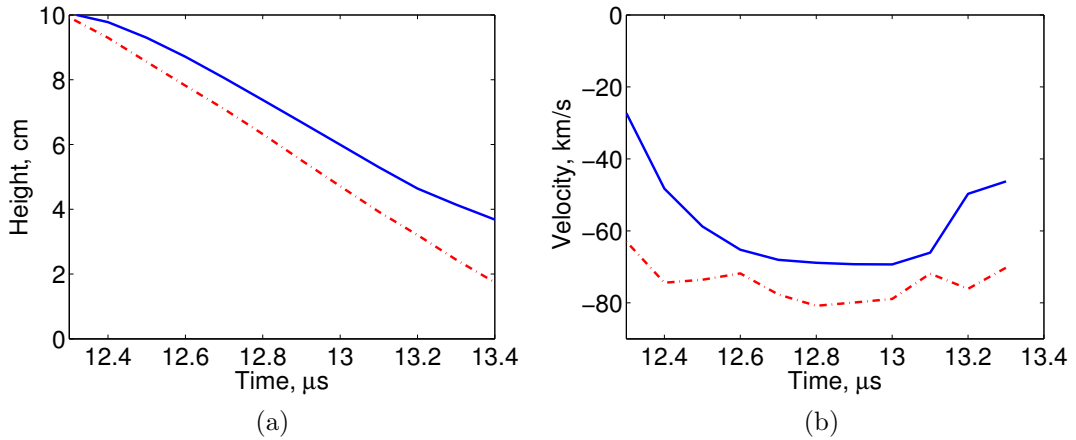
Figure 4.6: (a) Bubble (blue solid line) and spike (red dashed-dotted line) heights (b) Bubble (blue solid line) and spike (red dashed-dotted line) velocities evolution from starting of interaction until around target breaking into fragments for 16 jets with mesh size as 1 mm.
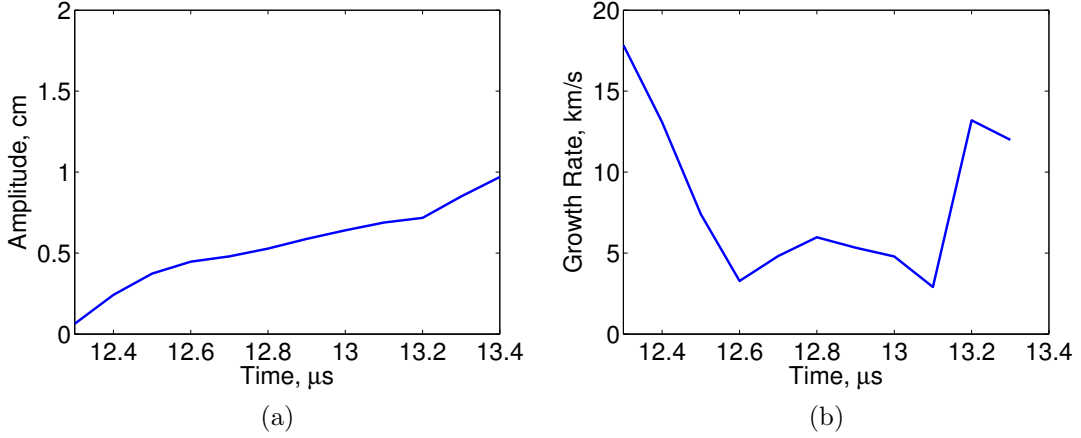
Figure 4.7: (a) Amplitude and (b) Growth rate evolution from starting of interaction until around target breaking into fragments for 16 jets with mesh size as 1 mm.

4.3 Optimization Studies of Target Compression and Fusion Energy

In this section, we study the influence on the target such as fusion energy and stagnation pressure using different numbers of jets (8 jets, 16jets and 32 jets) together with uniform 1-dimension case. Based on same total mass with 16 jets initial conditions, we obtain all the necessary initial conditions for other cases. For 8 jets, density $\rho = 4.6 \times 10^{-3}\,\mathrm{g/cm}^2$, pressure $P = 104\,\mathrm{bar}$, velocity $v = 100\,\mathrm{km/s}$, and Mach number $M = 60$. For 32 jets, density $\rho = 1.15 \times 10^{-3}\,\mathrm{g/cm}^2$, pressure $P = 26.5\,\mathrm{bar}$, velocity $v = 100\,\mathrm{km/s}$, and Mach number $M = 60$. The mesh size is 2 mm with flow through boundary conditions. Fig. 4.8 shows the density distributions of 8 jets and 32 jets before merging into liner.

Fig. 4.9a shows the total fusion energy in the target for different cases,

81
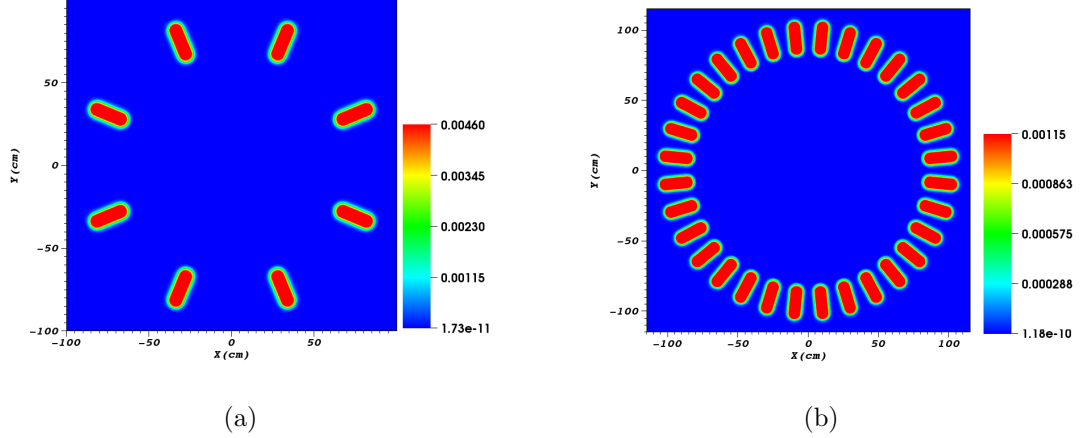
Figure 4.8: Density distribution(g/cm^2) of (a) 8 jets and (b) 32 jets

where the time t is around 14 μs. The uniform case (cylindrical symmetry) gives us the largest value, 4.62×10^{12} ergs. The second one is 32 jets case with fusion energy as 8.19×10^{11} ergs, around 5.6 times higher than that of 16 jets (1.46×10^{11} ergs) and around 9 times higher than that of 8 jets (9.07×10^{10} ergs). Fig. 4.9b shows the largest pressure of the uniform case is around 5.5 mbar. For the jet cases we focus on average pressure since it makes more sense. Here 32 jets case gives us the second largest average pressure as 1.32 mbar, around 2 times higher than that of 16 jets (0.632 bar) and around 2.5 times higher than that of 8 jets (0.531 mbar) from Fig. 4.9b. As we have mentioned in section 4.2, states after target breaking are very unstable and the maximum values of fusion energy and average pressure in the target are very sensitive.

From the above statement, we know that the uniform case always gives the upper bound of total fusion energy and pressure. This is obvious from what we have mentioned in chapter 3. The oblique shock waves caused by the neighboring jets reduce the Mach number of the liner and the ability to
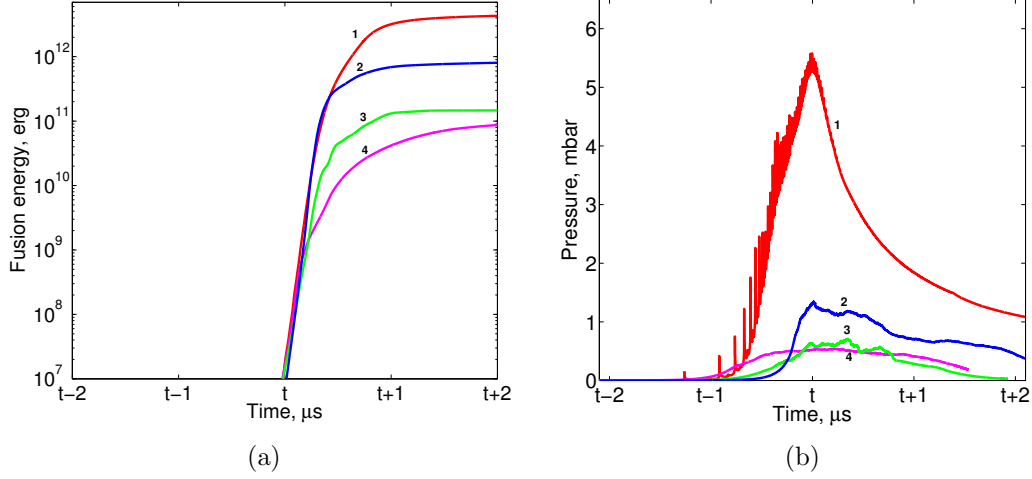
Figure 4.9: (a) Total fusion energy comparison of (1) uniform case, (2) 32 jets, (3) 16 jets and (4) 8 jets; (b) Average pressure of the target (1) uniform case, (2) 32 jets, (3) 16 jets and (4) 8 jets

compress the target. As a result of this and other factors, the maximum pressure and fusion energy in the target of uniform liner significantly exceed values achievable in liner formed by the merger of jets. And the more numbers of the jets, the larger value it is. This can be explained in the following two ways. First is the increase of the liner uniformity with the increase of the number of jets. A 1-dimensional uniform liner can be regarded as the merger of infinite number of jets. Second is the merging radius. Similar to the deduction in [2], we determine the merging radius by equating the circumference $2\pi r_m$ with the sum of the cross-sectional length of each jet in 2D.

$$2\pi r_m = 2Nb(r_m) \tag{4.1}$$

Because of the finite temperature within the jet, the jet pulse expands on its

83

way to the merging radius. The liner expansion model with constant initial sound speed predicts the increase of the jet radius b as $b(r_m) = b_0 + c_0(r_c - r_m)/u_j$. Here b_0 is the initial jet radius, u_j is the initial jet speed, M_j is the initial jet Mach number, $c_0 = u_j/M_j$ is the initial sound speed, r_c is the chamber radius and r_m is the merging radius. By substituting this into Eq.4.1, we obtain the merging radius

$$r_m = \frac{r_0 + r_c/M_j}{\pi/N + 1/M_j} \tag{4.2}$$

From the scaling laws, 32 jets case gives us the largest radius (63 cm), which then shows more ability to compress the target.

Fig. 4.10 depicts the evolution of the normalized average pressure in the target, the normalized total fusion energy and the normalized fusion energy at each time step (the rate) in the vicinity of the stagnation point for each case, where the time t is around 14 μs. The normalized average pressure in the target and the normalized fusion energy at each time step show similar shapes because of the definition of fusion energy. Recall the definition of deconfinement time: the fusion energy is more than 90% complete after the pressure in the target is reduced by the factor of 2. From Fig. 4.10, the deconfinement time for each case is observed. It's around 1.13 μs for 8 jets, 0.95 μs for 16 jets, 1.1 μs for 32 jets and 0.52 μs for uniform case. As we know, the maximum pressure is very unstable due to the instabilities in the target (see section 4.2), we allow certain deviations of deconfinement time. Here the uniform case gives the smallest deconfinement time, the possible reasons are:

it is the ideal case with ideal target compression and quick deconfinement; the target in the jet case breaks into fragments, whose evolution is much slower because of non-uniform motion; the jet case is using average pressure, which does not show the pressure evolution quite accurately.

4.4   3D Simulation of Plasma Targets

We have discussed 2-dimensional spherical liner-target simulations in previous section, now we focus on 3-dimenstional simulations with multi-stage scheme mentioned in section 4.1. The scheme is described as follows: First we perform the simulation of the propagation of a single detached argon jet from the nozzle of the plasma gun. Here we use the code features of solving the Riemann problem, front tracking and applying plasma EOS model. We use jet with following initial conditions: initial inner radius and outer radiuses are 137.2 cm and 162.7 cm, density $\rho = 8.04 \times 10^{-4}$ g/cm^3, pressure $P = 18.59$ bar, velocity $v = 100$ km/s, and Mach number $M = 60$. The ambient vacuum is modeled as rarefied gas with density $\rho_0 \sim 10^{-9}$ g/cm^3 and pressure $\sim 10^{-6}$ bar. The mesh size is 2 mm with reflecting boundary for left side and flow through boundary conditions for other sides. Second after we obtain the profiles for the single jet before the merger, we first find directions for 90 jets uniformly distributed in space using Spherical Centroidal Voronoi Tessellation (SCVT) as in chapter 3 and then initialize states around each direction based on pressure, density, and velocity profiles from single jet simulation. In order to be in accordance with 16 jets in 2-dimensional space, we use 90 jets in 3-dimensional simulation since the angle between the nearest two jets are both
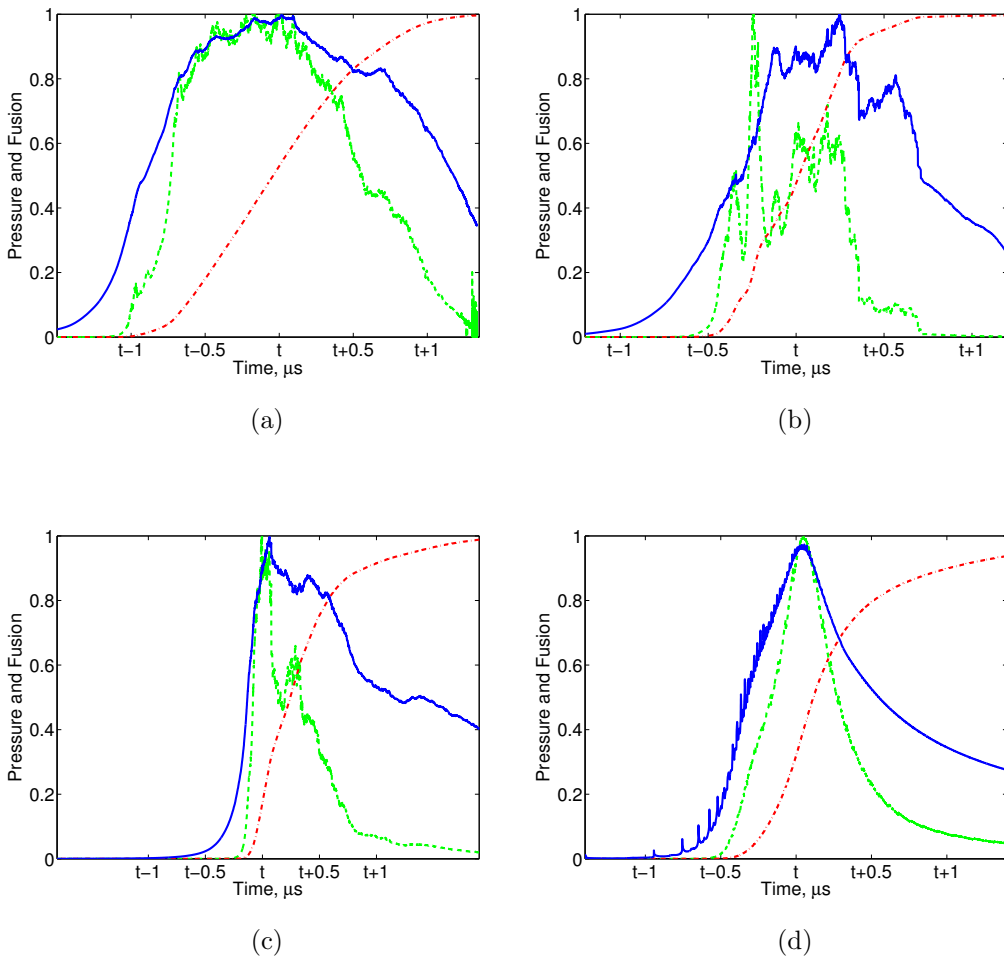
Figure 4.10: Evolution of normalized average pressure of the target (blue solid line), normalized total fusion energy (red dash-dotted line), normalized fusion energy at each time step (green dashed line) during target deconfinement with (a) 8 jets, (b) 16 jets and (c) 32 jets (d) uniform case

around 0.39. The mesh size is 5 mm with flow through boundary conditions and we use this coarse mesh simulation later for our refinement run (2 mm). The target is not included in this coarse simulation since we only need the liner information before liner-target interaction. Fig. 4.11 and Fig. 4.12 depict density and pressure contours before and after merger. Due to oblique shock waves, we observe same phenomenon as in chapter 3. At the later stage, the highest pressure and density appear along the plane of interaction of the neighboring jets. This non-uniform distribution causes the instabilities on the target. We also observe the contours with shapes of pentagon and hexagon.

Finally, we take the data of the center area from the previous simulation with 5 mm mesh size when the liner is still not reaching the target and then do the mesh refinement (2 mm) run to save computational time and processors to be used. The target condition is same as before: density $\rho = 8.3 \times 10^{-6}\,\mathrm{g/cm^3}$, pressure $P = 640.3\,\mathrm{bar}$. In order to prevent target diffusion, we set the velocity of the target to be zero before the liner-target interaction. As we have mentioned in 2-dimensional simulation, the target breaks into fragments because of the non-uniform pressure and density distributions in the liner. The target behavior is unstable and complicated after this stage and in this section we only focus on the properties before this stage. Fig. 4.13 and Fig. 4.14 depict density and pressure contours evolution in the center region including liner and target. Fig. 4.14 shows the interaction between the liner and target with formation of bubbles and spikes on the target at later stage. Here spikes are inward pointing toward the target and bubbles are outward pointing toward the liner. Similar instabilies as we have discussed the details in section 4.3

(a)

(b)

(c)

(d)
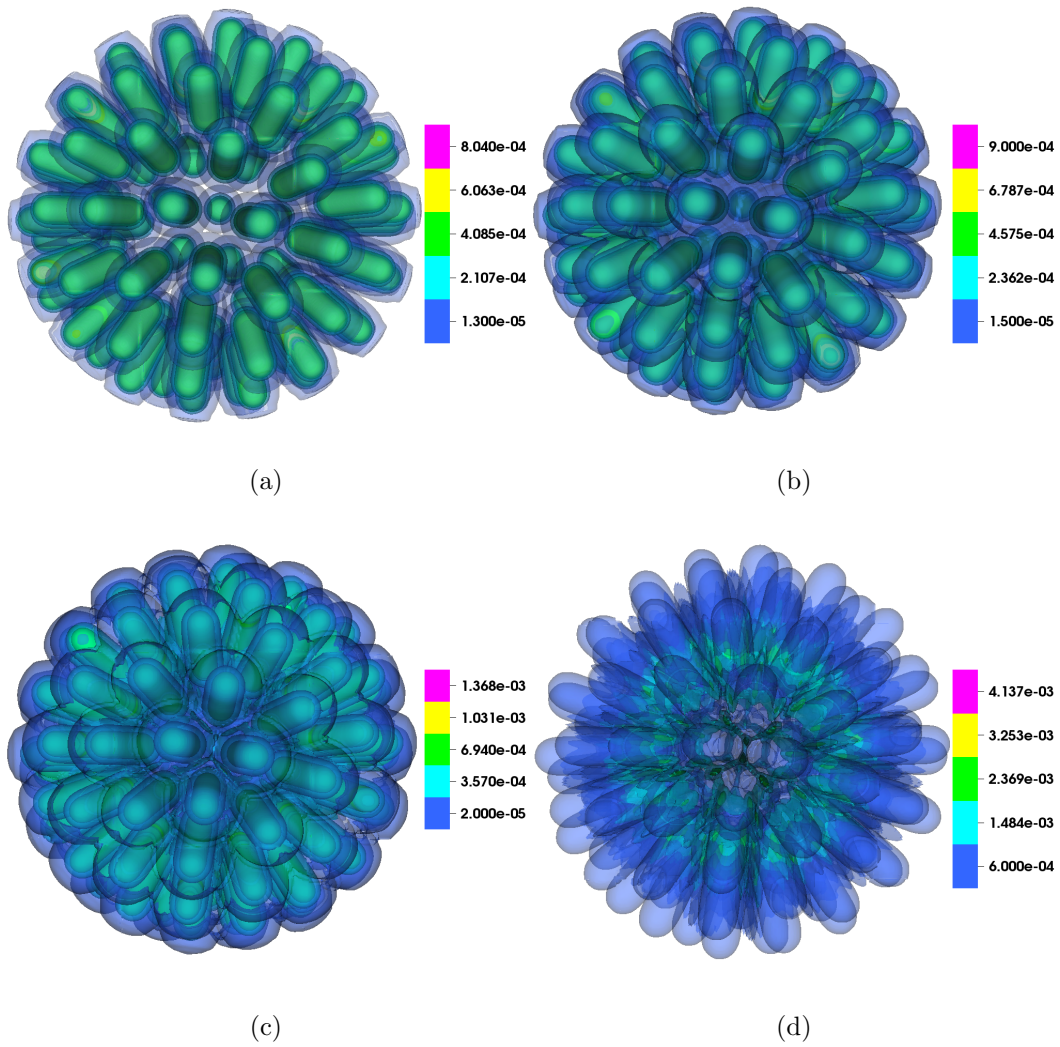
Figure 4.11: Density contour evolution of the liner formed by 90 jets before interaction with the target.
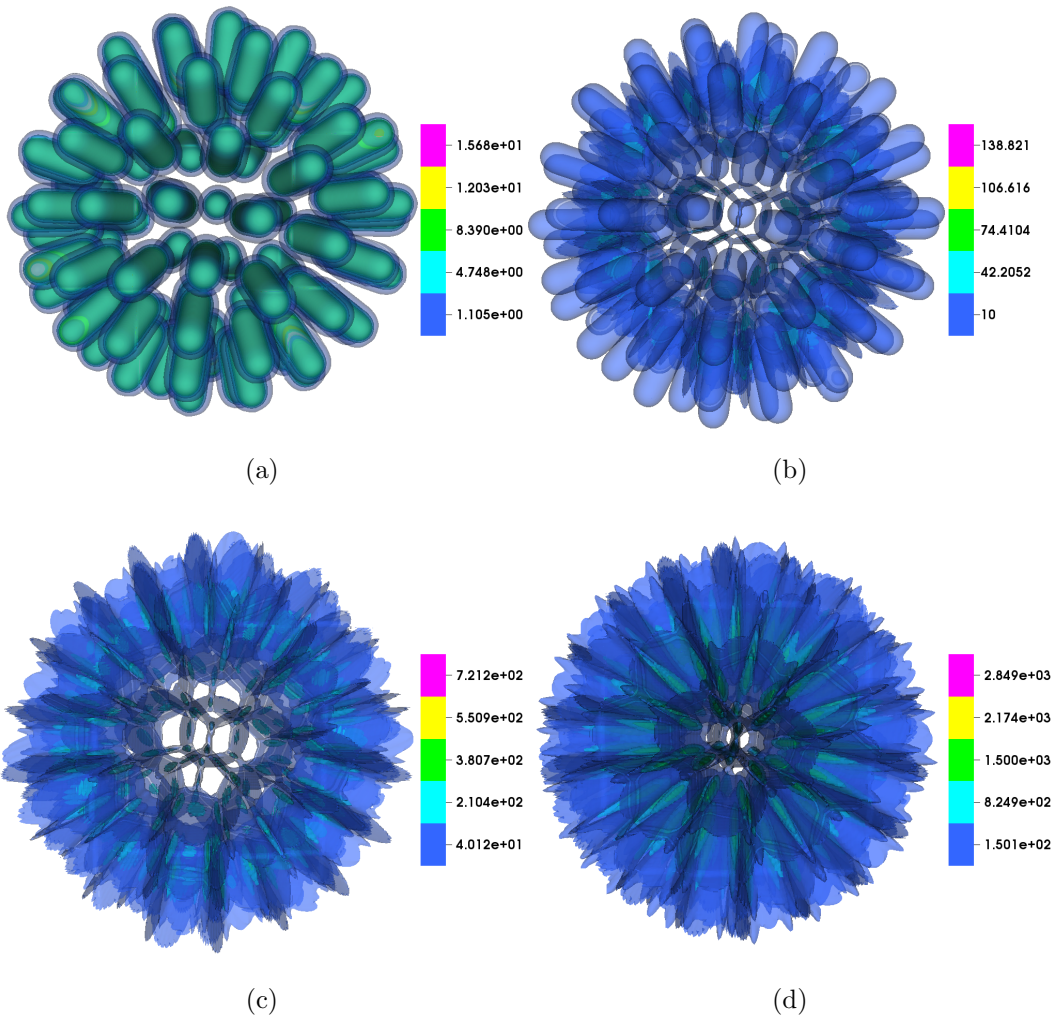
Figure 4.12: Pressure contour evolution of the liner formed by 90 jets before interaction with the target.

are observed. The region with higher density and pressure along the plane of interaction of the neighboring jet compresses the target with higher ability and bubbles and spikes are obtained. The instabilities are amplified as time goes by. In order to inspect the evolution of the target more clearly, we present the evolution of target together with pressure distribution on the interface in Fig. 4.15. The maximum appears on the spikes, in the region of interaction of the neighboring jets which is also the region of the maximum pressure for the liner due to oblique shock waves. The target finally breaks because of this uneven pressure distribution. Using the same definitions of bubble and spike heights and amplitude as in section 4.3, Fig. 4.16 and Fig. 4.17 show similar patterns as in Fig. 4.6 and Fig. 4.7. The bubble and spike heights keep decreasing and the terminal bubble velocity is constant around 12.6 $\mu s \rightarrow$ 13.1 μs before target starting to break while the amplitude keeps increasing.

At last, we perform 1-dimensioal spherical symmetric (3-dimensinal uniform liner) simulation to do the comparison study. The initial condition is proposed as follows with inner and outer radiuses as 137.2 cm and 162.7 cm respectively: density $\rho = 1.744 \times 10^{-5}\,\mathrm{g/cm^3}$, pressure $P = 0.421\,\mathrm{bar}$, velocity $v = 100\,\mathrm{km/s}$, and Mach number $M = 60$. The mesh size is 2 mm with flow through boundary condition for right side and reflecting boundary for left side. Fig. 4.18 shows the average pressure in the target for different cases. Note that we only focus on the time range around the time when target breaks into fragments for stable results. The pressures of 3-dimensinal (90 jets) case and 2-dimensional (16 jets) case are very close to each, around $P = 7.5e4\,\mathrm{bar}$ and $P = 7.1e4\,\mathrm{bar}$ respectively at the end of this time range. The pressure of uni-

form cases is always higher as expected because of the impact of oblique shock waves for jet case. The 3-dimensinal uniform case (1-dimenstional spherical geometry) is around $P = 6.3 \times 10^6$ bar while the 2-dimensinal uniform case (1-dimenstional cylindrical geometry) is around $P = 1.3 \times 10^6$ bar. The pressure of 3-dimensinal uniform case is almost 80 times higher than that of the 90 jets case. Note what we have mentioned in chapter 3, the difference of stagnation pressure between 3 dimensional simulation and 1 dimensional uniform case is around 50 times for self-collapse simulations.

(a)   (b)

(c)   (d)
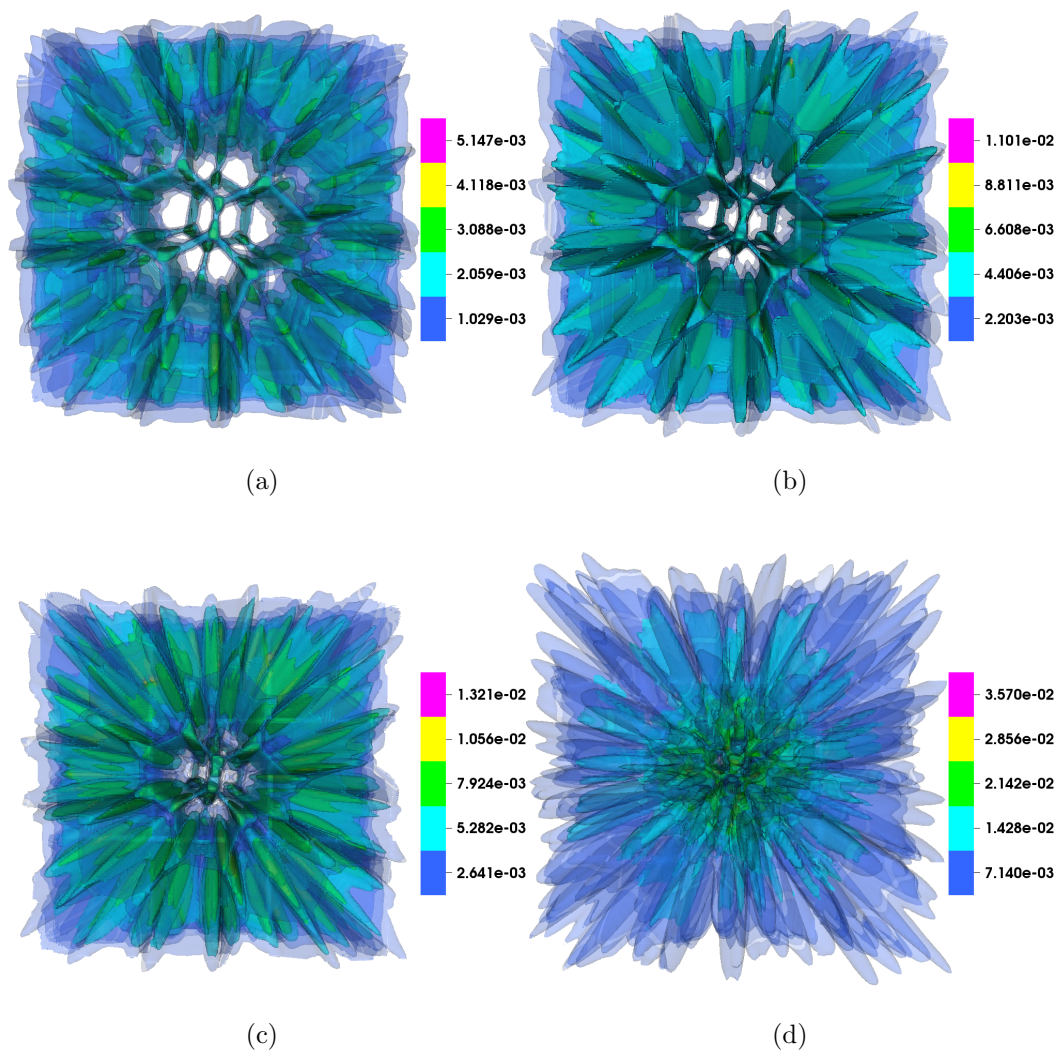
Figure 4.13: Density contour evolution of the liner and the target after interaction.

(a)

(b)

(c)

(d)
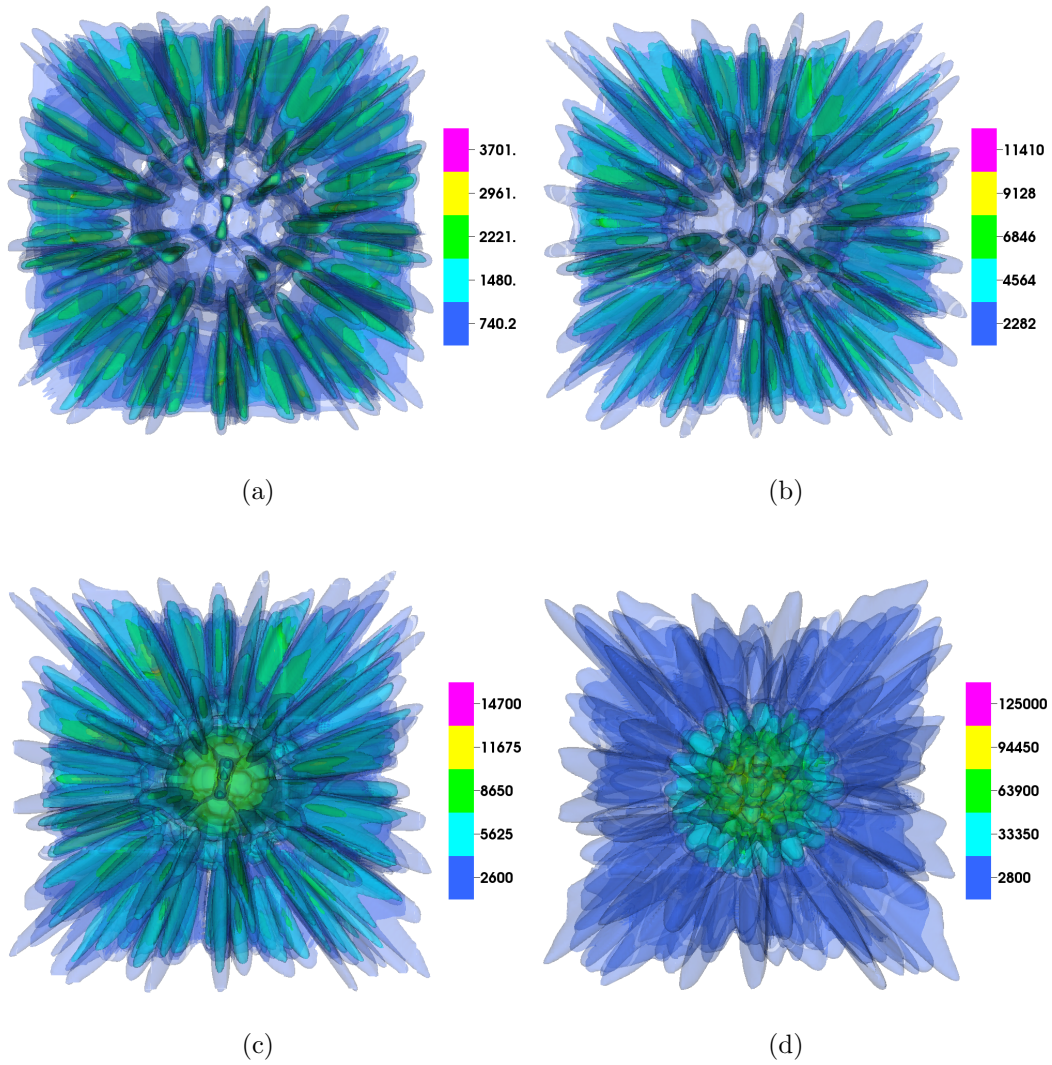
Figure 4.14: Pressure contour evolution of the liner and the target after inter-action.
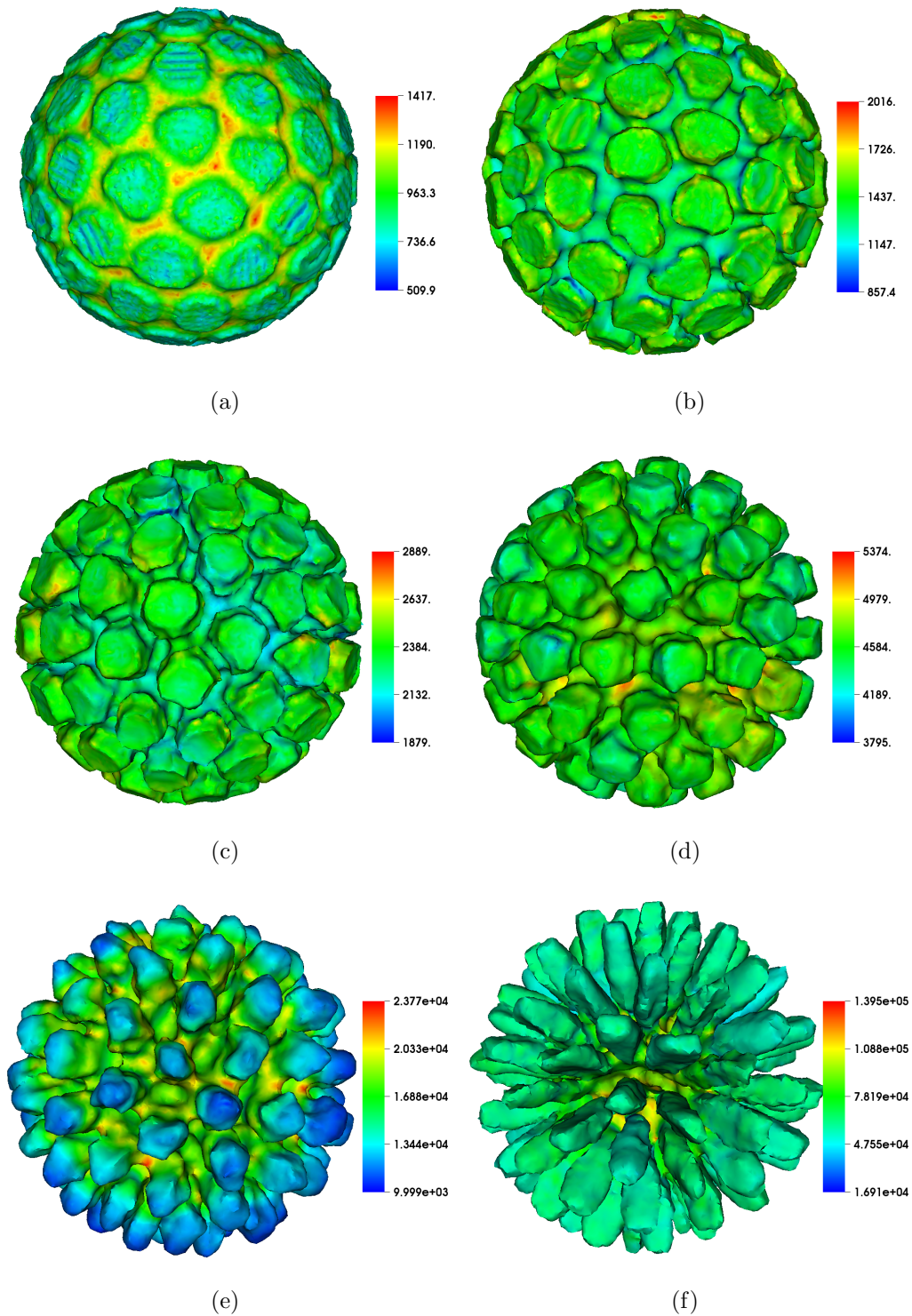
Figure 4.15: Target evolution together with pressure distributions on the interface.

94
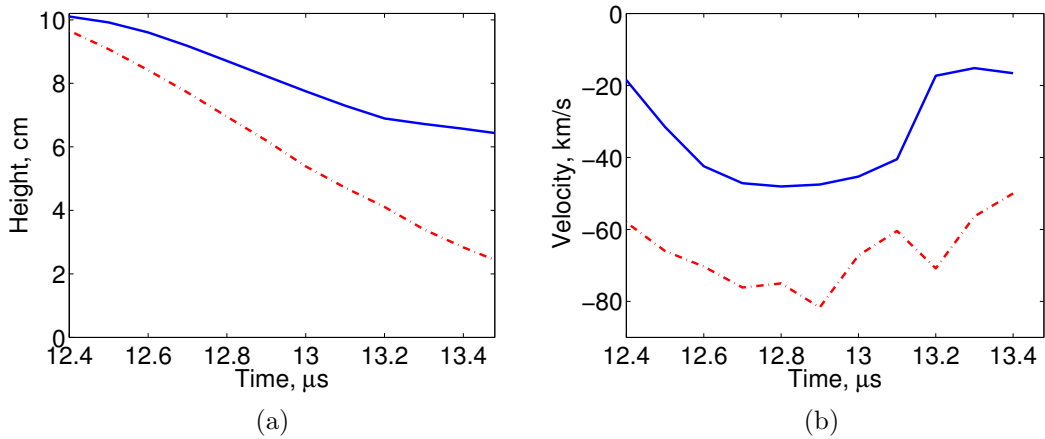
Figure 4.16: (a) Bubble (blue solid line) and spike (red dashed-dotted line) heights and (b) Bubble (blue solid line) and spike (red dashed-dotted line) velocities evolution from starting of interaction until around target breaking into fragments for 3-dimensional simulation with mesh size as 2 mm based on 5 mm.
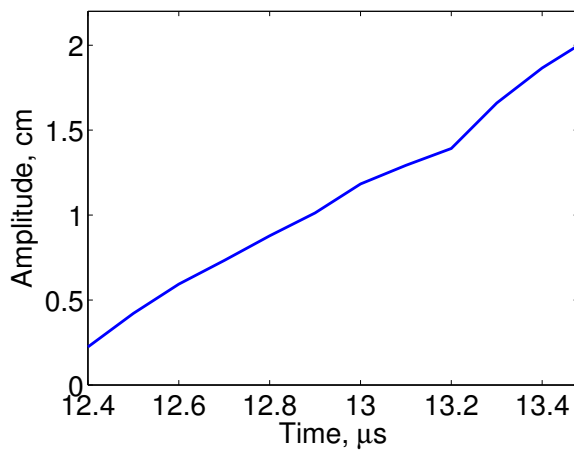
Figure 4.17: Amplitude evolution from starting of interaction until around target breaking into fragments for 3-dimensional simulation with mesh size as 2 mm based on 5 mm.
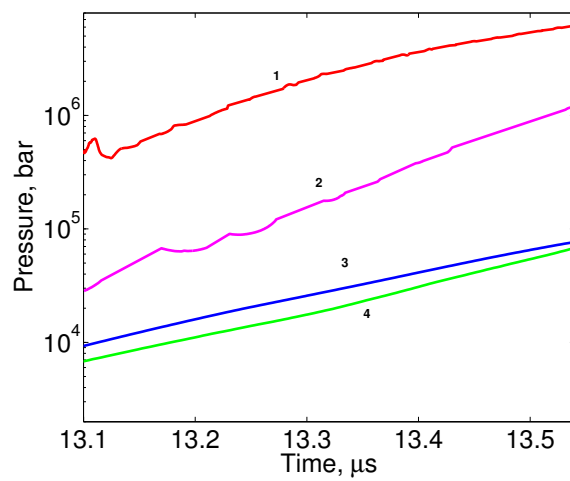
Figure 4.18: Average pressure in target for (1) 3-dimensional uniform case (1-dimenstional spherical geometry); (2) 2-dimensional uniform case (1-dimenstional cylindrical geometry); (3) 3-dimensional case (90 jets); (4) 2-dimensional case (16 jets).

Chapter 5

Conclusions and Future Directions

In this thesis, one of the most important issues we focus is to improve the fusion energy gain. According to the scaling law, the gain increases with the reduction of the liner thickness provided that such a liner is still capable of compressing the target. Keeping the liner unchanged, there is also an optimal choice for the target radius using the initial conditions to get the maximum fusion energy gain. We also use heavy material such as argon for liner to generate better results. Another way is to describe the process more accurately in our simulations. Compared with previous theoretical and numerical studies of PJMIF, our numerical models and algorithms implement several new physics models important to PJMIF. We have investigated the influence of atomic physics processes on the implosion of deuterium and argon liners for magneto-inertial fusion via numerical simulations in spherically symmetric geometry. The EOS models for deuterium and argon, valid in the approximation of local thermodynamic equilibrium, present processes of dissociation (for molecular deuterium) and ionization. The numerical EOS for argon, built upon ideas of

97

the average ionization model proposed by Zeldovich, is verified using accurate solutions of the coupled system of Saha equations. These EOS models have been implemented in the FronTier code [15] and used for all the included plasma simulations. With plasma EOS, we obtained more fusion energy and stagnation pressure. Another factors influencing liner implosion are residual vacuum gas and heat conduction. For the cases of self-collapse, as the liner goes inward, the condition in the center of the simulation is not realistic. We replace the idealized vacuum region with realistic residual gas and check the results. There is no heat conduction in our previous implosion processes. By applying the Spitzer electronic thermal conductivity, we have a more accurate description for our simulations.

A study of the self-implosion and the internal structure of a plasma liner formed by the merger of 30 argon plasma jets relevant to the PLX experiment have been performed via 3-dimensional numerical simulations using the FronTier code. To reduce the computational cost, a cylindrically symmetric 2-dimensional simulation of detached jet from plasma gun was obtained first and simulation results were embedded in a 3-dimensional simulation which had an optimized computational domain. We applied a numerical model for the argon equation of state [7] which captures the ionization of argon atom. Our study demonstrates that the jet merger process is accomplished via a cascade of oblique shock waves that heat the liner, reduce its Mach number, and lower the self-collapse pressure. To demonstrate the formation of cascades of oblique shock waves in simpler geometry, a 2-dimensional simulation of the merger of polytropic gas jets was performed and results were compared

with the oblique shock theory. We achieved a good agreement with theory on after-shock states of gas after the first and second oblique shocks. The 3-dimensional jets merger process is complicated by (1) secondary shocks due to three-jet interactions, (2) spreading out of free jets in the longitudinal and transverse directions, (3) change of the ionization fraction across the oblique shock wave, and (4) heating associated with the adiabatic compression. We compared the self-implosion density and pressure of the 3-dimensional liner with the pressure and density of 1-dimensional liners with the sharp profile at the merging radius and with profile identical to the average profile of the 3-dimensional liner. We observed that the self-implosion pressure of the 3-dimensional liner, 6.4 kbar, is 10 times smaller compared with the pressure of the equivalent 1-dimensional liner (64 kbar), and 50 times smaller compared with the 1-dimensional liner with the sharp profile at the merging radius (320 kbar). Mesh convergence studies have been performed for all simulations to ensure that results are not affected by the numerical resolution. The number of jets used in this study was dictated by the current experimental equipment and not the liner optimization considerations.

For spherically symmetric 1-dimensional liner, we study the scaling laws and related theories based on its uniform structure. But due to the oblique shock waves and other factors, the internal structure of plasma liners formed by jets is not uniform. We then performed 2-dimensional simulations with 16 jets to show this effect on the target. A multi-stage scheme was proposed to save computational time and we observed good convergence for this scheme. The Rayleigh-Taylor (RT) instabilities on the interface were also investigated

in detail. RT instability is an instability of an interface between two fluids of different densities that occurs when one of the fluids is accelerated into the other [21]. The instability in our simulations is not in traditional sense since the liner is moving because of its own energy instead of gravity and there is no random perturbation at the beginning and it is also combined with Richtmyer-Meshkov instability [22]. The target breaks into fragments at the end. The growth rate showed a balance result between the resistance to penetration by liner and instabilities. We also performed different numbers of jets (8 jets and 32 jets) to form the liners and compared the results. The more numbers of the jets, the larger value it is. This can be explained by the increase of the liner uniformity with the increase of the number of jets. 1-dimentional uniform liner can be regarded as the merger of infinite number of jets. 3-dimentional simulations were also performed to get further investigation. In order to be in accordance with 16 jets in 2-dimentional space, we use 90 jets in 3-dimensional simulation since the angle between the nearest two jets are both around 0.39. In 3-dimentional simulation, the interface structure is much more complicated as it is a surface. Based on multi-stage scheme, the coarse mesh size is 5mm and we use this coarse simulation later for our refinement run (2 mm). Spikes were observed on the target and similar analysis was drawn as in 2-dimensional simulations. Since 3-dimensional simulation is very complicated and the states in the target are unstable after target breaking into fragments, we just focused on the stage before breaking. The average pressure for 3-dimensional uniform case is almost 80 times higher than that of the 90 jets simulation at the end of this time range.

Multiphase MHD in the low magnetic Reynolds number approximation based on front tracking has already been developed in FronTier and used for the simulation of mercury targets for Neutrino Factory / Muon collider [19, 34] and cryogenic pellets for tokamak fueling [35, 36]. Since the low magnetic Reynolds number approximation is not quite suitable for the description of MHD processes in the imploding liner and magnetized target, we propose to make theoretical analysis of a new MHD with more accurate description of the target physics model within the method of front tracking in the future. We will use this new model to describe the motion of the target - vacuum interface as the electrical conductivity changes from zero in the vacuum to infinity in the target.

Bibliography

[1] Y. C. F. Thio, E. Panarella, C. E. Knupp R. C. Kirkpatrick, F. Wysocki, P. Parks, and G. Schmidt. Magnetized target fusion in a spheroidal geometry with standoff drivers. *in Current Trends in International Fusion Research II, edited by E. Panarella, National Research Council Canada, Ottawa, Canada*, 1999.

[2] P. B. Parks. On the efficacy of imploding plasma liners for magnetized fusion target compression. *Phys. Plasmas*, 15:062506, 2008.

[3] R. Samulyak, P. Parks, and L. Wu. Spherically symmetric simulation of plasma liner driven magnetoinertial fusion. *Phys. Plasmas*, 17:092702, 2010.

[4] T. J. Awe, C. S. Adams, J. S. Davis, D. S. Hanna, and S. C. Hsu. One-dimensional radiation-hydrodynamic scaling studies of imploding spherical plasma liners. *Phys. Plasmas*, 18:072705, 2011

[5] S. C. Hsu, E. C. Merritt, A. L. Moser, T. J. Awe, S. J. E. Brockington, J. S. Davis, C. S. Adams, A. Case, J. T. Cassibry, J. P. Dunn, M. A. Gilmore, A. G. Lynn, S. J. Messer, and F. D. Witherspoon. Experimental characterization of railgun-driven supersonic plasma jets motivated by high energy density physics applications. *Phys. Plasmas*, 19:123514, 2012.

[6] J. T. Cassibry, M. Stanic, S. C. Hsu, S. I. Abarzhi, F. D. Witherspoon. Tendency of spherically imploding plasma liners formed by merging plasma jets to evolve toward spherical symmetry. *Phys. Plasmas*, 19:052702, 2012.

[7] H. Kim, R. Samulyak, L. Zhang, P. Parks. Influence of atomic processes on the implosion of plasma liners. *Phys. Plasmas*, 19:082711, 2012.

[8] J. S. Davis, S. C. Hsu, I. E. Golovkin, J. J. MacFarlane, and J. T. Cassibry. One-dimensional radiation-hydrodynamic simulations of imploding

spherical plasma liners with detailed equation-of-state modeling *Phys. Plasmas*, 19:102701, 2012.

[9] J. Santarius. Compression of a spherically symmetric deuterium-tritium plasma liner onto a magnetized deuterium-tritium target. *Phys. Plasmas*, 19:072705, 2012.

[10] H. Kim, L. Zhang, R. Samulyak, P. Parks. On the Structure of Plasma Liners for Plasma Jet Induced Magnetoinertial Fusion *Phys. Plasmas*, 20:022704, 2012.

[11] S. C. Hsu, T. J. Awe, S. Brockington, A. Case, J. T. Cassibry, G. Kagan, S. J. Messer, M. Stanic, X. Tang, D. R. Welch, and F. D. Witherspoon. Spherically imploding plasma liners as a standoff driver for magnetoinertial fusion. *IEEE Transactions on Plasma Science*, 40:1287, 2012.

[12] J. T. Cassibry, R. J. Cortez, S. C. Hsu, and F. D. Witherspoon. Estimates of confinement time and energy gain for plasma liner driven magnetoinertial fusion using an analytic self-similar converging shock model. *Phys. Plasmas*, 16:112707, 2009.

[13] E. C. Merritt, A. L. Moser, S. C. Hsu, J. Loverich, M. Gilmore. Experimental characterization of the Stagnation Layer between Two Obliquely Merging Supersonic Plasma Jets. *Phys. Rev. Lett*, 111:085003, 2013.

[14] J. Glimm, J. Grove, X. L. Li, K. L. Shyue, Q. Zhang., and Y. Zeng. Three dimensional front tracking. *SIAM J. Sci. Comput.*, 19:703–727, 1998.

[15] B. Fix, J. Glimm, X. Li, Y. Li, X. Liu, R. Samulyak, and Z. Xu. A TSTT integrated frontier code and its applications in computational fluid physics. *Journal of Physics: Conf. Series*, 16:471–475, 2005.

[16] J. Glimm, J. W. Grove, X. Li, W. Oh, D. H. Sharp A critical analysis of RayleighTaylor growth rates. *J. Comput. Phys.*, 169 (2001), p. 652.

[17] B. van Leer. Towards the ultimate conservative difference scheme: V. A second order sequel to Godunov's method. *J. Comput. Phys.*, 32 (1979) 101-136.

[18] W. Bo, B. Fix, J. Glimm, X. Li, , X. Liu, R. Samulyak, L. Wu FronTier and Applications to Scientic and Engineering Problems. *Proc. in Appl. Math. and Mech.*, 7 (2007), 1024507.

[19] R. Samulyak, J. Du, J. Glimm, and Z. Xu. A numerical algorithm for MHD of free surface flows at low magnetic reynolds numbers. *J. Comput. Phys.*, 226:1532–1546, 2007.

[20] R. Samulyak, T. Lu, and P. Parks. A hydromagnetic simulation of pellet ablation in electrostatic approximation. *Nuclear Fusion*, 47:103–118, 2007.

[21] D. H. Sharp. An overview of Rayleigh-Taylor instability. *Physica D: Nonlinear Phenomena*, volume 12, Issue 1-3, p. 3-3, 1984.

[22] J. Glimm, J. W. Grove, Y. Zhang. Numerical calculation of Rayleigh-Taylor and RichtmyerMeshkov instabilities for three dimensional axisymmetric flows in cylindrical and spherical geometries. *SUNY Preprint* SUNYSB-AMS-99-22, *LANL Preprint* LA-UR 99-6796, 1999.

[23] H. S. Bosch and G. M. Hale. Improved formulas for fusion cross-section and thermal reactivities. *Nucl. Fusion*, 32:611, 1992.

[24] Ya. B. Zel'dovich and Yu. P. Raizer. *Physics of shock waves and high-temperature hydrodynamic phenomena.* Dover, 2002.

[25] F. S. Felber, P. B. Parks, R. Prater, and D. F. Vlasow. Effect of atomic processes on fuel pellet ablation in thermonuclear plasma. *Nucl. Fusion*, 19:1061, 1979.

[26] J. Du, B. Fix, J. Glimm, X. Jia, X. Li, Y. Li, and L. Wu. A simple package for front tracking. *J. Comput. Phys.*, 213:613 – 628, 2006.

[27] See http://people.sc.fsu.edu/ jburkardt/f_src/sphere_cvt/sphere_cvt.html for further information about SCVT software.

[28] Q. Du, V. Faber, M. Gunzburger. Centroidal Voronoi Tessellations: Applications and Algorithms. *SIAM Review*, 41:637 – 676, 1999.

[29] J.D. Huba, NRL Plasma Formulary, 2011 Edition.

[30] Charles E. Knapp. An implicit smooth particle hydrodynamic code. PhD thesis, Los Alamos national laboratory, 2000.

[31] R. Courant, K.O. Friedrichs. *Supersonic Flow and Shock Waves*, Springer, 1991.

[32] S. C. Hsu et al. "Summary of Plasma Liner Experiment (PLX) Research Results," 54th Annual Meeting of the APS-DPP (2012).

[33] E. Merritt. "PLX is assessing single and merged plasma jet properties in support of plasma liner experiments," 54th Annual Meeting of the APS-DPP (2012).

[34] R. Samulyak, Y. Prykarpatskyy, Richtmyer-Meshkov instability in liquid metal flows: influence of cavitation and magnetic fields, Mathematics and Computers in Simulations, 65 (2004), 431 - 446.

[35] R. Samulyak, T. Lu, P. Parks, A magnetohydrodynamic simulation of pellet ablation in the electrostatic approximation, Nuclear Fusion, 47 (2007), 103-118.

[36] P. Parks, T. Lu, R. Samulyak, Charging and $E \times B$ rotation of ablation clouds surrounding refueling pellets in hot fusion plasmas, Physics of Plasmas, 16, 060705 (2009).